Computational Investigations of Photocatalytic Surfaces exhibiting Spatially Selective Reactivity

Submitted in partial fulfillment of the requirements for

the degree of

Doctor of Philosophy

in

Materials Science and Engineering

James J. Glickstein

B.S., Engineering Science, The Pennsylvania State University
M.S., Materials Science and Engineering, Carnegie Mellon University

Carnegie Mellon University
Pittsburgh, PA

August 2016

ACKNOWLEDGEMENTS

This work was made possible by the ideas, assistance, and support of a number of people.

First, I would like to thank my advisors Dr. Paul Salvador and Dr. Gregory Rohrer for their guidance and intellectual commitment. They have taught me how to conduct scientific analyses, how to evaluate and critique the work of others, and how to effectively communicate technical ideas. Their influence is present throughout this thesis and will impact my work in future endeavors. I would also like to thank Dr. Lisa Porter, Dr. Mohammad Islam, and Dr. Paul Sides for their dedication in serving on my dissertation committee. Their insights and critical analyses have guided and strengthened my research. This work would not have been possible without the financial support of the National Science Foundation Grant DMR 1206656, for which I am deeply appreciative.

Many staff members and students of the Department of Materials Science and Engineering have assisted in my research and educational pursuits. I would like to thank Suzanne Smith, Marygrace Antkowski, Kelly Rockenstein, and Jeanna Pekarcik for their administrative help. I would also like to acknowledge Jason Wolf, Dr. Adam Wise, and William Pingitore for their guidance and equipment training. I am very grateful for the support and critique over the years from my research group, including Dr. Sudip Bhattacharya, Dr. Miaolei Yan, Dr. Ratiporn Munprom, Yisi Zhu, Julia Wittkamper, Tim Hsu, Siyuan Liu, Ajay Pisat, Rubayyat Mahbub, and Saurabh Waghmare.

Lastly, I am thankful for the continuous encouragement from my family, which grew in size during my studies. I would not have reached this point without the unconditional love and support of my wife, Helen. Amidst the stresses of many moves, wedding planning,

MBA studies, and job interviewing, you displayed a sense of patience, determination, and confidence that inspired me throughout our time in Pittsburgh.

Jimmy Glickstein

August 2016

ABSTRACT

Materials for photocatalytic water splitting have been studied extensively due to the revolutionary prospect of directly using solar energy to generate hydrogen gas to power a growing global hydrogen economy. However, this research thrust has struggled to achieve efficiencies that are competitive with more developed energy technologies. One promising development in the field is the possibility to engineer photocatalytic materials to perform both water splitting half reactions selectively on different areas of their surfaces, which could result in increased efficiencies by reducing the frequency of both recombination and back-reactions. Spatially selective reactivity has been observed in a variety of materials, and can be induced by different phenomena. For instance, ferroelectric $BaTiO_3$ coated with TiO_2 has been shown to exhibit domain-specific reactivity, with oxidation and reduction reactions at the surface being separated according to the orientation of the substrate polarization. In $SrTiO_3$, a material that is nearly isostructural to $BaTiO_3$ but is not ferroelectric at room temperature, the reactivity has been shown to be termination-specific on annealed terraces with different charged atomic termination layers. While spatially selective reactivity has been clearly established in these materials, the majority of work in the literature has been qualitative in nature and the efficiencies are not well established or understood.

In this work, a finite element computational model is developed to quantify the performance of photocatalysts exhibiting spatially selective reactivity. The model is used as a tool to identify the origins of lost efficiency and to optimize the photocatalyst design through the control of key parameters. Both 1D and 2D simulations of TiO_2-coated $BaTiO_3$

were performed to improve understanding of domain-specific reactivity and to quantify and optimize the performance. Simulated one-dimensional (1D) results of individual TiO_2-coated ferroelectric $BaTiO_3$ domains are shown to be consistent with physical observations in the literature. The internal quantum efficiency (IQE) of the materials reported in the literature is estimated to be less than 1%. However, the computations demonstrate that a dramatically enhanced IQE of over 90% can be achieved independently for oxidation and reduction reactions on negatively and positively polarized domains through an increased carrier lifetime, faster reduction kinetics, and an optimized potential.

The computational model was expanded to two dimensions to assess the multidomain performance for adjacent oppositely polarized 180° domains. A wide range of near-optimal domain widths from 100 - 400 nm is shown to yield efficiencies within 10% of each other. When the domain width and potential are optimized, lateral electric fields are shown to promote the transfer of charge carriers across domain boundaries and enable an overall limiting IQE across the surface for oxidation and reduction reactions of up to 90%, nearly equaling the 1D optimal half reaction efficiencies for individual domains.

With the optimization of the potential being shown by the computational results to enable significantly higher efficiencies (without any changes to the photocatalyst itself), it is of interest to explore this effect physically. However, physical photoelectrochemical testing of coated $BaTiO_3$ photocatalysts is challenging due to the difficulties in controlling the domain structure and achieving high substrate conductivity to allow measurements through a back contact. $SrTiO_3$, on the other hand, which has been shown to exhibit termination-specific reactivity on polar surfaces (with the overall reactivity of the surface having been observed to vary with annealing environment) and has heavily doped single

crystals available commercially, is a much better candidate for physical photoelectrochemical testing. Therefore, 0.7 wt% Nb-doped $SrTiO_3$ nonpolar (100) and polar (111) single crystals were tested photoelectrochemically after being annealed in atmospheres with varying compositions to create terraces of two different crystal terminations.

Physical photoelectrochemical results reveal significant changes in the I-V characteristic with annealing environment for both crystal orientations, indicating that effects other than the electric field permeating through the semiconductor due to polar terminations may have a significant influence on the reactivity in these heavily doped materials. Additionally, the I-V curves show that, at the approximate operating potential of past photochemical tests, oxidation is the dominant half reaction averaged over the surface. However, the oxidation occurs at an extremely low efficiency that can be increased dramatically with anodic bias. Data obtained for unannealed crystals shows that the high temperature annealing itself plays a role both in delaying the onset of significant photocurrent to more anodic biases and in increasing the saturated photocurrent magnitude for all annealing environments.

Photoelectrochemical simulations, using a modified model to that of $TiO_2/BaTiO_3$ photocatalysts, indicate that the reaction kinetics dictated by the chemical composition of different terminations may play a large role in the observed variation in I-V characteristic with annealing environment for both orientations. Simulations also demonstrate that the non-uniformity of key parameters near the surface may contribute to the anodic onset shift and higher saturated photocurrent observed after high temperature annealing.

The conclusions resulting from the computational and physical photoelectrochemical characterization of these photocatalysts can be applied to similar material systems with higher achievable photoconversion efficiencies, providing a pathway to significantly increasing the competitiveness of the technology.

CONTENTS

LIST OF TABLES

LIST OF FIGURES

1 INTRODUCTION

1.1 Motivation

With an ever-growing global demand for energy, the search for a source that is abundant, renewable, and economically competitive has been the focus of a multitude of research efforts that span all aspects of science and engineering. Both globally and domestically, the primary raw materials for energy production are currently natural gas, coal, and crude oil.[1] Each of these sources, while relatively abundant, exist in limited global reservoirs and, in the case of crude oil, must be imported in large quantities into the United States. The natural distribution of crude oil reservoirs in the world has shaped much of the historical geopolitical landscape and has been responsible for a variety of international conflicts.[2] In the United States, recent discoveries of extensive shale gas reservoirs could provide a domestic energy source for decades to come that will reduce the dependence on imported crude oil. However, each of the aforementioned fuel sources produce pollutants that can drastically reduce air quality in congested areas and contribute to observed changes in the global climate.[3] One of the most promising candidates for a globally accessible and renewable fuel that produces minimal pollutants is hydrogen gas.[4]

Hydrogen has a significantly higher energy density than the fossil fuels mentioned above and, while not abundant in elemental form as a diatomic molecule, is present in many readily available compounds including water. Historically, hydrogen has been

produced by the steam reformation of hydrocarbons, which has the inherent drawbacks of producing pollutants and relying on a raw material with limited supply.[5] A much more desirable approach would be to extract the hydrogen from water and collect the diatomic gas. Devising a cost-competitive process to produce hydrogen gas from water would provide a means of creating a clean, renewable, and globally available fuel source that could be implemented in previously developed and actively researched industrial and commercial applications including fuel cells. One of the most promising candidate processes, which employs a semiconductor that can use absorbed solar energy to drive the reaction to split water and produce hydrogen, is known as photocatalytic water splitting.

1.2 Photocatalytic Water Splitting

The discovery and optimization of photocatalytic materials has been an active area of research for over four decades. The operation of such materials encompasses principles from solution chemistry, solid-state materials science, and electrochemistry. While the scientific implications of this research area are of great interest, the most exciting prospect is the ability to efficiently generate hydrogen fuel using the renewable inputs of solar energy and water, as shown schematically in Figure 1.1. Though the current political and social climates greatly favor the development of such a clean and domestic energy source,[6] the best materials developed thus far are still a long way from reaching efficiency levels that are competitive with existing technologies.[7]

Since the discovery of TiO_2 as the first stable photocatalyst,[8] along with the inherent shortcomings in its performance,[9] intensive research efforts[10] have revealed the challenge in developing a material that can absorb visible light, remain chemically stable in solution

under illumination, and split water at a competitive efficiency without significant external bias.

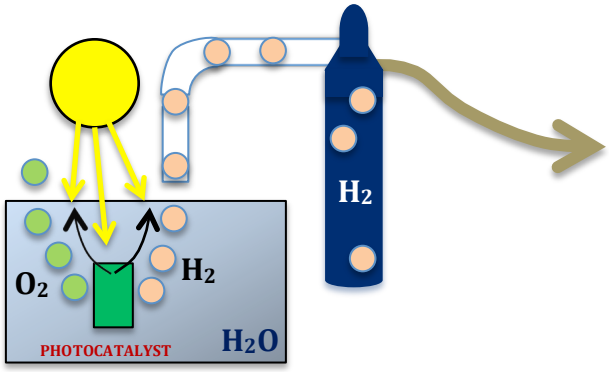

Figure 1.1: Schematic of Hydrogen Production from Photocatalytic Water Splitting

Therefore, increased performance will likely be obtained by identifying the correct material and then carefully engineering the material to optimize the performance. In order to investigate the factors that govern performance, many early studies on photocatalysts[11-13] relied on photoelectrochemical methods to identify the relative efficiencies of certain processes. These same methods enable the comparison of the photocatalytic performance to that of competing technologies, which is essential for future progress in the field.

1.3 Research Objectives

Recently published studies from our research group[14-30] have revealed the prospect of using various unique oxide semiconductors that possess internal electric fields as a means of improving the overall efficiency of photocatalytic devices by spatially separating the water splitting half reactions. These materials can be utilized in the design of both single material and heterostructured photocatalysts, and provide an alternative to co-catalysts

that may decrease the efficiency and increase the cost of the system. While spatially selective half reactions have the potential to improve quantitative performance, the majority of studies involving these materials have focused on qualitative characterization techniques, which reveal only relative reactivities within a given experiment. A more quantitative analysis of the performance of these novel photocatalytic materials may enable a significant improvement in efficiency. Additionally, a thorough understanding of the quantitative data should allow for the design of an optimized photocatalytic device to maximize efficiency.

The objective of this research is to apply photoelectrochemical characterization techniques to oxide photocatalytic semiconductors with surfaces exhibiting spatially selective reactivity in an effort to better understand and quantify the material parameters that optimize performance. These quantitative results can be used to aid in the interpretation of the largely qualitative local reactivity data that has been obtained in past works. Due to the many factors that contribute to the physical photoelectrochemical output, a finite element computational model is developed and implemented in this work to isolate key parameters dictating the device operation and to provide a platform for designing optimized devices in the future. Though planar photocatalyst geometries driven by external voltages are employed in this work, the ultimate goal is to apply the findings to the development of scalable particulate photocatalytic systems with no applied external bias. The objectives of this work are as follows:

1. Construct a computational photoelectrochemical model of photocatalytic materials.
2. Quantify the photocatalytic performance using a 1D model.

3. Identify and optimize the key material parameters that influence the performance.
4. Expand to a 2D model, re-evaluate performance, and optimize design parameters.
5. Conduct physical photoelectrochemical tests.
6. Use the computational model to enhance understanding of the physical results.

Two material systems are explored in this work to investigate these research objectives: TiO_2-coated ferroelectric $BaTiO_3$ and annealed $SrTiO_3$. $BaTiO_3$ with a thin TiO_2 coating has been shown to promote oxidation and reduction reaction products that are segregated to complementary domains. $SrTiO_3$, when (111)-oriented and annealed to form terraces with two possible terminating atomic layers, has been shown to have oxidation and reduction products localized to complementary terraces with different terminations. The domain-specific reactivity in $TiO_2/BaTiO_3$ and termination-specific reactivity in annealed $SrTiO_3$ have both been established in the literature, but have not been quantified or optimized.

$TiO_2/BaTiO_3$ heterostructures have been selected to investigate computational research objectives 1-4 due to the thorough marker reaction results in the literature and the previously demonstrated domain-specificity of reaction products on visible light absorbing ferroelectrics (increasing the potential future impact of increased understanding of ferroelectric photocatalysts). As a result of the difficulties in conducting and interpreting physical tests with $TiO_2/BaTiO_3$ (discussed in more detail in Section 2.8), annealed $SrTiO_3$ has been selected for investigating research objectives 5 & 6.

1.4 Hypotheses

Scientifically investigating the research objectives outlined in Section 1.3 requires the development of working hypotheses. The objectives are reproduced below, along with the corresponding working hypothesis to guide research into each area. For each objective, the relevant chapter in which each hypothesis is tested is noted.

1. *Construct a computational photoelectrochemical model of photocatalytic materials.*

Hypothesis: The physically observed spatially selective reactivity can be modeled using a simple semiconductor model (Chapter 4).

2. *Quantify the photocatalytic performance using a 1D model.*

Hypothesis: Oxidation and reduction reactions proceed at different rates at the illuminated open-circuit potential, limiting the overall efficiency (Chapter 4).

3. *Identify and optimize the key material parameters that influence the performance.*

Hypothesis: The performance can be optimized primarily by altering the potential (Chapter 4).

4. *Expand to a 2D model, re-evaluate performance, and optimize design parameters.*

Hypothesis: The mutidomain performance is less than the single domain performance but greater than half of the single domain performance (Chapter 5).

5. *Conduct physical photoelectrochemical tests.*

Hypothesis: The annealing environment dictates the area fractions of different terminations on the (111) surface, which in turn affects the reactivity accordingly. Reactivity of the (100) surface has no dependence on the annealing environment (Chapter 6).

6. *Use the computational model to enhance understanding of the physical results*

Hypothesis: The electric field resulting from the polarity of the termination layer is the primary factor responsible for the selectivity of reaction products to specific terraces previously observed on the (111) $SrTiO_3$ surface (Chapter 7).

These hypotheses are tested though computational and physical photoelectrochemical analyses of two photocatalytic material systems each capable of separating oxidation and reduction reactions on the surface. The result is a significant advancement in understanding the operation of photocatalytic surfaces exhibiting spatially selective reactivity and a demonstration of the tools and knowledge required to optimize future device designs. By applying the approach outlined in this work to a similar material that absorbs sunlight more efficiently, a photocatalyst may be designed that is truly competitive with existing energy technologies and has the potential to revolutionize the global energy supply.

2 BACKGROUND

2.1 Water Splitting Mechanisms

Splitting water to produce diatomic hydrogen and oxygen gases can be achieved simply by applying a sufficiently high voltage between two electrodes submersed in aqueous solution, a process known as electrolysis. The applied voltage produces high-energy electrons at the cathode and low energy vacant electronic states (electron-holes or just holes) at the anode. The minimum necessary voltage required to split water is a direct consequence of the difference in redox potential between the hydrogen reduction and oxygen oxidation reactions, as shown in Figure 2.1.

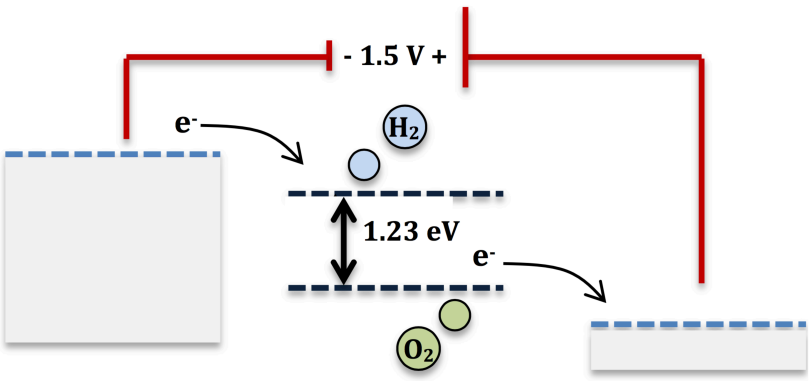

Figure 2.1: Schematic of Water Electrolysis

This difference of 1.23 eV establishes the minimum potential required by thermodynamic constraints; in practice, a voltage of roughly 1.5 – 1.6 V or greater is

needed.[12] The overall reaction potential is negative, indicating that the process increases the free energy of the system, and thus requires the input of electrical energy to produce hydrogen gas. Electrolysis relies on transforming relatively expensive electrical energy, which traditionally must be generated from coal and other fossil fuels, into the chemical energy stored in the reaction products. Although a cleaner fuel source is ultimately generated, the traditional process of producing the electricity results in a level of pollutants akin to the combustion of fossil fuels. Therefore, in this process, hydrogen gas acts as an intermediate between the input of fossil fuels and the end process, and only has utility where hydrogen gas is highly preferred or more efficient as the fuel source.

An alternative is to capture solar energy to drive the water splitting reaction. However, when pure water is illuminated with sunlight, it requires much more than the 1.5 eV needed in the electrolytic process to drive the reaction. Past studies have shown that the direct absorption of sunlight and ultimate photolysis of water requires photons with energies greater than 4.0 eV (to excite directly water molecules to the high energy triplet state that will then decompose), which corresponds to a wavelength of roughly 310 nm.[33-39] Given that the solar output spectrum ranges from roughly 350-1100 nm,[33] direct water photolysis is not expected to occur under illumination from the sun, and is thus why this decomposition is not frequently observed in nature.

While sunlight cannot directly split water, electricity can be used to drive electrolysis. Therefore, it would seem apparent that the missing material is one that can convert absorbed solar energy into electrical energy that can drive the photolysis reaction. One very developed class of devices designed to perform in this way is photovoltaics. However, many of the design parameters of photovoltaics are unnecessary costs and

complications in the application of hydrogen generation from water. For instance, the need to shuttle photogenerated charge carriers through the bulk of the material, to manufacture an electrical interface to collect these charge carriers, to sustain Ohmic losses throughout the transport of this current, to be restricted to a planar device design, and to incur the additional cost of electrode materials could all be avoided if one material could be designed that could directly transduce solar energy to perform the desired surface chemistry, without the need for an elaborate and expensive electrical intermediate. The hope for designing a very efficient process for water splitting relies on the development of this material, a photocatalyst, which can absorb visible light, generate carriers at appropriate energy levels, and can lower the activation barrier for water splitting without being consumed in any of the chemical reactions.

The idea of a material that can absorb light to produce a chemically energetic fuel source is seemingly complicated, but it has occurred in nature for over 3 billion years.[40] The process of photosynthesis harnesses the energy in sunlight to power cellular processes and form molecules that are integral to sustaining the life of a plant. The major inputs that make this process possible are water and a light-absorbing mechanism such as the thylakoid stacks of grana, which contain pigment molecules including chlorophyll. This elegant process has shaped our world and provided an atmosphere that can sustain life. However, as evidenced by the green color of plants (due to the green color of the chlorophyll pigment), plants do not absorb sunlight very efficiently and reflect light in the green portion of the visible spectrum. Photosynthesis, while using solar energy and water as the primary inputs, is too inefficient to be competitive in the global energy market and does not rapidly produce a fuel that is commercially useful in our society. To do so, a

material must be developed that can efficiently absorb solar energy and perform desirable chemistry that produces a clean, renewable, and high energy density fuel such as hydrogen.

2.2 The First Photocatalysts

The major breakthrough in the field of photocatalysis came in 1972, when Fujishima and Honda[8] designed an electrochemical cell using TiO_2 in the rutile phase as the semiconductor photoanodic electrode. It was demonstrated in further studies that oxygen was, in fact, being produced at the TiO_2 photoanode, and that the oxygen was not released from the electrode itself. Most impressively, the electrode remained chemically stable despite the Faradaic current at the surface. TiO_2 seemed to function well as a photocatalyst with two major shortcomings. The first is that the band gap energy of rutile is roughly 3.0 eV, meaning that only a small percentage of the solar spectrum (in the UV range) will be absorbed, and no visible light will be captured. Another major challenge is that TiO_2 acts only as a photoanode; an expensive platinum electrode is electrically connected as the cathode to produce hydrogen. This results in a high additional cost as well as difficulties in the scalability, limiting the potential for this cell to be a significant contributor to the global energy supply.

The discovery of the photoanodic properties of TiO_2 prompted a multitude of research efforts in the area that continue today. A few years later, $SrTiO_3$ was shown to also perform similarly to TiO_2 as a photocatalyst.[41] While both materials have been shown to split water under illumination with small to zero external electrical bias, both had also been shown to produce higher Faradaic currents with the application of an increasing anodic bias before reaching a saturated current that was limited by the irradiance.

Mavroides et al.[42] then demonstrated that $SrTiO_3$ actually performed with a higher quantum efficiency than TiO_2. This was thought to be a result of the more negative conduction band edge relative to the vacuum level (higher on an energy diagram) of $SrTiO_3$, which provides increased excess potential for hydrogen generation. A study published around the same time by Wrighton et al. presented similar findings.[43] However, the foremost limitations that were noted with the TiO_2 cell were not overcome with $SrTiO_3$; its band gap is actually larger at 3.2 eV, and it still only functioned as a photoanode, with an external connection to Pt required for the reduction half reaction.

In 1980, Sato and White[44] expanded on the work of Fujishima and Honda by compressing the TiO_2/Pt photoelectrochemical cell into a single material that could split water without any external circuit to a metal electrode. This design more closely resembles the schematic in Figure 1.1, whereby a material need only be placed in water and illuminated to produce hydrogen. Instead of a single solid electrode, a powder of TiO_2 integrated with 2 wt% Pt was dispersed in solution. The authors observed a stoichiometric production of H_2 and O_2 and found that the production approached a limiting value due to losses sustained as the reaction intermediates recombined to form water by the reverse reaction. This is one added limitation of condensing the system to a single particle; although the oxidation and reduction are spatially separated to the TiO_2 and exposed Pt areas of the surface, respectively, the reaction intermediates are still formed in very close proximity and may react before they generate the final reaction products to be collected. The higher surface area to volume ratio for powdered materials, when compared to a bulk electrode, does represent a very large improvement, though, in the expected hydrogen output per unit volume of catalyst material. The use of suspended particle catalysts, which

contain a co-catalyst such as platinum, have been the source of much further work and are the basis for many of the best performing photocatalytic systems to date.[7]

Thus far, only Ti-containing oxides have been discussed as possible photocatalytic materials. However, there are many other semiconducting compounds that have band gaps that absorb some fraction of the solar output. In fact, the efficiencies of the materials discussed thus far are severely limited by their large band gaps, which absorb only in the UV part of the solar spectrum. Figure 2.2 shows a collection of representative semiconductors along with their band gap energies and the energies of the conduction and valence band edges.[45]

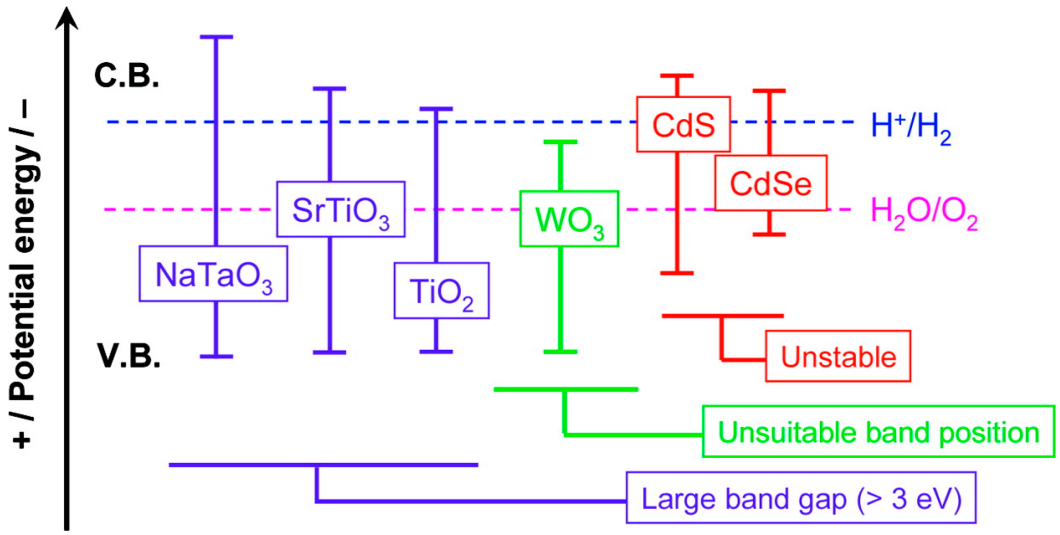

Figure 2.2: Band Gaps and Edges for Representative Semiconductors
Figure Reprinted with Permission from: K. Maeda and K. Domen: J. Phys. Chem. C, 2007, vol. 111, pp. 7851-7861.[45] Copyright © 2007, American Chemical Society

The ideal semiconductor for photocatalysis would have a conduction band edge above the H^+/H_2 level, a valence band edge below the H_2O/O_2 level, and a band gap in the range of 1.5-2.5 eV, which would allow for maximum solar absorption and sufficient energy

to split water, including the consideration of required excess potentials. Generally, a higher overpotential for the oxygen reaction can be expected, as it requires the transfer of four electrons to produce one diatomic oxygen whereas it only requires two electrons to produce hydrogen gas. Accordingly, a significant excess potential that separates the valence band below the H_2O/O_2 level is desirable. Examining Figure 2.2, it appears that one of the best candidates is CdS. However, it was discovered in the early days of research on photocatalytic materials that, with many sulfide and selenide compounds including CdS, the illumination results in corrosion of the electrode material itself. In other words, the catalyst is unstable. Upon illumination, Cd^{2+} is released into solution and a layer of sulfur coats the CdS surface, rendering the interface photochemically unreactive.[33]

Due to their chemical stability in solution under illumination and favorable kinetics for the water splitting reaction, oxide semiconductors have remained the most researched materials in the field. Many efforts have focused on improving the visible light absorbing properties of TiO_2 and related materials through impurity doping. Another popular approach is to use a sensitizing material that can absorb visible light and inject photogenenerated charge carriers into an oxide semiconductor exposed to solution. A wide variety of approaches, many well beyond the scope of the discussion here, are underway to improve the photocatalytic performance of oxides (and other materials) to enable photocatalytic water splitting to become a competitive source of useable energy.

2.3 Design Criteria for Photocatalysts

Extensive research efforts since the founding studies in the field have identified a variety of criteria[7] that must be satisfied for a single material to be an efficient water splitting photocatalyst. These criteria are listed and represented schematically in Figure 2.3.

To be economically competitive with rival energy technologies, the material must be relatively inexpensive (criterion 1). In order to maximize efficiency, it must also absorb a high percentage of the available solar energy (criterion 2). Semiconductors are a class of material in which there is great variability and control over the absorption spectrum, which is principally determined by the value of the band gap, E_g, as indicated in Figure 2.3. They are thus a natural choice for use as a photocatalyst.

1) Abundant / low production cost
2) Maximizes solar absorption
3) Separates charge carriers
4) Ideal band edge positions
5) Low overpotentials
6) Separates half-cell reactions
7) Chemically stable

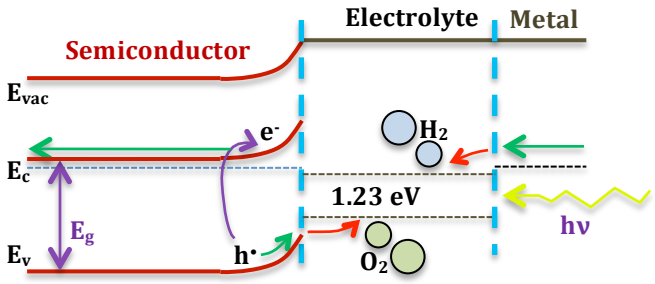

Figure 2.3: Operation of Photoelectrochemical Cell

Figure 2.3 shows an n-type semiconductor on the left in contact with an electrolyte. The band bending at the interface is the result of equilibration of the electrochemical potential of electrons in the semiconductor and in the electrolyte. A small discontinuity between the Fermi levels in the semiconductor and electrolyte is a result of the photovoltage induced in the semiconductor upon exposure to light due to a significant increase in hole concentration at the illuminated surface. Photons with energies above the

band gap energy will be absorbed, whereas those that are too low in energy will be reflected or transmitted. If the band gap energy is too high, a majority of the incident photons will not be absorbed and the energy will not be utilized. If the band gap is too low, while more of the photons of the solar spectrum will be absorbed, the energy per absorbed photon in excess of the band gap is generally lost to thermalization processes which release heat; only the band gap energy is captured for each photon. An intermediate value for the band gap energy is ideal to counterbalance these two extremes. Consideration of the solar output spectrum is required in this optimization process, depending on the band gap energies in question, since the solar photon flux varies with wavelength, with the visible light region generally having the highest photon flux.

When a photon is absorbed by the semiconductor, an electron-hole pair is generated near the surface as shown in Figure 2.3. If the light is absorbed in a region of band bending, the electrons and holes will be driven to migrate in opposite directions. This separation (criterion 3) is crucial in both shuttling charge carriers to the surface for reaction, and in avoiding recombination of the electron and hole, which represents a loss in efficiency. When the minority carriers, holes in the case of an n-type semiconductor as shown, are shuttled to the surface, they must be delivered at an energy (criterion 4) for which there is a driving force to perform the desired reaction in solution. As shown in Figure 2.3, the higher redox level in solution represents the equilibrium potential of the H^+/H_2 couple, while the level 1.23 eV below represents equilibrium of the H_2O/O_2 couple. These two half reactions represent the overall water splitting, and the 1.23 eV driving force shown in the diagram is obtained by adding the equilibrium potentials of the two half reactions as follows.[8]

Reduction Half reaction	$4H^+(aq) + 4e^- \leftrightarrow 2H_2(g)$	$E^0{}_{red} = 0\ V$
Oxidation Half reaction	$2H_2O(l) \leftrightarrow 4H^+(aq) + 4e^- + O_2(g)$	$E^0{}_{ox} = -1.23\ V$
Overall Water Splitting Reaction	$2H_2O(l) \leftrightarrow 2H_2(g) + O_2(g)$	$E^0{}_{rxn} = -1.23\ V$

The 1.23 V establishes a minimum thermodynamic driving force, but in practice, more energy is required to overcome kinetic barriers.[12] This required excess potential (criterion 5) can be seen for the anodic half reaction in Figure 2.3 as the difference between the H_2O/O_2 level and the valence band edge at the semiconductor/electrolyte interface.

An n-type semiconductor, due to its higher Fermi level relative to solution, tends to have upward band bending at the interface that favors hole transport to the surface. However, due to the very low intrinsic hole concentration, no anodic Faradaic current is expected in the dark. When the semiconductor is illuminated, the hole population near the illuminated surface increases by many orders of magnitude and, if the valence band edge position is appropriate relative to the available redox levels, the electrode will oxidize solution to form oxygen, and is thus known to behave as a photoanode. The electrons are shuttled away from the surface and travel into the bulk of the material where they can travel through an external circuit to a metallic electrode, such as platinum, and reduce H^+ in solution to form hydrogen. Therefore, in this cell, the oxygen is generated at the solution interface with the semiconductor, whereas the hydrogen is generated at the interface of solution and a metallic electrode. This spatial separation (criterion 6) reduces the probability that reaction intermediates will back-react to form water, which is thermodynamically favorable. Spatial separation thereby increases the efficiency of the reaction and allows for collection of pure hydrogen gas without oxygen contamination. In

the application to particulate photocatalysts, which is preferable when considering scalability of the technology, hydrogen and oxygen are produced in closer proximity, and back-reaction rates will likely be higher. Additionally, hydrogen and oxygen products must ultimately be separated by some mechanism for pure hydrogen to be collected.

Another very important criterion for a photocatalyst is that it remains chemically stable in solution (criterion 7). The energetic electrons and holes at the interface can react with the surface of the semiconductor that produces them, and corrode the electrode.[33] In this way, the electrode does not behave as a true catalyst and will disappear over time while also significantly lowering the efficiency of the process. This criterion limits the applicability to photocatalysis of many semiconductor material systems (like CdS) as photocatalysts, and it drives research on oxide semiconductors, which often satisfy this criterion.

These criteria establish the ideal parameters for a single material. However, individual materials are not known to satisfy these extensive requirements, and the optimally design photocatalyst will likely be composed of multiple materials. When considering a multi-component photocatalyst, certain criteria may be satisfied by one material while the remaining ones are met solely by the other. However, new criteria can also be introduced, such as the need for efficient transfer of charge carriers across a solid interface (when two solids are used to drive the two electrochemical reactions). Designing a photocatalytic system, no matter the number of components, that can separate the two half reactions, improve charge-carrier separation, reduce production costs, and have the potential to improve visible light absorption would be of tremendous value in the development of an economically competitive photocatalytic system.

2.4 Key Parameters

There are seven key criteria for a well-performing photocatalyst, which were outlined in the previous section. However, even if all or a majority of these requirements are met, there's great variability in the extent to which a given material satisfies each requirement. An ideal material is one that satisfies each requirement in a way that maximizes the efficiency, minimizes the cost, and exhibits no loss in performance over time. But there is much more to the design of a photocatalyst than simply selecting the right material. The preparation and processing of the material can greatly influence its performance and can be tailored to maximize its efficiency. In order to make informed preparation and processing decisions, and to better interpret results from photocatalytic testing, it's essential to understand what parameters influence the performance and how these parameters can be manipulated to optimize the device.

Band Gap

The band gap, E_g, of the selected semiconductor establishes a ceiling on the achievable efficiency. Unfortunately, many of the photocatalysts that best satisfy the majority of criteria in Section 2.3 fail to satisfy the condition of maximizing solar absorption. The introduction of impurities can narrow the band gap of photocatalytic oxide semiconductors but may lead to decreased performance in other areas. Figure 2.4 shows a plot, published by Murphy et al.[46] and reproduced here, of the maximum achievable (total energy conversion) efficiency for a single semiconductor (as a function of its band gap in nm). Higher efficiencies could be achieved with multiple materials with different band gap energies. The 610 nm

maximum band gap wavelength (minimum band gap energy) is determined by the thermodynamics required to drive the reaction and the minimum estimated kinetic overpotentials.[47] Different curves are shown for illumination from a xenon lamp (which is commonly used for characterization in a lab including one without a water filter which was used in the physical testing in this work) and from AM 1.5G, which is a spectrum representative of the solar output. The curves are fairly different for each source due to different relative intensities of short wavelength light compared to the intensities of longer wavelengths.

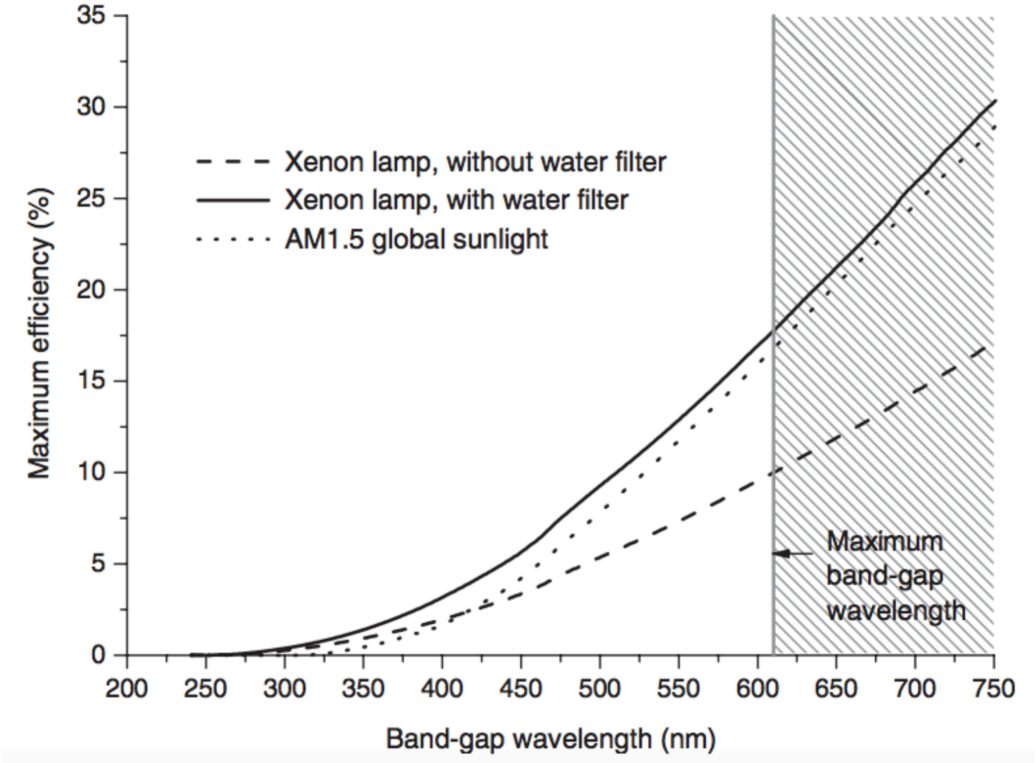

Figure 2.4: Maximum Efficiencies Determined by Band Gap for Different Illumination Sources

Figure Reprinted from International Journal of Hydrogen Energy, 31, A. B. Murphy, P. R. F. Barnes, L. K. Randeniya, I. C. Plumb, I. E. Grey, M. D. Horne, and J. A. Glasscock, Efficiency of solar water splitting using semiconductor electrodes, 19, Copyright 2006, with permission from Elsevier.[46]

To be competitive with existing technologies, researchers have set performance goals for photocatalysis that are generally between 5%[46]-10%[48] in overall efficiency of converting energy in sunlight to chemical energy stored in hydrogen. Looking at the figure, a band gap wavelength of greater than 520 nm, which equates to an energy less than approximately 2.4 eV, is needed to have any possibility of achieving 10% efficiency in the most ideal case. While the band gap is not a parameter that is altered through processing in this work, the implications of band gap selection and consideration of the band gap required to achieve competitive efficiencies are important to highlight.

Dopant Density

Consideration of the dopant density, denoted N_D when donors are the dopant as in n-type materials, is crucial to the interpretation of this work. The donor density dictates both the bulk electrical conductivity and the width of space charge region, which will be discussed below. To perform physical photoelectrochemical tests, a sufficiently high dopant density is required to conduct charge carriers through the thickness of the sample to the back contact in an effort to measure the Faradaic current at the surface. However, doping too heavily can reduce the width of band bending at the surface, which may reduce the efficiency of the device. Heavy doping may also affect charge transfer mechanisms at the surface and make tunneling more probable as a dominant mechanism.

Absorption Depth

The absorption depth represents how deep into a material photogeneration of carriers occurs. The depth can be calculated using a version of the Beer-Lambert law shown below.

$$\frac{I}{I_0} = 1 - e^{-\alpha x} \quad (2.1)$$

I = absorbed intensity, I_0 = incident intensity,
α = absorption coefficient, x = material depth

The absorption coefficient, α, is a material property that reflects the percentage of light absorbed in a given thickness of material. It is, accordingly, a function of the wavelength of the incident photons under consideration. The left side of the equation represents the fraction of incident light that has been absorbed at a given material depth, x. The value of x at which the left side of the equation is beyond a certain threshold is the absorption depth. This specific threshold is often defined as when the transmitted intensity is a factor of e^{-1} or 37% of the incident intensity.

Space Charge Depth

Ignoring complicating surface electronic effects, equilibration of bulk electrochemical potentials of electrons at the surface between the semiconductor and a solution results in an electric field that permeates into the semiconductor. The space charge depth represents the distance into the material at which an electric field exists that can act to separate photogenerated charge carriers and limit recombination, and is given by the equation below.

$$x = \sqrt{\frac{2(V_m - V_{fb})\varepsilon_0\varepsilon_r}{eN_D}} \quad \textbf{(2.2)}$$

x = space charge depth, V_m = applied potential,
V_{fb} = flat-band potential, ε_0 = free space permittivity,
ε_r = relative permittivity, q = elementary charge, N_D = donor concentration

The difference between the applied or measured voltage and the flat-band potential relative to the same reference determines the potential that must be dropped by the semiconductor. One result of this equation is that heavy doping decreases the space charge width. The space charge depth must be compared to the absorption depth in the design of a photocatalyst. Carriers that are photogenerated beyond the space charge width (plus the minority carrier diffusion length) are very likely to recombine before reaching the surface. Ideally, the space charge width should exceed the absorption depth so that all photogenerated carriers can be separated by the electric field. In this way, to maximize efficiency, the absorption depth sets a limit on the level of doping before the narrowing of the space charge width begins to result in losses.

Carrier Lifetime

For carriers that are not quickly captured by an electric field and accelerated towards the surface, they are likely to recombine before reacting at the surface. This recombination represents lost efficiency in the device as carriers absorb solar energy but release the energy as heat through the recombination process. The parameter governing how quickly these carriers recombine, and in turn their

probability of diffusing or drifting to a reaction site, is the carrier lifetime. The carrier lifetime represents the average time between photogeneration and recombination. For a very long lifetime (such as 10^{-6} s), carriers generated beyond the space charge region have a high probability of diffusing to the space charge region and being collected before recombining. However, for more moderate lifetimes (such as 10^{-9} s), common in the semiconductors relevant to this work, the majority of carriers generated significantly beyond the space charge depth will be lost to recombination.

Reactivity Parameter

The parameters above have dealt primarily with the delivery of photogenerated carriers to the surface, with the assumption that this is the limiting process and that carriers at the surface will rapidly undergo appropriate chemical reactions. In reality, the rate of reaction may be slow compared to the rate of carrier delivery. From electrochemical theory, the kinetics of the surface reactions can be described by the Butler-Volmer Equation.[49-50] However, in this work, the semiconductor interface with solution is modeled in simulations as a Schottky contact with charge transfer governed by thermionic emission. In this context, the simulation parameter that governs the rate of reactivity is best represented by the effective Richardson constant. In thermionic emission theory, the material-dependent Richardson constant is a leading coefficient in the expression for thermionic current that governs the rate of emission so long as a sufficiently high concentration of carriers is present. In this way, the Richardson constant is used in the simulations as a general 'reactivity parameter' which consolidates a variety of factors related to how readily

carriers at the surface react. A more detailed discussion of this parameter can be found in Section 3.2.

Applied Voltage

The applied voltage is very easily controlled in photoelectrochemical testing and has a dramatic influence on the observed current. Simply dropping a semiconductor into a solution and allowing time for equilibration at the surface establishes an open-circuit potential relative to a reference that is determined by the electrochemical potential of the solution. An applied voltage acts to move the Fermi level of the semiconductor, separating it from the solution Fermi level. In practice, a voltage is applied by a potentiostat between the sample, which is designated as the working electrode, and a reference electrode. The voltage alters the direction and degree of band bending at the surface, as well as the depth of the space charge layer. In this way, applying a favorable bias voltage can result in a massive increase in photocurrent output. However, applying a bias is an expenditure of energy, and must be accounted for when evaluating the overall efficiency of the process. In the application of developing a particulate photocatalyst with no external connection to a potentiostat, small potential shifts can be achieved by altering the solution (pH, concentration, or redox species). Variations in the electrochemical potential of the solution can also shift the redox levels for water splitting, and could therefore effectively change the value of the reactivity parameter introduced above.

Flat-band Potential

The flat-band potential, E_{fb}, is the potential that must be applied relative to the reference electrode at which there is no band bending near the surface of the semiconductor. The flat-band potential can be measured experimentally, or can be calculated if certain material parameters are known. In 1978, Butler & Ginley[51] published an equation, reproduced below, that related the measureable flat-band potential of a semiconductor to its electron affinity and the potential across the Helmholtz layer.

$$E_a = E_0 + E_{fb} + \mu + V_H \quad \textbf{(2.3)}$$

E_a = electron affinity, E_0 = reference potential, E_{fb} = flat-band potential,
μ = Fermi level separation from E_C (n-type), V_H = Helmholtz potential

Due to the dependence of the Helmholtz voltage on the solution pH, the flat-band potential will be different for a given material in different electrolytes. The voltage value of E_{fb} is measured relative to a reference electrode, which dictates the value of E_0. Therefore, when reporting a flat-band potential, it must always include a pH of the measurement and the reference electrode that is being used. Generally, for an n-type semiconductor, the oxidation photocurrent increases significantly for potentials anodic of the flat-band potential. Thus, it is important to know E_{fb} in designing a photoanode to ensure that the operating potential is significantly positive of the flat-band condition.

Efficiency

The parameter that must be maximized is represented by the QE (quantum efficiency), which has units of electrons/photon. Two version of the quantum efficiency are used in this work, the EQE (external quantum efficiency) represents the fraction of incident photons that generate a charge carrier that reacts at the interface with solution. The IQE (internal quantum efficiency) is calculated in the same manner as the EQE but rather than the incident photon flux being used, it calculates the fraction of absorbed photons that generate charge carriers that participate in reactions.

$$QE = \left|\frac{J}{\varphi_{ph}}\right| * 100\% \qquad \textbf{(2.4)}$$

J = photogenerated current (expressed as elementary charge flux),
Φ_{ph} = photon flux,

The EQE and IQE are both calculated from Equation 2.4 by inputting either the incident or absorbed photon flux, respectively. To maximize the internal efficiency of the photocatalyst, a high minority carrier diffusion length, a high space charge width, and a relatively narrow absorption depth are ideal in accordance with a simplified model developed by Gärtner.[52] One important factor not considered in the QE calculation is any applied voltage. As discussed previously, the ideal operating voltage may not coincide with the open-circuit voltage. In this case, a measure of efficiency must be used which allows the evaluation of the optimal potential which maximizes photocurrent output while limiting the excess energy injected into the system by the applied voltage. These effects are combined in the

equation for the overall efficiency, or photoconversion efficiency (assuming 100% faradaic efficiency), shown below.[53]

$$\varepsilon_0 = \frac{(1.23 - V_{bias}) * J}{P} \quad \textbf{(2.5)}$$

J = photogenerated current, P = incident power density of illumination,
V_{bias} = potential difference between working and counter electrode

This photoconversion efficiency, ε_0, is the most relevant metric when considering the performance relative to competing technologies. QE, on the other hand, provides insight into how well the device, for a given material and operating potential, converts incident photons into reacted charge carriers. The primary difficulty in computing the photoconversion efficiency is determining the value of V_{bias}, but this value is often approximated as the voltage between the working and reference electrode controlled in photoelectrochemical tests. Similar adjustments can be made to other efficiency measures to compensate for the applied bias.

A number of key parameters govern the theoretical understanding of the operation of photocatalytic materials, and are used frequently to explain various experimental observations in the field. As mentioned previously, the majority of research in the field has been focused on oxide photocatalysts due to their superior chemical stability under illumination. However, the O 2p orbitals characteristic of these materials result in a low valence band edge potential, which often leads to a wide band gap that cannot absorb visible light. As indicated by Figure 2.4 and the subsequent discussion, there is only a small

range of band gaps that are small enough such that the achievable efficiency is sufficiently high to be competitive but are not so small that they do not possess enough energy to drive the water splitting reaction. Even if a material possesses a band gap within this tight region, there is a further restriction that the band edges must be appropriately positioned on an energy scale to drive both half reactions. Given these very stringent requirements, and the fact that even for a material with a suitable band gap, the efficiencies from Figure 2.4 are maximum efficiencies assuming perfect capture and performance of the device, it is imperative that the device operation is well understood in terms of the key parameters so that the performance may be optimized to approach the maximum efficiency.

2.5 Perovskite Photocatalysts

One of the most well studied groups of oxide photocatalytic materials since the first years of research in the field have been perovskite semiconductors. Perovskite oxides ideally exhibit a cubic crystal structure ($Pm\bar{3}m$) with the general chemical formula ABO_3 where A and B denote larger and smaller cations, respectively. Figure 2.5 shows the cubic perovskite structure with BO_6 octahedra positioned at the corners surrounding the A-site atom at the center (red atoms represent the oxygen at the vertices of the octahedral).[52] The A-site metal cations (yellow in Figure 2.5) have 12-fold oxygen coordination while the B-sites have 6-fold oxygen coordination (represented by the blue octahedral in Figure 2.5). In practice, perovskites generally diverge from this ideal case and exhibit distortions in the cubic symmetry due to the radius and valence of the metal cations present. These distortions lead to variations in the band structure and can lead to new functionalities,

including ferroelectricity. The breadth of properties available within perovskite materials can be selectively harnessed to improve photocatalytic efficiencies.

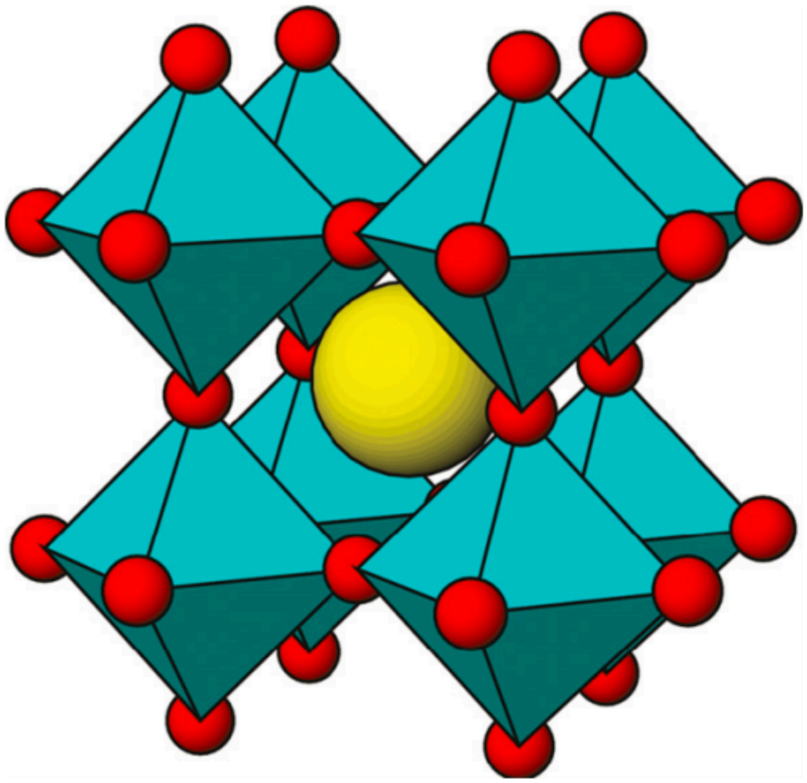

Figure 2.5: Cubic Oxide Perovskite Crystal Structure
Figure Reprinted from Prog. Nat. Sci., 22, J. Shi and L. Guo, ABO3-based photocatalysts for water splitting, 592-615, Copyright (2012), with permission from Elsevier.[52]

Another benefit of perovskites, and a reason why they have been the subjects of so many studies in the field of photocatalysis, is the versatility of the structure to accommodate different metal cations (and hence exhibit tailorable properties). Select compositions can even give rise to visible light absorbing semiconductors such as those shown in Figure 2.6 (next to the well studied TiO_2), which are ultimately desirable in the pursuit of a high-efficiency photocatalyst.[55] Of the materials shown in Figure 2.6, $PbTiO_3$ and $BiFeO_3$ are ferroelectric while the others are not, with the difference being simply

attributable to the atomic positions in the crystal at room temperature depending on the composition.

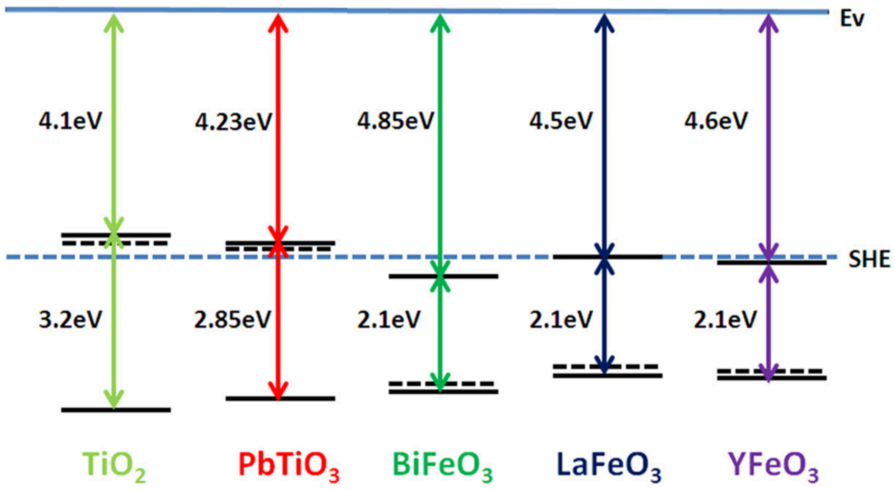

Figure 2.6: TiO_2 and Select Narrow Band Gap Perovskite Band Edge Positions
Figure Reproduced from [55].

One unique characteristic of many titanium-based perovskites, in particular, is a conduction band edge that is positioned high enough to reduce hydrogen without external bias or the introduction of a co-catalyst. This became evident when Mavroides et al.[42] demonstrated the superior photocatalytic properties of $SrTiO_3$ and observed higher performance than that of TiO_2, which has a slightly lower conduction band edge. The conclusions from this paper[42] discuss how the quantum efficiency could be improved further by preparing a material with a more favorable flat-band potential, a smaller band gap, and a deeper space charge layer. These key parameters, and others, have been the guiding determinants of performance over decades of photocatalysis research.

Since the initial 1976 study on $SrTiO_3$, various studies have focused on enhancing the visible light absorption through impurity doping[56-62] and the incorporation of various

co-catalysts[63-67] to increase the photocatalytic performance. A number of studies have also investigated the potential improvement in efficiency when $SrTiO_3$ was paired with visible light absorbing materials as part of a heterostructured photocatalyst.[68-74] Another perovskite with a nearly identical conduction band edge and band gap as $SrTiO_3$, but that is ferroelectric at room temperature, is $BaTiO_3$. $BaTiO_3$ is one of the best-known ferroelectrics and is a well-studied photocatalyst.[70] Similar to $SrTiO_3$, the photoelectrochemical response of $BaTiO_3$ electrodes were first studied in 1976,[71] and subsequent studies have been targeted at increasing the visible light performance through heterostructures and doping.[72,73]

For both $SrTiO_3$ and $BaTiO_3$, a multitude of results in the literature have established their material characteristics and demonstrated enhanced properties including increased visible light absorption. However, a computational analysis of the combined effect of optimizing a variety of the parameters outlined in Section 2.4 on the photocatalyic performance of these materials has not been done. It is crucial both in the case of well-developed systems and upon the discovery of new catalysts that some consideration of optimization be conducted to evaluate the maximum achievable efficiencies and the feasibility of reaching them.

2.6 Motivating Experiments

Many studies on n-type photocatalysts, such as the perovskites relevant to this work, report only photoanodic currents representing the photogeneration and reaction of energetic holes (minority carriers) at the surface. Photoanodic performance is generally characterized with oxidation occurring on a test material and reduction occurring at a

counter electrode. However, in the ultimate application of a powdered water-splitting photocatalyst, the device must perform the hydrogen reduction reaction on the surface as well. In studies that test n-type oxide photocatalysts that can operate independently of any external circuit, platinum is generally incorporated into the light-absorbing material or decorated on the surface to provide a pathway for the reduction half reaction. However, platinum is expensive and has been shown to produce high losses due to the back-reaction of the hydrogen and oxygen reaction intermediates. It is thus of interest to investigate other methods of controlling the sites where reduction occurs at the surface. Other high performance co-catalysts have been developed in addition to platinum, including Rh,[75,76] RuO_2,[77,78] and NiO.[67] While both RuO_2 and NiO exhibit greatly reduced back-reaction rates relative to Pt,[79] and NiO is a much more affordable co-catalyst, problems still exist. There may be losses from co-catalysts due to shielding a portion of the surface from light absorption and carrier generation. Since they also block surface reaction sites for the counter reaction, an optimal surface coverage of co-catalyst material exists, that balances the two overall reaction rates, which is found empirically. Also, the charge carriers reacting in the co-catalysts originate from other areas of the photocatalyst where light is absorbed. Having an area on the surface that favors reduction, is also absorbing light, and can transfer photogenerated holes to areas favoring oxidation may greatly improve the efficiency of the process.

While improving the efficiency and lowering the cost of the mechanism that promotes reduction on the surface is an important research direction, it is necessary to be mindful that a promising approach should not greatly limit potential improvements in other areas. The most crucial area related to oxide semiconductor photocatalysts is the

ability to absorb visible light. Developing a system which can separate the two half reactions, improve charge-carrier separation compared to TiO_2 alone, reduce production costs, and still have the potential to improve visible light absorption would be of tremendous value in the development of an economically competitive photocatalytic system.

Ferroelectric Polarization

In 2001, Giocondi and Rohrer[15] demonstrated spatial selectivity of a reduction reaction on the surface of a $BaTiO_3$ polycrystal that appeared to coincide with the ferroelectric domain structure. Atomic force microscopy (AFM) was used to reveal the ferroelectric domain structure, which displays contrast because of surface relaxation as the material is cooled below its Curie temperature after annealing. The samples were illuminated using a 300 W Hg lamp while immersed in a $AgNO_3$ solution. This type of experiment can be referred to as a 'silver marker reaction' (see Section 2.7 for a more detailed description of marker reactions) because if Ag^+ ions in solution are reduced by the material, solid silver will be deposited very close to the reaction site. AFM can then be used, after allowing the reaction to proceed for some time, to reveal the locations where a reduction reaction occurred, along with the relative activity of the surface based on the amount of deposited silver. The primary limitations of this method are that it does not provide a quantitative analysis of the reaction rate and that there may be differences in the occurrence of the Ag reduction reaction compared to the hydrogen-producing reaction that is ultimately desired.

Despite the promising demonstration of domain specific reactivity on the surface of $BaTiO_3$, Ba leaching has been shown to dissolve the material over time in aqueous solution.[80-82] In 2006, Burbure, Salvador, and Rohrer[17] expanded on the previous work and

performed the silver marker reaction on thin TiO_2 films coating polycrystalline $BaTiO_3$ substrates. The results closely resembled those that were found on the bare ferroelectric surface, even though the 10 nm TiO_2 overlayer is not ferroelectric. For a thicker 100 nm film, the Ag deposits did not correspond as closely to the domain stripes as they did in the case of the thinner film. It was hypothesized that the underlying ferroelectric exhibits a field effect that influences the chemistry at the surface, and this effect is limited as the thickness of the film increases and the interface polarization is shielded away from the film surface.

In 2010, further experiments from the same authors[21-22] established the relationship between the domain polarization and the sign of the Faradic current at the surface of the film. In this set of studies, $BaTiO_3$ with a 15nm TiO_2 film was exposed to a $Pb(C_2H_3O_2)_2$ solution that, when oxidized, deposited PbO_2 on the surface. Figure 2.7 shows AFM images of these samples where, in 'a' and 'c', the white contrast represents PbO_2 on the surface.[21] The patterns of PbO_2 photodeposited on the TiO_2-coated $BaTiO_3$ resembled the underlying substrate domains, which are shown in 'b', after the entire film was polished away.

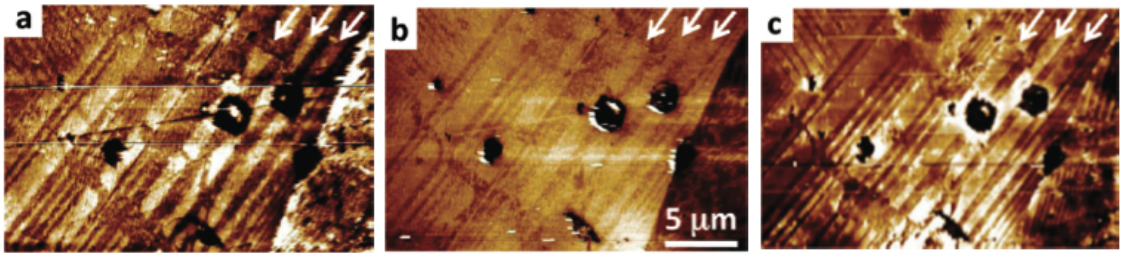

Figure 2.7: AFM of TiO_2 on $BaTiO_3$ & Bare $BaTiO_3$ Substrate
Figure Reproduced from [21].
(a) 15 nm TiO_2 on BaTiO3 exposed to $Pb(C_2H_3O_2)_2$ **(b)** TiO_2 film polished away **(c)** Bare $BaTiO_3$ exposed to $Pb(C_2H_3O_2)_2$

The pattern of PbO_2 photodeposited on the bare substrate is shown in 'c', and it can be seen that the domains covered with PbO_2 are identical between the uncoated 'c' and coated 'a' ferroelectric. It was suggested by the authors that this was a strong indication that the carriers are being generated in the substrate and travel through the film to react on the surface. However, the mechanism of this transfer and the characteristics of the energy band structure are not fully understood.

Control of the surface reactivity using the ferroelectric domain polarization represents an alternative to the addition of co-catalysts to generate spatially selective reactions on a single material. The thin TiO_2 film protects the less stable $BaTiO_3$ and yields surface states with better catalytic properties, while the substrate absorbs the majority of light and dictates the spatial location of half reactions at the surface of the film. Similar oxide heterostructure photocatalysts have been shown to not only separate half reactions, but also to perform better than either of their constituent materials alone.[83,84] The speculative reasons for better performance from a heterostructure include better charge-carrier separation, broader solar absorption, and improved surface band edge energies.

Polar Surface Terminations

Ferroelectric $BaTiO_3$, which was the focus of the studies above, is virtually isostructural with $SrTiO_3$, with the difference being that $SrTiO_3$ is not a ferroelectric at room temperature. This establishes $SrTiO_3$ as an excellent material system in which to investigate internal fields caused by phenomena other than ferroelectricity that might similarly influence reactivity. A study in 2003 by Giocondi and Rohrer on the (100) $SrTiO_3$ surface[16] revealed that the lack of ferroelectric domains at room temperature results in no observable spatial selectivity of reaction products when probed using the marker reactions

that the researchers employed previously on $BaTiO_3$. The AFM results in Figure 2.8 reveal that marker reaction products for reduction and oxidation appear to be deposited sporadically across the surface for both reaction in $AgNO_3$ (shown in Figure 2.8b) and reaction in $Pb(C_2H_3O_2)_2$ (shown in Figure 2.8c), with the silver products being much more prevalent.[16]

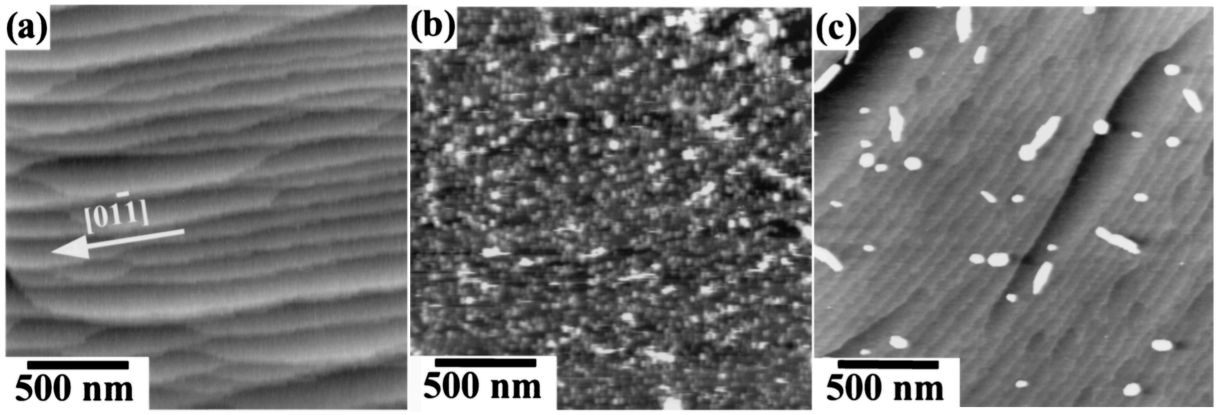

Figure 2.8: AFM of Annealed (100) $SrTiO_3$ Single Crystal
Figure Reproduced from [16].
(a) Unreacted **(b)** After illumination in $AgNO_3$ solution **(c)** After illumination in $Pb(C_2H_3O_2)_2$ solution

The visible segmentation of the surface, clearly visible in Figure 2.8a, represents different crystal terraces created by extended annealing at 1250 °C. The terraces, which appear somewhat analogous in the AFM to ferroelectric domains, are separated by steps of varying multiples of atomic planes in the crystal structure.

When an identical set of experiments was repeated in the same study on (111) $SrTiO_3$ single crystals, spatially selective reactivity reminiscent of that observed on the ferroelectric $BaTiO_3$ surface was observed. Furthermore, the reactivity seemed to be localized to specific terraces on the surface in the same way that $BaTiO_3$ had exhibited differential reactivity for different ferroelectric domains.

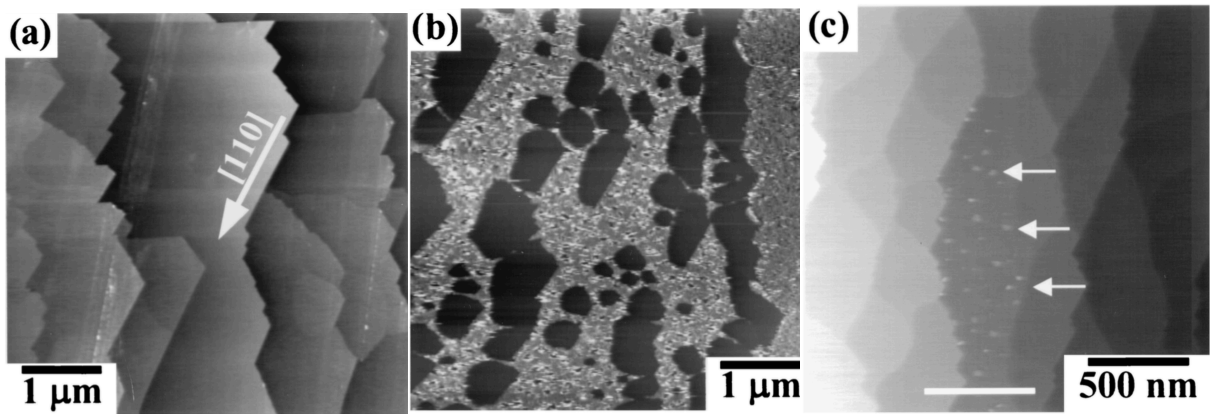

Figure 2.9: AFM of Annealed (111) $SrTiO_3$ Single Crystal
Figure Reproduced from [16].
(a) Unreacted **(b)** After illumination in $AgNO_3$ solution **(c)** After illumination in $Pb(C_2H_3O_2)_2$ solution

As shown in Figure 2.9, a majority of the terraces appear to be active for the silver reduction reaction (b) whereas only a minority of terraces are active for lead oxidation (c).[16] An analysis of the step heights of reactive and unreactive terraces for lead oxidation normalized as multiples of the spacing between atomic layers in the crystal structure is shown in Figure 2.10.[16]

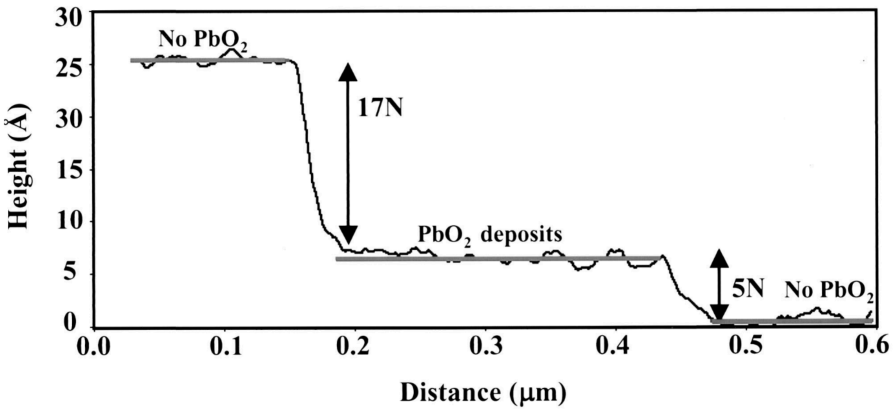

Figure 2.10: Height Profile for (111) $SrTiO_3$ after Illumination in $Pb(C_2H_3O_2)_2$ Solution
Figure Reproduced from [16].

Considering the cubic perovskite crystal structure of $SrTiO_3$, a separation by an odd multiple of steps represents a change in the termination composition while an even multiple preserves the termination composition. The conclusion is that reactivity appears to be influenced by the composition of the termination layer in the crystal structure at the surface.

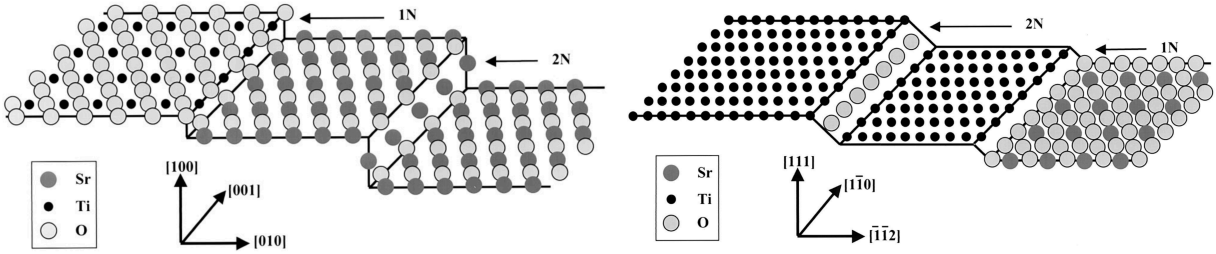

(a) **(b)**

Figure 2.11: Surface Terminations Separated by Various Step Heights
Figure Reproduced from [16].
Schematics shown for $SrTiO_3$ single crystal surfaces with **(a)** (100) and **(b)** (111) orientations. The multiples of atomic layers separating terraces on the surface are indicated. Terraces separated by odd multiples retain the same surface termination, while terraces separated by even multiples have different terminations.

Examining the crystal structures for the (100) and (111) orientations of $SrTiO_3$ in Figure 2.11 reveals two different possible compositions of bulk-like termination layers for each orientation.[16] For the (100) surface, the terminating atomic plane can be composed of TiO_2 or SrO, both of which are charge neutral. However, for the (111) surface, the possible terminating layers consist of Ti^{4+} or SrO_3^{4-}, both of which are highly polar. While the overall (111) crystal is approximately neutral due to a balancing of the two charged planes, the surface will be locally charged depending on the composition of the terminating layer.

This fundamental difference between nonpolar and polar terraces for (100) and (111) $SrTiO_3$ surfaces, respectively, was thought to be responsible for the extent of reaction

selectivity observed experimentally for the two orientations. Giocondi and Rohrer[16] also tested the (110) $SrTiO_3$ surface, which exhibits two distinct polar terminations, and observed spatial selectivity as expected but an overall greatly reduced reactivity relative to the (111) surface. While it's evident that the composition of the termination determines the reactivity of the surface, it is unknown which orientation favors which half reaction. It is also unknown precisely how the termination influences the reactivity. The mechanism that was assigned to the relationship between termination and reactivity was that the polar termination produces an electric field that permeates through the semiconductor and dictates which charge carriers are delivered to the surface for reaction, similar to the theorized source of spatially selective reactivity in ferroelectric $BaTiO_3$.

New findings from Zhu, Rohrer, and Salvador[32] have expanded upon the 2003 study by Giocondi and Rohrer. Single crystals of (111) $SrTiO_3$ were annealed at the same high temperature from the previous study but in various annealing environments. Crucibles, which hold the samples during annealing, were pre-annealed with powders of $SrTiO_3$, TiO_2, or other substances before being annealed with the $SrTiO_3$ samples. The logic behind this pre-annealing was that, when the crucible is ultimately heated to the annealing temperature with the sample, any powders present from the pre-annealing will be released and alter the environment at the surface during terrace formation. In other experiments, mixtures of $SrTiO_3$ and TiO_2 powders were added to the crucible during annealing of the sample itself. In the past study by Giocondi and Rohrer,[16] no pre-annealing of the crucibles or annealing in the presence of powders was done; the samples were simply annealed in air inside a crucible.

Characterization of (111) samples annealed in different pre-annealed crucibles by the silver reduction marker reaction and subsequent AFM has shown spatial selectivity of the reactivity to different terminations in all cases, with some annealing environments resulting in a higher fraction of the surface being reactive than others. Specifically, samples annealed in crucibles that have been pre-annealed in TiO_2 showed the smallest fraction of the surface reactive for silver reduction. Samples annealed in crucibles that were pre-annealed in $SrTiO_3$ and ones that were annealed in crucibles that had not been pre-annealed at all showed comparable fractions of the surface active for silver reduction, both of which produced a higher reactive fraction of the surface than in the TiO_2 pre-annealed crucible case. The proposed explanation for this result is that different annealing environments favor the formation of different terminations and so, for a given annealing environment, the observed dominant reactivity will depend on the reactivity of the favored termination. In this way, if one assumes that one termination composition is active for silver reduction while the other is not, the fraction of the surface area of each termination produced by annealing in each environment directly corresponds to the observed fraction of the surface that is reactive. The mechanism by which the powders present during annealing influence the surface chemistry has been proposed by Zhu, Rohrer, and Salvador as follows:[32] excess TiO_2 in the crucible reacts with high pressure SrO vapor in the furnace, establishing a concentration gradient that drives increasing amounts of SrO from the surface for increasing ratios of TiO_2 in the crucible. In this way, the surfaces of pre-TiO_2 annealed samples are expected to be Ti-rich. Adsorbates result in a less positive measured surface potential on a higher percentage of the surface, which is thought to result in a surface with more photoanodic terraces.[32]

Zhu, Rohrer, and Salvador have also found that, if a very thin (<10nm) TiO_2 film is deposited on the (111) $SrTiO_3$ surface, the nature of the spatial selectivity of reactions is preserved. This result suggests that, for the $SrTiO_3$ sample used in the study, the local electric field generated by the polarity of the terminating atomic layer and its effect on the movement of charge carriers is likely the primary factor in determining reactivity, and not the termination-dependent chemistry of the surface and its interaction with species in solution. Since the TiO_2 film coats the $SrTiO_3$ surface and the varying polar terminations are no longer in contact with solution, the proposed explanation is that the electric fields from the terminating layer influence the transfer of charge carriers which transport through the thin film and react at the film surface in qualitatively the same way that they would if no film were present.

Summary

The domain-specific reactivity on coated ferroelectric $BaTiO_3$ and the termination-specific reactivity on annealed $SrTiO_3$ have been qualitatively demonstrated by marker reactions. The following section provides a detailed description of the benefits of this characterization method, as well as the limitations. The fixed key parameters (like the potential) and lack of reliable quantitative output from the marker reactions used in these motivating experiments presents the opportunity for a different approach to significantly enhance the understanding of photocatalysts exhibiting spatially selective reactivity.

2.7 Marker Reactions

Marker reactions, which have thus far been the dominant characterization method in the study of photocatalytic perovskite surfaces with spatially selective reactivity (see Section

2.6), focus on the study of a single half reaction at a time on a given surface. They function by introducing a redox species in solution which will both be favored over one of the water splitting half reactions, and will also result in the deposition of a solid product on the surface which can be imaged using AFM. By measuring step heights on the surface before and after exposure to the marker reaction solution, AFM can detect the precise areas of the surface on which the marker reaction has proceeded. Marker reactions are distinctly different than the photoelectrochemical methods described in Chapter 3. To begin with, the sample is not connected to any power source and instead exists in an open-circuit condition. The operating potential can be measured and mimicked using a potentiostat in the photoelectrochemical setup, but marker reactions also lack a counter electrode to perform the non-dominant half reaction. Therefore, the slower half reaction dictates the overall reaction rate in marker reaction experiments.

When a reduction marker reaction product decorates the whole surface, the necessary interpretation is that oxidation must occur so readily on the surface to allow for so much reduction. When and where oxidation occurs, electrons cannot escape through a back contact to retain charge neutrality and so it is thought that they ultimately react nearby on the surface to preserve the charge balance. If only certain areas are decorated with a reduction marker reaction product, then it is possible that the areas with no reaction products are more active for oxidation, and reduction on the decorated areas of the surface preserves the charge balance. Since the marker half reactions are designed to occur more readily than the water splitting half reaction of the same redox character, it is generally assumed that they are a good proxy for a specific half reaction for water splitting.

The marker reactions of most relevance to this work are the Ag^+/Ag reaction[99,100] for reduction, which occurs in 0.115M $AgNO_3$ solution,[16] and the Pb^{2+}/PbO_2 reaction[101,102] for oxidation, which occurs in 0.0115M $Pb(C_2H_3O_2)_2$ or 0.115 M $Pb(NO_3)_2$ solutions.[16] The chemical reactions that result in solid products of Ag and PbO_2 are shown below.

$$Ag^+ + e^- \leftrightarrow Ag(s) \quad \textbf{(2.6)}$$

$$Pb^{2+} + 2H_2O + 2h^+ \leftrightarrow PbO_2(s) + 4H^+ \quad \textbf{(2.7)}$$

The silver reduction redox level is positioned at 0.8 V vs. NHE[103] and the lead reaction redox level is at 1.45 V vs. NHE.[104] This places the silver reduction reaction 0.8 eV below the hydrogen reduction redox level, which means that more excess potential is available for conduction band electrons to participate in the silver reaction. The lead reaction, on the contrary, is positioned slightly below the oxygen oxidation level, meaning that holes in the valence band have slightly less excess potential to participate in the lead oxidation reaction relative to the oxygen gas generating reaction. The consequence of this is that, from purely a consideration of the excess potential, the lead reaction may be slower than water oxidation, which has a larger excess potential. However, which reaction dominates depends on the precise distribution of states in the valence band in question, their overlap with the redox states in solution, and the kinetic processes for the given reaction.

Despite some complexities in the interpretation of marker reaction results, they provide valuable information that cannot be obtained from physical photoelectrochemical testing alone. When studying surfaces with spatially selective reactivity, marker reactions

are ideal in determining spatial selection of reaction products, as well as the relative percentage of the surface area active for specific half reactions. Without this information, it is very difficult to say if a given reactive surface has a small area fraction of the surface favoring one reaction at a high rate or a large area fraction favoring that reaction at a comparably low rate, both of which could result in the same net total measured current. Only with the full integration of knowledge gained from multiple characterization methods can a significant advancement be made in the understanding of photocatalytic surfaces exhibiting spatially selective reactivity.

2.8 Material Selection and Parameters

Justification

The design of photocatalysts that can perform both of the required water splitting half reactions at different areas on the surface is a crucial research area for the design of optimized photocatalysts for solar hydrogen production. Improving the efficiency of the overall photocatalyst and allowing for an extension to materials that absorb visible light are both ultimately needed, and this thesis will focus on the former.

A multitude of studies in the last 15 years have firmly established the ability of ferroelectric oxide semiconductors to exhibit spatially selective reactivity depending on the domain polarization. In particular, studies produced from our research group have investigated reactivity by employing marker reactions and using AFM to analyze the surface. These studies, specifically on $BaTiO_3$ with and without deposited layers of TiO_2, have established that the orientation of the polarization of a ferroelectric domain on the surface can strongly influence the reactivity at the surface and that carriers can be

transferred through a thin film to reveal the same selectivity as the bare substrate. Similar studies have shown that the same two findings can be observed for a visible light absorbing ferroelectric material such as $BiFeO_3$ with thin TiO_2 films.[23] $BiFeO_3$ is a material with one of the most narrow band gaps among the commonly used and fabricated ferroelectrics. From its nearly ideal band gap of approximately 2.1 eV, the maximum achievable photoconversion efficiency is around 15%. However, the material parameters of $BiFeO_3$ are not as well researched as $BaTiO_3$, and so $BaTiO_3$ coated with TiO_2 is a better model system to use in the computational model. Therefore, TiO_2-coated $BaTiO_3$ was selected as the material system for computational investigations into research objectives 1-4 (from Section 1.3).

One drawback of using ferroelectrics is the limited number of available materials with relatively narrow band gaps like $BiFeO_3$. In addition, it is difficult to test $BaTiO_3$ using physical photoelectrochemical methods to compare directly to the computational results. A high dopant density is required (as described in Section 3.1) which can be difficult to achieve in ferroelectric $BaTiO_3$. Additionally, physical photoelectrochemical results output an average of the entire surface. Therefore the surface domain structure must be carefully controlled to more directly interpret the results, which can be difficult to achieve. A different material is therefore desirable to conduct a direct comparison between physical and computational photoelectrochemistry.

The combined findings of Giocondi and Rohrer and Zhu, Rohrer, and Salvador have revealed that orientations of $SrTiO_3$ with polar terminations exhibit spatially selective reactivity similar to that observed for ferroelectric materials, that this reactivity appears to be preserved even with a thin TiO_2 film, that the percentage of the surface that is reactive

depends on the annealing environment, and that the selectivity is absent for orientations with nonpolar terminations. The ability to control the area fractions of each termination by annealing environment and the increased flexibility of material selection to those that need not be ferroelectric renders materials with polar surface terminations a very promising direction for investigations in photocatalyst design.

The ability to control the terminations on the surface with annealing environment is especially important given the goal of characterizing the samples using photoelectrochemical methods. Both (100) and (111) $SrTiO_3$ surfaces are investigated to isolate the effect of the polar terminations, and to distinguish these effects from those that are universally present on $SrTiO_3$ surfaces. Three different annealing environments in air and in the presence of crucibles pre-annealed with powders of $SrTiO_3$ and TiO_2 are used to provide a spectrum of termination composition area fractions to aid in the interpretation of their net effect on the surface average current output from the photoelectrochemical testing.

This level of the control over the surface terminations makes $SrTiO_3$ an excellent candidate for a direct comparison of physical and computational photoelectrochemistry. The one additional requirement for physical testing is a high substrate conductivity, which is possible using commercially available 0.7 wt% Nb-doped $SrTiO_3$. However, it is important to note that the literature marker reaction results showing spatially selective reactivity were done with undoped samples. Using heavily doped samples may change the performance significantly by limiting the effect of internal fields and shrinking the space charge region. However, it is required to conduct a direct physical and computational comparison. To determine whether or not spatially selective reactivity is still possible in

samples doped this heavily, a marker reaction experiment was conducted, as described in Section 6.4. Some spatial selectivity was observed on the surface of heavily doped samples in a similar fashion to that observed on the undoped samples. Therefore, $SrTiO_3$ can be used to correlate photoelectrochemical characterization to marker reaction chemistry, and has been selected in this thesis as the material for testing research objectives 5 & 6 (from Section 1.3).

Material Properties

$BaTiO_3$ coated with thin TiO_2 films have been selected as the primary material system for computational modeling in this work. Anatase TiO_2 was selected because it was the phase found in the experiments described as motivating the computational work, and because it has superior photocatalytic performance compared to rutile.[105] The relevant material properties for modeling $BaTiO_3$ and TiO_2 are summarized in Table 2.1.

The focus for the direct comparison of physical and computational photoelectrochemistry in this work is on $SrTiO_3$ (100) and (111) surfaces. In order to test bulk samples electrochemically with only a single orientation exposed to solution, single crystals were obtained from MTI Corporation in Richmond, CA. The crystals were grown by the Verneuil process, which consists of shuttling high purity titanyl double oxalate powder (in the presence of oxygen and hydrogen gas) through a combustion tube with a temperature exceeding 2000 °C, with the melted droplets forming a boule.[124] Defects commonly reported in $SrTiO_3$ grown by this method include solid impurities and a high concentration of both dislocations and oxygen vacancies.[124-125]

Sufficiently conductive samples are required to allow Faradaic current at the surface to be measured at the back contact through the whole thickness of the sample. Accordingly,

single crystal samples of 0.7 wt% Nb-doped $SrTiO_3$ oriented in the (100) and (111) directions (±0.5°) were obtained. Figure 2.12 shows the cubic perovskite crystal structure of $SrTiO_3$.[85]

Table 2.1: Properties of TiO_2 (anatase) and $BaTiO_3$

Description	Symbol	TiO_2	$BaTiO_3$	Unit	Source
Relative Permittivity	ε_r	31	1200	1	106,107
Donor Density	N_D	$1{\cdot}10^{18}$	$1{\cdot}10^{18}$	cm^{-3}	108,109
Acceptor Density	N_A	$1{\cdot}10^{16}$	$1{\cdot}10^{16}$	cm^{-3}	
Surface Polarization Magnitude	P	0	0, 26	$\mu C\ cm^{-2}$	110
Electron Mobility	μ_n	0.1	0.5	$cm^2\ V^{-1}\ s^{-1}$	111,109
Hole Mobility	μ_p	$2{\cdot}10^{-3}$	0.25	$cm^2\ V^{-1}\ s^{-1}$	112,113
Electron Affinity	χ	4.2	4.2	eV	114,115
Band Gap	E_g	3.2	3.2	eV	111,116,117
Surface Effective Richardson Constant	$A^*_{n,p}$	$1{\cdot}10^{7}$	-	$A\ m^{-2}\ K^{-2}$	118, 119
Conduction Band Effective Density of States	N_c	$7.9{\cdot}10^{20}$	$5.5{\cdot}10^{19}$	cm^{-3}	120,121
Valence Band Effective Density of States	N_v	$1.8{\cdot}10^{19}$	$1.2{\cdot}10^{20}$	cm^{-3}	120,121
Absorption Coefficient	α	$2{\cdot}10^{3}$	$1{\cdot}10^{5}$	cm^{-1}	122-126
Representative Photon Energy	E_{ph}	3.82	3.82	eV	
Carrier Recombination Lifetime	τ_n,τ_p	$1{\cdot}10^{-9}$	$1{\cdot}10^{-9}$	s	127,128

Sufficiently conductive samples are required to allow Faradaic current at the surface to be measured at the back contact through the whole thickness of the sample. Accordingly, single crystal samples of 0.7 wt% Nb-doped $SrTiO_3$ oriented in the (100) and (111) directions (±0.5°) were obtained. Figure 2.12 shows the cubic perovskite crystal structure

of $SrTiO_3$, with a Ti atom at the center of the unit cell having 6-fold oxygen coordination and the Sr at the corners atoms having 12-fold oxygen coordination.[85]

The Nb dopant atoms substitute a percentage of the Ti atoms in the center of the unit cell. The 0.7 wt% substitution of Ti with Nb translates to a dopant density of approximately $2.3 \cdot 10^{20}$ cm^{-3}. The samples are 0.5 mm thick with areal dimensions of roughly 5 x 5 mm^2, and only one side was polished.

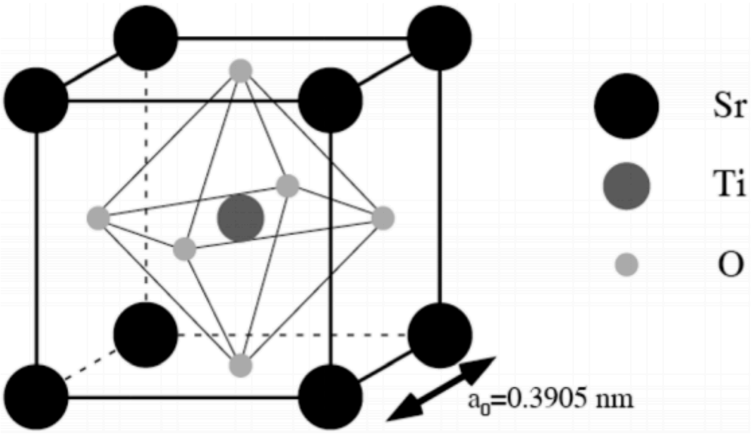

Figure 2.12: Unit Cell for Cubic Perovskite $SrTiO_3$
Figure Reproduced from A. V. Bandura, R. A. Evarestov, and Y. F. Zhukovskii: RSC Adv., 2015, vol. 5, pp. 24115-24125 with permission of The Royal Society of Chemistry.[85]

According to MTI, the samples have a cubic perovskite structure with a lattice parameter of 3.905 Å, a melting point of 2,080 °C, a thermal expansion coefficient of $10.4 \cdot 10^{-6}$ $(°C)^{-1}$, and a resistivity of 0.007 Ω·cm. Table 2.2 displays select properties of $SrTiO_3$ taken from the literature that are particularly relevant to its photocatalytic performance.

Table 2.2: Properties of $SrTiO_3$

Parameter	**Value**	**Reference**
Band Gap (E_g)	3.2 eV	86
Electron Affinity (χ)	4.0 eV	87
Absorption Coefficient (α)	$1 \cdot 10^5$ cm^{-1}	88
Dielectric Constant (ε)	300	89
Dopant Density (N_D)	$2.3 \cdot 10^{20}$ cm^{-3}	*Calculated*
Minority Carrier Lifetime (τ)	$1 \cdot 10^{-9}$ s	90
Point of Zero Zeta Potential (PZZP)	9	51
Electron Mobility (μ_n)	8.5 $cm^2/(V \cdot s)$	MTI,91
Hole Mobility (μ_p)	0.1 $cm^2/(V \cdot s)$	92
Effective D.O.S. Conduction Band (N_C)	$2.1 \cdot 10^{20}$ cm^{-3}	93
Effective D.O.S. Valence Band (N_V)	$1.8 \cdot 10^{20}$ cm^{-3}	93

These parameter values are used in the finite element simulations in Chapter 7 to model the physical device performance. However, data is not always available for each parameter that accurately represents the samples being used in this study: single crystal $SrTiO_3$ doped with 0.7 wt% Nb. Additionally, some of the physical samples have been annealed in various conditions, which could affect the values of some parameters. Therefore, the values given were used as a best approximation. In cases in which it's suspected that the physical values may differ greatly from the approximated values obtained from the literature, the simulations are compared to the physical results to better approximate key parameters.

3 METHODOLOGY

3.1 Physical Photoelectrochemistry

The electrochemical response under illumination, usually measured as current through the sample, can be measured under a potentiostat-controlled bias, which puts the sample (or working electrode) at specific potential difference with respect to a reference electrode of known and ideally constant electrochemical potential. The photocurrent recorded for an n-type semiconductor is expected to resemble the general shape shown in Figure 3.1. By electrochemical convention, negative current (referred to in this work as cathodic) is representative of the electrode (sample) reducing species in solution, while positive current (referred to as anodic) represents the sample oxidizing the solution.

At a large cathodic (negative) potential, the measured Faradaic current of the n-type semiconductor will be high in magnitude (and negative by convention), as an accumulation layer is formed (owing to downward band bending) and electrons are shuttled to the surface. On moving to more anodic potentials, the accumulation layer decreases (the bands begin to flatten), and the cathodic current decreases. This continues until the flat-band condition is reached, where approximately zero current is expected. The flat-band condition is defined as the potential at which there is no band bending at the surface of the semiconductor. Because there is a large concentration of electrons in the n-type

semiconductor, the current under dark or illumination conditions is expected to be the same in the cathodic region (negative of the flat-band potential). Because of the paucity of holes in the n-type semiconductor, the current value in the dark condition at potentials anodic (more positive) of the flat-band potential is essentially zero (a very small positive current may be seen owing to leakage or imperfect dark conditions), even though the bands are bent upward favoring hole transport to the surface. Under illumination, however, as the voltage moves positive of the flat-band potential, an anodic (positive) current develops as photogenerated holes are shuttled to the surface. This current increases with increasing anodic potential until the current is saturated at a value dictated by the irradiance and the overall losses in the system.

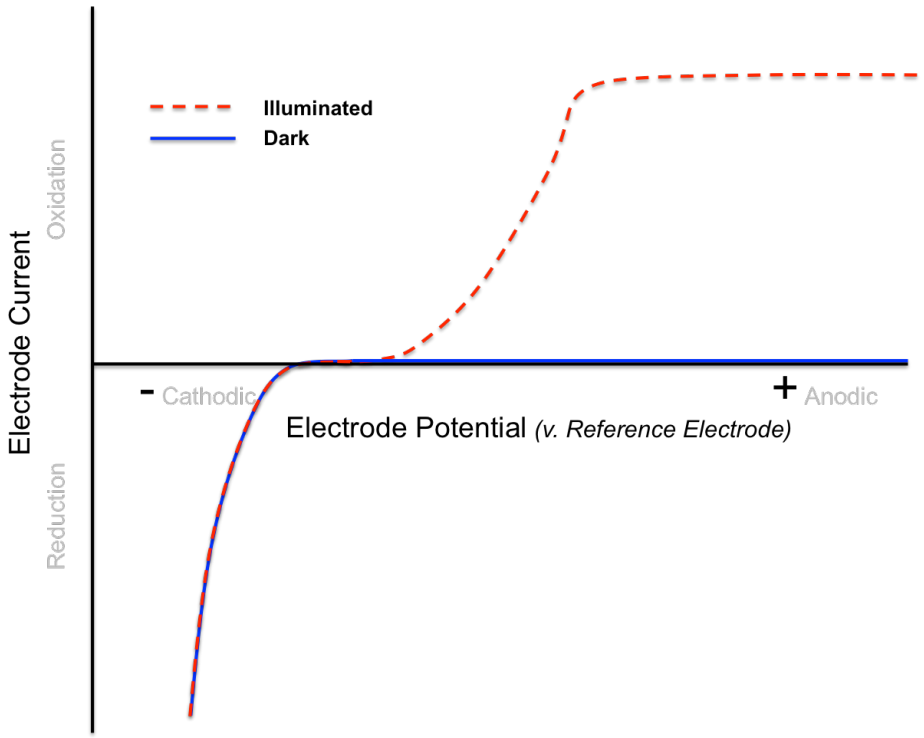

Figure 3.1: Typical Photoelectrochemical I-V Output for n-type Semiconductor

The details of the current-voltage (I-V) characteristic allow for a quantitative characterization of such photoanodic materials. The saturated photocurrent magnitude in the anodic region can be converted to a QE (at a specific voltage and illumination condition). The overall photoconversion efficiency, however, is a function of the applied voltage (see Equation 2.5), decreasing with applied bias. Therefore, a relatively cathodic onset to the photocurrent and a sharp transition to the saturated value ensure a high QE over a wide range of potentials. If these conditions are satisfied, the open-circuit potential under illumination (with no applied bias), which is the potential of the semiconductor after reaching quasi-equilibrium in the solution under illumination, is more likely to have its current close to its maximum value, and the overall energy conversion efficiency will be maximized.

Another important note in analyzing Figure 3.1 is that the current plotted is the net current averaged over the whole surface under test. In reality, both the anodic and cathodic reactions are occurring simultaneously on the surface at any given potential. Especially in the case of surfaces with spatially selective reactivity, which is the focus of this work, there are likely to be some areas on the surface where oxidation is dominant and others where reduction is dominant. This essentially means that the local flat-band potential varies on the surface (as would the local I-V curves), but this local information cannot be extracted from these surface averaged photoelectrochemical measurements. Instead, the contributions of the relative rates of each half reaction and the area fractions favoring each reaction on the total net current must be considered.

This elucidates an important distinction between photoelectrochemical results and those of marker reaction photochemical results, the latter of which are more closely related

to the production of hydrogen from powders. If there were a sample in which half of the surface favored reduction and the other half oxidation, and the rates of each reaction were comparable, then the net photoelectrochemical current should be zero; however, the overall reaction would actually be proceeding on the surface and reaction products would be observed in photochemical marker reactions. This is a drawback to photoelectrochemistry. The benefit of photoelectrochemistry is that the efficacy of one half reaction can be quantified on a surface without the necessity that the other half reaction also occur on the same surface. In the more extreme case, where the majority of the surface favors one reaction occurring at a faster rate, photoelectrochemical testing will reveal the true maximum performance of each half reaction, because the other half reaction occurs at the active counter electrode. For the same sample measured with photochemical marker reactions, the less favorable half reaction will limit the whole process and lead to comparably much lower performance for the desired reaction than in the photoelectrochemical case. Thus, the combination of the two processes is important in establishing the optimal photocatalyst.

3.2 Computational Photoelectrochemistry

This section is an extended version of the theoretical methods detailed in the published work: J. J Glickstein, P. A. Salvador, and G. S. Rohrer: Computational Model of Domain-Specific Reactivity on Coated Ferroelectric Photocatalysts, J. Phys. Chem. C, 2016, vol. 120, pp. 12673-12684.[129]

While physical photoelectrochemical testing, described in Section 3.1, provides valuable information about the net reaction rate at the surface and its voltage dependence, there is a great deal of information left to interpretation especially when studying surfaces exhibiting spatially selective reactivity. Carefully designed simulations have the potential to resolve

cathodic and anodic currents contributing to the total observed photocurrent, identify key parameters affecting performance, and optimize the photocatalyst design.

Simulations in this work have been designed in COMSOL Multiphysics®,[130] which is a finite element software suite developed by COMSOL, Inc. in Burlington, MA. This software was selected because of its advanced solvers for handling the systems of differential equations that describe the relevant semiconductor physics and because of the relative ease of designing, computing, and viewing data for complex geometries which is beneficial for examining surfaces with spatially selective reactivity. Additionally, while the present work focuses on primarily semiconductor physics, COMSOL® has built-in modules that allow for integration of additional relevant physics for more precise catalyst design including detailed illumination and absorption phenomena and reaction kinetics at the surface.

The focus of the simulations developed here is on charge transfer processes within the semiconductor. Given a prescribed illumination irradiance and a prescribed rate of 'reaction' at the surface, the simulations calculate the number and location of carriers generated, what percentage of them reach the surface for reaction, and the mechanism and location of losses in the system. This allows for the pursuit of computational photoelectrochemical experiments with different values of key parameters to compare to the physical photoelectrochemical data. Additionally, it provides further insight into the results by breaking down the current contributions from electrons and holes, the contributions from different areas on the surface, and the origins of losses whether it is from recombination, slow reaction rates, or related factors.

The semiconductor physics incorporated into the model are similar to those recently reported by Garcia-Esparza and Takanabe[131] Using the built-in semiconductor module, a fully coupled damped Newton's method[130] was employed to simultaneously solve Poisson's equation (see Table 3.1 for variable definitions):

$$\nabla \cdot E = -\nabla^2 \phi = \frac{q}{\varepsilon_0 \varepsilon_r} (p - n + N_D - N_A + P) \quad \textbf{(3.1),}$$

the electron and hole current continuity equations:

$$\frac{\partial n}{\partial t} = \frac{1}{q} \nabla \cdot J_n + G_n - U_n \quad \textbf{(3.2)}$$

&

$$\frac{\partial p}{\partial t} = -\frac{1}{q} \nabla \cdot J_p + G_p - U_p \quad \textbf{(3.3),}$$

and the electron and hole drift and diffusion equations:

$$J_n = q\left(\mu_n n E + \mu_n k T \nabla n\right) \quad \textbf{(3.4)}$$

&

$$J_p = q\left(\mu_p n E + \mu_p k T \nabla p\right) \quad \textbf{(3.5).}$$

The key parameters and variables used in the model are summarized in Table 3.1. Equations 3.1-3.5 were used to calculate the electrostatic potential (ϕ) and carrier (electron and hole) concentrations (n and p) throughout the heterostructure. Dopant concentrations, recombination losses, photogeneration rates, and various materials parameters were all factored into the computations. Whenever values were selected, they

were taken from the literature with an aim to describe previously reported marker reaction results (the values are summarized in Section 2.8).

Table 3.1: Model Variables And Constants

Description	**Symbol**
Schottky Barrier Height	ϕ_B
Depth	x
Electric Field	E
Electrostatic Potential	ϕ
Carrier Densities	n,p
Carrier Current Densities	J_n,J_p
Carrier Generation Rate	$G_{n,p}$
Carrier Recombination Rate	$U_{n,p}$
Conduction Band Energy	E_c
Valence Band Energy	E_v
Elementary Charge	q
Vacuum Permittivity	ε_0
Temperature	T
Boltzmann Constant	k
Incident Irradiance	I_0
Metal Work Function	ϕ_m

The arrival of charge carriers to the film surface (where reaction can occur) is dependent on the electrostatic potential (band bending) and relative photogeneration and recombination rates. The conduction (E_C) and valence (E_V) band energies were defined (relative to the reference level) throughout the heterostructure by determining the spatially varying electrostatic potential (ϕ), and combining it with the fixed electron affinity (χ) and band gap (E_g) of the material, as follows:

$$E_c = -q(\Phi + X) \quad \textbf{(3.6)}$$

&

$$E_v = -q\left(\Phi + X + E_g\right) \quad \textbf{(3.7).}$$

Illumination was modeled as being incident at the film surface and penetrating through the film, and into the substrate. The photogeneration rate ($G_{n,p}$), which was applied equally to electrons and holes, was derived from the Beer-Lambert Law:

$$G_{n,p} = \frac{I_0 \alpha}{E_{ph}} \cdot e^{-\alpha x} \quad \textbf{(3.8).}$$

Considering the spectrum of the illumination source of irradiance I_0 under consideration, a representative photon energy (E_{ph}) was selected to approximate the total irradiance as originating from a monochromatic source.

Photogenerated carriers drift and diffuse throughout the heterostructure until either being collected at the film surface or recombining internally. The method of recombination used in the model was trap-assisted Shockley-Read-Hall (SRH) recombination. The SRH recombination rate ($U_{n,p}$), defined as:

$$U_{n,p} = \frac{np - N_c N_v e^{-E_g/kT}}{\tau_p\left(n + \sqrt{N_c N_v} e^{-E_g/2kT}\right) + \tau_n\left(p + \sqrt{N_c N_v} e^{-E_g/2kT}\right)} \quad \textbf{(3.9),}$$

depends strongly on the local carrier concentration (n and p) and lifetimes ($\tau_{n,p}$).

The surface of the thin film coating in contact with solution was modeled as a Schottky contact, with thermionic emission governing the electron and hole currents at the surface:

$$J_n = -\frac{A^*_n T^2}{N_c}\left(n - N_c e^{-\Phi_B/kT}\right) \quad \textbf{(3.10)}$$

&

$$J_p = \frac{A^*_p T^2}{N_v}\left(p - N_v e^{-(E_g-\Phi_B)/kT}\right) \quad \textbf{(3.11).}$$

The work function of the metal (ϕ_m) in the Schottky contact is defined as the approximate electrochemical potential of the solution being modeled. The Schottky barrier height (ϕ_B) was determined self-consistently in the model, and is a function of the electrochemical potential of electrons in the metal ('solution') and semiconductor, the polarization at the film/substrate interface, and the (applied) potential at the back Ohmic contact.

Ultimately, currents through the Schottky contact are of the most interest, as this represents the injection of carriers into the reactive solution (modeled as a metal Schottky contact). The currents reported herein, accordingly, were measured at the surface of the semiconducting film. The value of the leading coefficient in Equations 3.10 and 3.11, known as the effective Richardson constant, A*, can greatly affect the measured surface currents. The constant is commonly calculated as follows:[132]

$$A^* = \lambda \cdot \frac{4\pi q m_e k^2}{h^3} \quad \textbf{(3.12),}$$

wherein the leading coefficient, λ, is a material-specific parameter (dependent on the charge carrier effective mass) that is typically determined empirically. The transport of

carriers across the film/substrate interface was similarly modeled with thermionic emission with the potential barriers defined by the interfacial band bending after equilibration of the film and substrate Fermi levels.

In the application of this model to photocatalysis at a solution interface, A* acts as a kinetic parameter influencing the rate at which arriving carriers react with species in solution (producing Faradaic current in the model). Therefore, it can be treated as a variable parameter used as a general measure of reaction kinetics and was adjusted to explore different operating regimes and to model surfaces of different relative reactivity (given the same number of available carriers). For instance, a sufficiently high A* value models the regime where the rate of delivery of charge carriers to the surface limits the reaction rates, whereas a sufficiently low A* value models the regime where slow reaction rates limit the surface current.[133]

Through the introduction of the fundamental governing semiconductor equations, additional photogeneration and recombination mechanisms, and a reactivity parameter to monitor the reaction rate of charge carriers at the surface, the major elements are in place to gain insight into the operation of select photocatalytic surfaces. Through educated adjustments to these parameters, comparison to experimental results, and a transition to higher-dimensional modeling, this basic framework allows for extensive computational experimentation of the photoelectrochemical behavior of surfaces with spatially selective reactivity.

4 1D COMPUTATIONAL STUDY OF FERROELECTRIC DOMAIN-SPECIFIC REACTIVITY

This chapter is an extended version of the published work:
J. J Glickstein, P. A. Salvador, and G. S. Rohrer: Computational Model of Domain-Specific Reactivity on Coated Ferroelectric Photocatalysts, J. Phys. Chem. C, 2016, vol. 120, pp. 12673-12684.[129]

4.1 Overview

Quantitatively evaluating the efficiency and understanding how to optimize the performance is essential for future photocatalyst design. However, it is often difficult to control independently all of the variables in the laboratory. Reported computational efforts have focused primarily on modeling the solution/photocatalyst interface.[134] However, modeling the transport of carriers throughout the depth of the photocatalyst is essential to understanding the influence of buried charges.

In this chapter, a quantitative computational model is developed of heterostructured ferroelectric photocatalysts, using a general model that represents any potential buried charge separation mechanism. Simulations are then used to assess the impact of specific parameters in the underlying physical model on reactivity and to develop directions to improve catalyst performance. TiO_2 (anatase)/$BaTiO_3$ heterostructures were simulated to make direct comparisons with the thorough photochemical results available in the literature. Simulations of films of varying thicknesses over a range of applied

voltages on domains of different types were carried out and the results expand upon insights gained from the physical experiments in the literature (see Section 2.6).

The general physics behind the model are described in detail in Section 3.2, and the material parameters for TiO_2 and $BaTiO_3$ are summarized in in Table 2.1. A one-dimensional (1D) geometry was used, as shown in Figure 4.1. The geometry was discretized into thousands of mesh elements that are most narrowly defined near the film surface, throughout the thin film, and at the solid interface between the film and substrate. Uniform n-type doping (N_D) was applied throughout the film and substrate, with a relatively smaller concentration of p-type counter dopants also included (N_A). The ferroelectric polarization (P) was modeled in the form of a sheet charge density at the node representing the film/substrate interface and was locally incorporated into Poisson's equation. An Ohmic contact fixed the substrate Fermi level at the back contact node. A Schottky contact at the film surface is fixed to the electrochemical potential of the solution, estimated from the published marker reactions to be -4.76 eV.

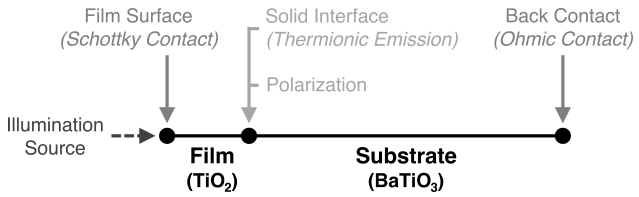

Figure 4.1: Heterostructure Model Geometry and Corresponding Physics

The Richardson constant (A*) can be calculated using Equation 3.12 with λ equated to the charge carrier effective mass (computed from the effective density of states) of TiO_2. The upper limit of A* is the value for the material when in contact with a metal, which can

be calculated using Equation 3.12 to be 10^7 A m^{-2} K^{-2} for TiO_2.[118,119] Replacing the metal with an electrolyte generally decreases A*, as the value becomes directly proportional to the reaction rate constant and the concentration of redox species in solution.[133] The reported height of marker reaction deposits in a set period of time can be used to estimate the current densities required to produce them. This current density magnitude was compared to simulated current density outputs and the A* value adjusted until the simulation output matches the estimated physical currents. The A* value that produces current magnitudes on the order of those estimated form the literature is 10^1 A m^{-2} K^{-2}, significantly lower than the theoretical maximum value of 10^7 A m^{-2} K^{-2}. These two values for A*, corresponding to the theoretical upper limit and the estimation from physical results in the literature, are referred to in the results section as high and low A*, respectively.

The focus of the model is to determine the percentage of photogenerated carriers created throughout the heterostructure that are able to navigate through the spatially varying electrostatic potential and ultimately generate surface current before recombining. The irradiance (I_0) of photons with sufficient energy to be absorbed by TiO_2 and $BaTiO_3$ was estimated from marker reaction setups described in the literature. The ratio of photogenerated carriers to the reacted carriers (the number passing through the Schottky contact or film surface) can be quantified and used to determine the internal quantum efficiency (IQE). The maximum photogenerated current density (representing an IQE of 100%), wherein all photogenerated carriers are transferred to the film surface, is 262 mA cm^{-2} (using the estimated irradiance from reported marker reactions). The setup of the model is directly comparable to that of a photoelectrochemical potentiostat-controlled

testing environment (commonly employed in the literature and described in Section 3.1), wherein Faradaic current is a function of applied voltage. Voltages were applied to the heterostructure by shifting the potential of the Ohmic back contact (V_a) without adjusting the Schottky contact at the film surface.

Unlike in photoelectrochemical testing, there is no back contact in typical marker reaction characterization. Therefore, the results, while providing novel insight into the photoelectrochemical behavior of these heterostructures, must only subjectively be compared to reported marker reaction results. The slower of the two (oxidation and reduction) half reactions limits the overall reaction rate (and the rate of the other half reaction) in a marker reaction setup. Additionally, the voltage is not externally controlled and the reactions occur at the open-circuit voltage under illumination (V_{OC}^*). An estimation of V_{OC}^* (again approximating the photochemical tests reported in the literature) is input into the model as an applied potential to simulate the marker reaction conditions. The V_{OC} without illumination is taken as the metal ('solution') work function of 4.76 eV, which is 0.016 V vs. saturated calomel electrode (SCE). Given the material parameters in Table 2.1, the flat-band potential (E_{fb}) can be computed to be approximately -0.34 V vs. SCE for bulk TiO_2. With increasing illumination, the potential increases from the dark (no illumination) V_{OC} and approaches E_{fb}. Given the very high level of illumination, V_{OC}^* has been approximated as being near but slightly positive of E_{fb} at a value of -0.3 V vs. SCE.

The results presented in this chapter provide a framework for predicting and optimizing the physical performance of these heterostructures. Specifically to these heterostructures, it is shown that by increasing the carrier lifetime to approximately 100 ns, increasing the reduction reaction (majority carrier) kinetics, and optimizing the

potential (externally or through pH), complementary electron and hole reactions of equal magnitude can occur separately on positive and negative domains with an IQE of over 90% (45% if operated in a Z-scheme).

4.2 Results

A series of computational experiments were performed with the goals of revealing the effects of substrate polarizations on current output of the $TiO_2/BaTiO_3$ heterostructure and understanding how various materials parameters influence these results. Table 4.1 summarizes the values of key parameters that were varied to produce the main figures.

Table 4.1: Summary of key variable inputs for film (f) and substrate (s). The voltage, V_a, is applied at the back contact.

Figure #	Film Thickness (nm)	$A^*_n{}^f$ ($A\ m^{-2}\ K^{-2}$)	$A^*_p{}^f$ ($A\ m^{-2}\ K^{-2}$)	P^s ($\mu C\ cm^{-2}$)	V_a (V vs. SCE)	$\tau_{n,p}{}^{f,s}$ (s)
2	20	$1{\cdot}10^7$	$1{\cdot}10^7$	0, ±26	-0.3	$1{\cdot}10^{-9}$
3	variable	$1{\cdot}10^7$	$1{\cdot}10^7$	0, ±26	-0.3	$1{\cdot}10^{-9}$
4	variable	$1{\cdot}10^1$	$1{\cdot}10^1$	0, ±26	-0.3	$1{\cdot}10^{-9}$
5a,b	20	variable	variable	±26	variable	$1{\cdot}10^{-9}$
6a	20	$1{\cdot}10^1$	$1{\cdot}10^1$	±26	variable	variable
6b	variable	$1{\cdot}10^1$	$1{\cdot}10^1$	±26	-0.3	variable
7a	20	$1{\cdot}10^7$	$1{\cdot}10^1$	±26	variable	$1{\cdot}10^{-7}$
7b	variable	$1{\cdot}10^7$	$1{\cdot}10^1$	±26	variable	$1{\cdot}10^{-7}$

For clarity, the Results section has been subdivided as follows. The first section presents a description of the band bending and light absorption in the heterostructure. The second section considers the effect of the film thickness on the current through the heterostructure. The third section describes the potential dependence of the current and identifies the applied potential for the maximum internal quantum efficiency. The fourth

section considers the influence of the carrier lifetime, the magnitude of the polarization, and the Richardson constant. The final section describes the characteristics of a heterostructure optimized for efficiency.

Band Bending and Light Absorption

The effects of neutral (P_0), positive (P_+), and negative (P_-) polarizations at the film/substrate interface on simulated energy level diagrams are shown in Figure 4.2 for a 20 nm film. The voltage at the back contact was set to -0.3 V vs. SCE, the estimated illuminated V_{OC} (V_{OC}^*). For a neutral polarization (no charge at the interface), there is slight upward band bending at the surface of the film that arises from the Schottky barrier. The film cannot completely screen this charge, and the band bending penetrates into the substrate. A positive polarization (P_+ = +26 μC cm^{-2}) at the film/substrate interface lowers the conduction and valence bands at the solid interface, resulting in downward band bending in the substrate and increased upward band bending in the film approaching the surface. As such, holes photogenerated in the substrate are driven away from the solid interface while electrons are driven towards it. Conversely, a negative polarization (P_- = -26 μC cm^{-2}) raises the bands at the solid interface, resulting in significant upward band bending in the substrate and generating a deep space charge layer and strong downward band bending throughout the 20 nm anatase film. The nature of the substrate band bending for negative polarizations favors hole transport in the substrate towards the solid interface and electron transport to the bulk (away from the interface). These simulated results are similar to the qualitative schematics used to interpret the prior observations.[21]

The simulated irradiance is incident on the film surface, on the left edge of Figure 4.2. Due to the low absorption coefficient of anatase, 99.6% of incident photons are

transmitted to the substrate, where the vast majority of photogeneration occurs. It is therefore crucial that carriers photogenerated in this substrate region are separated to avoid recombination. Roughly 75% of the illumination is absorbed within the first 140 nm of the substrate, with a fraction of e^{-1} of the incident illumination transmitted beyond 100 nm into the substrate (representing the absorption depth). For the negative polarization, the potential value dropped by band bending from the solid interface to the bulk substrate value reaches a fraction of e^{-1} at a depth of 89 nm (representing the space charge depth). Roughly 50% of the incident illumination has been absorbed within the space charge depth (though the bands remain bent further into the solid where more absorption occurs). The total simulated thickness of the substrate is 1 μm, to allow sufficient depth for all incident illumination to be absorbed. Only the first 140 nm of the substrate are displayed in Figure 4.2, with the back Ohmic contact being applied at a depth of 1,020 nm into the heterostructure (for a 20 nm film).

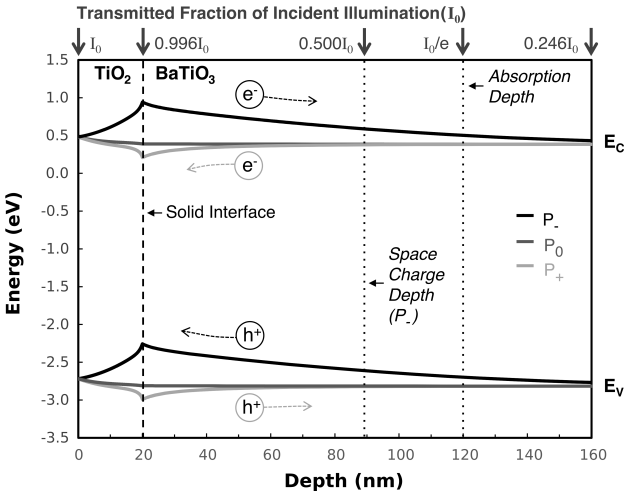

Figure 4.2: Simulated energy level diagrams of heterostructured anatase TiO_2 (20 nm) films on $BaTiO_3$ substrates for neutral, negative, and positive substrate polarizations implemented at the solid interface.

For a neutral polarization, the slight upward band bending favors hole transport to the surface. However, the driving electric field is only minimally present at the absorption depth. On the other hand, the field is much stronger at the absorption depth for negative polarizations, leading to an increased percentage of holes being photogenerated in a region where a field drives them towards the surface. Similarly, electrons are expected to accumulate at the solid interface for positive polarizations more so than for neutral polarizations as a result of the substrate band bending. When holes accumulate at the solid interface for negative polarizations and electrons accumulate for positive polarizations, the band bending in the film provides a barrier (in both cases) to charge transfer to the surface (no tunneling was included in the model). To investigate the net effect of the electric fields introduced by positive and negative polarizations, the surface currents must be examined.

Effect of Film thickness on Current Density

Figure 4.3 shows the electron and hole current densities at the film surface for different polarizations and varying film thicknesses. The open circles represent (positive) hole current densities and the closed circles mark (negative) electron current densities. The value of the kinetic parameter, A*, was set to it's maximum value, which is sufficiently high so as to not meaningfully limit the surface currents. The potential was set to the estimated illuminated open-circuit condition (-0.3 V vs. SCE). The hole currents, or minority carrier currents, are entirely photogenerated and behave as expected from the above discussion. At the 20 nm film thickness used to generate the energy level diagrams shown in Figure 4.2, the negative polarization has the highest hole current density magnitude, at 17.7 mA cm^{-2}. The neutral and positive polarizations have much smaller hole current densities

(respectively 3.59 mA cm^{-2} and 0.421 mA cm^{-2}). The deeper and stronger electric field shuttling holes to the solid interface for negative polarizations results in a significantly higher hole current compared to neutral (and positive) polarizations. This is true despite the unfavorable downward band bending introduced in the 20 nm film.

The behavior of the electron currents is slightly different. The electron current, which is the majority carrier current, is largely not photogenerated but driven by the applied voltage in the simulation. In other words, similar values are observed with or without illumination. The neutral domain has a slightly higher magnitude ($-7.31 \cdot 10^4$ mA cm^{-2}) than the positive domain ($-5.55 \cdot 10^4$ mA cm^{-2}), owing to the upward band bending throughout the 20 nm film (both are much larger than the maximum photogenerated current density of 262 mA cm^{-2}). However, the electron current density for negative polarizations is minimal, being only -5.69 mA cm^{-2}, resulting from the large barrier at the solid interface. Quantitatively, the negative polarization at the film/substrate interface decreases the majority carrier current by three to four orders (which remains true for all film thicknesses). Thus, for a negative domain (at this applied voltage), the minority and majority carrier current densities are of similar magnitudes.

Examining the thickness dependence of the currents in Figure 4.3 reveals that hole current densities are highest for thinner films (results for films below 5 nm are not included because of the diminished applicability of the underlying physics and the probable increased significance of tunneling effects for such thin films). Below film thicknesses of 30 nm, the hole current for negative polarization domains increases as the film thickness decreases. For thicknesses greater than 30 nm, the hole current is independent of thickness and is fixed to a small value. Because nearly all of the photogeneration occurred in the

substrate (for all of these thicknesses), these results indicate that fewer and fewer holes traverse the film barrier without recombining as thickness increases.

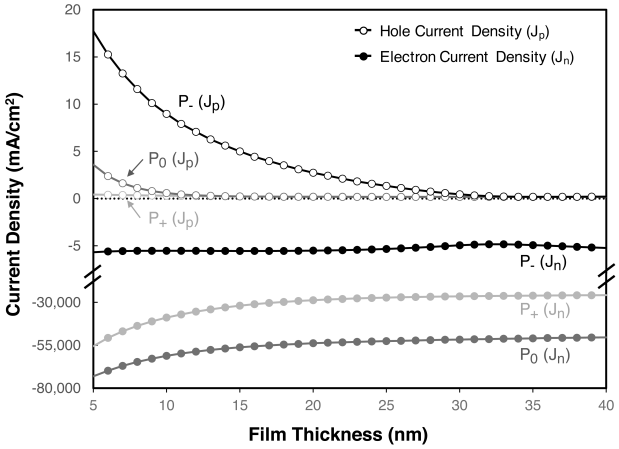

Figure 4.3: Simulated TiO_2(anatase)/$BaTiO_3$ film thickness dependence of surface electron and hole currents (high A* value) for neutral, negative, and positive substrate polarizations.

The high A* value used in Figure 4.3 represents the regime in which reaction rates at the film surface do not significantly limit the current (high A*). As discussed in Section 4.1, an estimated A* value of $1 \cdot 10^1$ A m^{-2} K^{-2} produced current densities similar to the marker reaction rates. The thickness dependence of the electron and hole current densities for different polarizations with the low A* value is displayed in Figure 4.4. Again, the potential was set to -0.3 V vs. SCE. Similar to Figure 4.3, the current contribution of photogenerated holes originating in the substrate disappears beyond roughly 30 nm film thicknesses. In contrast to Figure 4.3, however, the highest value of hole current is observed for the 5 nm film with a neutral polarization. Nevertheless, for films thicker than 5 nm, the hole current is highest for the negative polarization (similar to Figure 4.3). The electron current magnitude is again highest for the neutral polarization and lowest for the negative

polarization. Overall, the current densities in Figure 4.4 (low A*) are much smaller than those in Figure 4.3 (high A*). The hole currents are 1-2 orders of magnitude lower, while the electron currents are 3-4 orders of magnitude lower. In fact, the highest electron current magnitudes in Figure 4.4 are now comparable to those for holes. The electron current is penalized more so than the hole current in the low A* case because of the applied bias (it is slightly anodic of the flat-band condition for a neutral polarization).

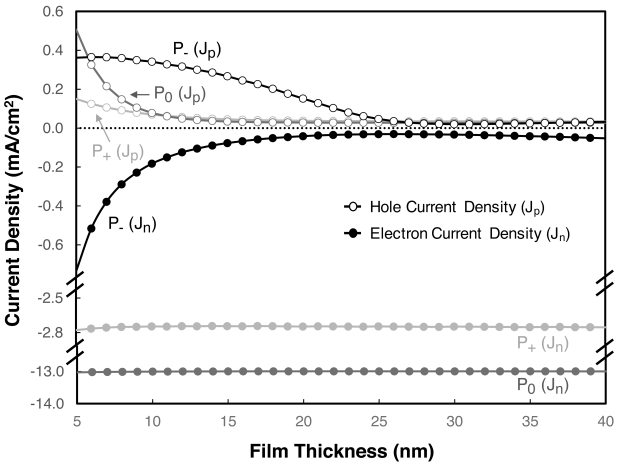

Figure 4.4: Simulated TiO_2(anatase)/$BaTiO_3$ film thickness dependence of electron and hole current densities (low A* value) for neutral, negative, and positive substrate polarizations.

As the film thickness increases beyond the 40 nm displayed in Figures 4.3 and 4.4, the current densities retain approximately the same values as they become reflective of photogeneration in the film. It should be noted that the current densities do not approach the same values regardless of polarization as a consequence of the boundary conditions of the model. The voltage of the modeled Schottky contact is fixed; therefore, when a large polarization is introduced at the solid interface, the degree of band bending at the surface of even the thickest films varies with the sign and magnitude of the buried polarization

charge. These effects are not as noticeable for films less than approximately 40 nm (the displayed domain of Figures 4.3 and 4.4) when the energy bands in the film are bent throughout the entire thickness.

Variation of Current with Applied Potential and Potential for Maximum Efficiency

Several current-voltage curves are depicted in Figure 4.5a for a 20 nm thick film. Only the electron currents (solid symbols) for positive polarizations and hole current (open symbols) for negative polarizations are shown, since these are the most relevant when considering domain specific reactivity. The current-voltage output for both the high A* (lighter symbols) and low A* (darker symbols) cases are included in Figure 4.5. The maximum photogenerated current density for this illumination is marked as a horizontal line (at 262 mA cm^{-2}). The band structure for this film at V_{OC}^{*} (marked with a vertical line in Figure 4.5) was shown in Figure 4.2 (and the current values at this voltage were given in Figures 4.3 and 4.4). From Figure 4.2, it is clear that the J-V behavior of the Schottky contact will be a strong function of the domain orientation, as the band diagrams are significantly different. Specifically, the buried charge for the polar domains perturbs the band bending at the Schottky contact, which should lead to significantly different turn-on voltages (V_{on}) in the J-V curves. As will be demonstrated below, these shifts in V_{on} for the different domains open a window of operation to achieve large efficiencies in ferroelectric photocatalysts.

The minority carrier photogenerated hole currents shown in Figure 4.5a are described as follows. The photogenerated hole currents onset at V_{on}^{+}, increase smoothly with more anodic (positive) voltages, and saturate at a current density near 190 mA cm^{-2}, which represents an IQE of over 70%. At cathodic voltages, more negative than V_{on}^{+} for the negative domains, the hole currents are approximately zero for both A* values. The

difference between the two curves for the different A* values is small, with the higher A* material having higher current values at lower anodic voltages above V_{on}^{+} (i.e. the curve is shifted slightly to the left).

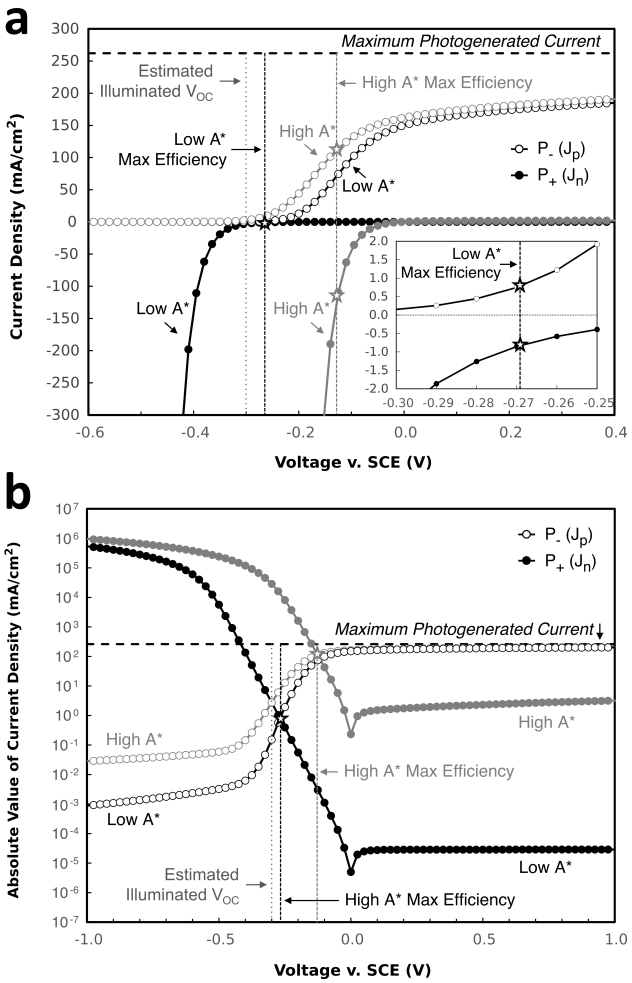

Figure 4.5: Simulated voltage dependence of electron (J_n) and hole (J_p) current densities at the surface of a 20 nm TiO_2 film on $BaTiO_3$, displayed in **(a)** linear and **(b)** semi-log representations. Conducted separately for both high (theoretical maximum) and low (corresponding to reported physical results) A* values. The voltage, assumed to be the open-circuit potential under illumination (V_{OC}^{*}), is noted along with the potentials that maximize the IQE for each A* value (with the low A* region of interest expanded in the inset of (**a**)).

The majority carrier electron currents (which are not generally photogenerated in the model) are described as follows. For large anodic voltages, more positive than the turn-on voltage (V_{on}^{-}) for positive domains, the electron currents are approximately zero. In the high A* case, the electron current rapidly increases in magnitude for voltages more cathodic than V_{on}^{-}. Note that there is no saturation in the majority carrier current, and it quickly becomes larger than the maximum photogenerated current density in the model. On the linear scale for the low A* case, the general shape of the electron current is the same as that for the high A* case, but it appears that the onset potential (V_{on}^{-}) is shifted to a significantly more cathodic voltage compared to the high A* electron current. If J-V behavior is plotted on a semi-log plot as in Figure 4.5b, the low and high A* electron currents onset at virtually the same potential, but the rate of increasing current magnitude is greatly reduced for low A*, and the electron current appears to onset at a more cathodic potential on a linear plot. Note that the downward band bending in the substrate at V_{OC}^{*} (for P_{+} in Figure 4.2) favors emission of electrons from the substrate into the film, while the film band bending presents a barrier to their emission into the solution: i.e., the electron population at the film/substrate interface is high. A large A* value permits a significant fraction of the majority carriers emitted from the substrate to pass through as Faradaic current, while a low A* value prevents most of these carriers from registering as Faradaic current through the film surface (though there is a smaller leakage component). By moving to more cathodic voltages, the band bending in the film ultimately favors emission into the solution and the current rapidly increases, despite the low A* value.

At any given voltage, the performance of the photocatalyst will be limited by the slower of the two reactions (i.e. the domain with the lower of the two current values). If it is

assumed that positive and negative domains producing electron and hole Faradaic currents (respectively) operate at the same potential, then the voltage at which the performance of the heterostructure is maximized will be at the potential for which the equal magnitudes of the electron and hole currents are maximized. These potentials of maximum efficiency for the low and high A* values are labeled in Figure 4.5. The corresponding maximum balanced electron and hole current density magnitudes are found where the dashed lines intersect the current-voltage curves, and can be used to compute the IQE_{max}. In either case, hole currents limit the overall current for voltages left of the dashed maximum efficiency line while electrons limit the current for voltages to the right.

For the 1D simulations presented here, the maximum efficiency represents the balanced performance for electrons in positively polarized domains and holes in negatively polarized domains. However, it is unknown what charge transfer may occur at the boundaries between neighboring, oppositely polarized, domains in a 2D (or 3D) geometry (this is the focus of Chapter 5). If the charge carriers not dominant in the surface reactions recombine at the domain boundaries, then the efficiency limit ($IQE_{Z,max}$) would be half of the IQE_{max}, as the Z-scheme photocatalyst loses half of all photogenerated carriers. However, if the non-dominant carriers drift across the domain boundaries to oppositely polarized domains and are driven to the surface to react, then the IQE_{max} value represents the highest theoretical efficiency. Therefore, the theoretically achievable efficiency predicted by this 1D model is somewhere between IQE_{max} and $0.5 \cdot IQE_{max}$ (= $IQE_{Z,max}$), depending on the extent of charge transfer at domain boundaries.

Influence of the Richardson Constant, Polarization, and Carrier Lifetime on Efficiency

When A* is not significantly limiting (high A*), the IQE_{max} for balancing oxidation and reduction reactions separated to oppositely polarized domains is 43%, which occurs at V_a = -0.13 V (SCE). This voltage that maximizes performance is shifted away from V_{OC}^* = -0.3 V (SCE) by +0.17 V, the equivalent of 2-3 pH units in solution and only 14% of the 1.23 V water-splitting voltage. Considering the fractional voltage input (relative to the water splitting voltage) to represent a fractional energy loss, the voltage efficiency would still be 37% (or 19% for the Z-scheme). By operating at this optimal voltage, the IQE for high A* is increased nearly forty-fold relative to the IQE = 1.1% at V_{OC}^*. The IQE_{max} when A* is at the value estimated from reported marker reaction data (low A*) is only 0.31%, occurring at V_a = -0.27 V (SCE), or +0.03 V from V_{OC}^*. This value is roughly five times higher than that at V_{OC}^* (IQE = 0.063%) for the low A* case. Note that the steep drop in optimal performance from the high to low A* values indicates that slow kinetics to the majority carrier reaction limit the optimal performance of the real photocatalyst to only a fraction of the possible value. Examination of Figure 4.5 reveals that the reduced kinetics for the majority carriers suppresses the current in the voltage region just below V_{on}^- (≈ 0 V in Figure 4.5b), causing the electron current to further limit the reactivity to the cathodic side of V_{on}^-. The low A* electron current is only slightly greater than the hole current at V_{OC}^*. On the other hand, faster majority carrier kinetics at the surface (high A*) results in large electron currents in the voltage region just below the V_{on}^-, which opens up a wide voltage region to the anodic side of V_{on}^+ in which the hole current is limiting the reaction but increasing with increasing positive voltages.

The optimal operating potentials and corresponding current densities (and IQE) are shown in Table 4.2 for various polarization magnitudes to assess the degree to which ferroelectrics enhance photocatalytic performance.

Table 4.2: Summary of conditions that optimize performance* for different multiples of the $BaTiO_3$ substrate polarization magnitude (P_{BTO} = 26 μC cm^{-2}) beneath a 20 nm TiO_2 film.

**Optimal performance is represented by the voltage at which the electron current density for positive polarizations is equal in magnitude to the hole current density for negative polarizations. The maximum efficiencies (without considering any lost efficiency from applied voltage) and the voltage at which they are achieved are displayed for the low A* value, the high A* value, and an increased carrier lifetime (with high A*n and low A*p, see Figure 7).*

Polarization Magnitude:		**0**	**0.25·P_{BTO}**	**0.5·P_{BTO}**	**P_{BTO}**	**2·P_{BTO}**
A^*_n Low, A^*_p Low, τ = 10^{-9} s (shown in Figure 4.5 for P_{BTO})	**V (vs. SCE)**	-0.161	-0.206	-0.230	-0.269	-0.339
	J (mA cm^{-2})	0.0582	0.277	0.479	0.807	1.53
	IQE_{max}	0.022%	0.11%	0.18%	0.31%	0.58%
A^*_n High, A^*_p High, τ = 10^{-9} s (shown in Figure 4.5 for P_{BTO})	**V (vs. SCE)**	0.026	-0.080	-0.096	-0.126	-0.184
	J (mA cm^{-2})	0.478	74.5	96.2	113	131
	IQE_{max}	0.18%	28%	37%	43%	50%
A^*_n High, A^*_p Low, τ = 10^{-7} s (shown in Figure 4.7 for P_{BTO})	**V (vs. SCE)**	-0.071	-0.111	-0.121	-0.147	-0.201
	J (mA cm^{-2})	60.6	236	240	242	245
	IQE_{max}	23%	90%	92%	92%	94%

For neutral domains (zero polarization), the optimal performance is reduced by two orders of magnitude for a high A* and one order of magnitude for low A* from that for domains with the $BaTiO_3$ polarization (P_{BTO}). For domains with only one quarter of P_{BTO}, there is still a significant increase in optimal efficiency compared to zero polarization, and only a relatively small drop from the performance of P_{BTO}. The relatively small differences between the IQE_{max} for -0.25·P_{BTO} (28% for high A*) and 2·P_{BTO} (50% for high A*) is

consistent with findings in the literature that similar reactivity effects are observed for differently oriented grains, for different materials (that have different spontaneous polarization magnitudes), and for different sources of internal fields (or surface charges).[28]

Because the primary mechanism for lost efficiency in the minority carrier current is carrier recombination, the carrier lifetime (τ) value should be addressed relative to performance. In the prior simulations, a τ of 10^{-9} s was used, as this is a value often reported in the literature. Figure 4.6a shows the current-voltage behavior for a 20 nm film using the low A* value (poor surface kinetics) and values of $\tau = 10^{-9}$, 10^{-7}, 10^{-5} s.

For the minority carrier current, increasing the lifetime from 10^{-9} s shifts the apparent onset V_{on}^{+} to significantly more cathodic values, increases the saturation current values significantly to more than 90% of the maximum value, and shifts the voltage at which saturation is achieved to more cathodic values. All of these changes open the window further for improved efficiencies. For the majority carrier current, the changing lifetime does not meaningfully affect the electron current, which exhibits a relatively cathodic onset in the linear plot due to the low A* value (see Figure 4.5b). As a result, the kinetically limited electron currents in Figure 4.6a limit the achievable efficiencies for almost all carrier lifetimes. For such photocatalysts, performance improvement will be achievable by modifying surface kinetics (A*), as described previously.

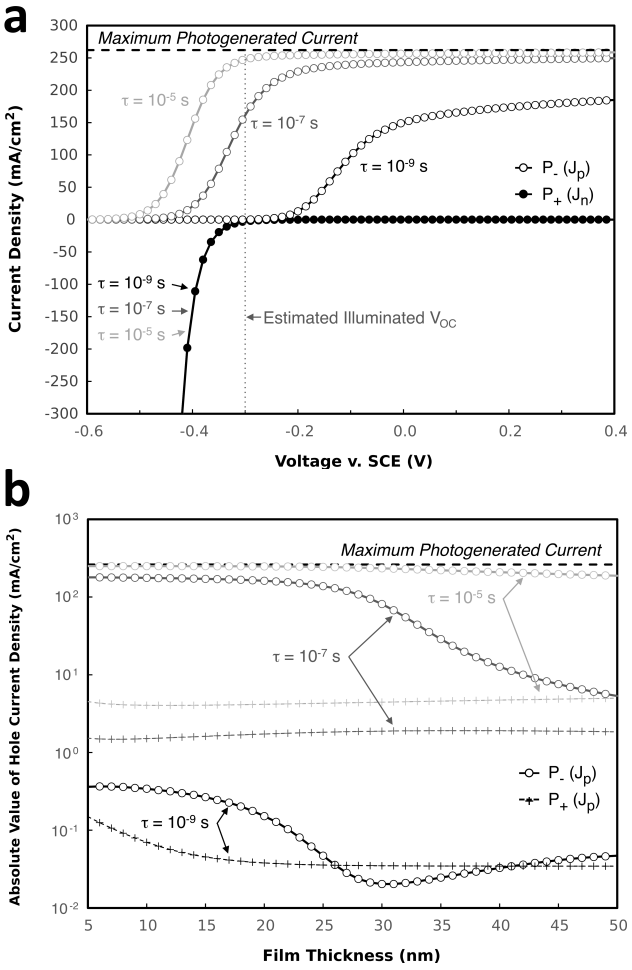

Figure 4.6: (a) Simulated voltage dependence of electron (J_n) and hole (J_p) current densities (low A* value) at the surface of a 20 nm TiO_2(anatase) film on $BaTiO_3$ for various values of the carrier recombination lifetime (τ). **(b)** Simulated TiO_2(anatase)/$BaTiO_3$ film thickness dependence of hole current densities (low A* value) produced by negative and positive substrate polarizations for various values of the carrier recombination lifetime (τ).

The thickness dependencies of the hole current density for negative ($P_-(J_p)$) and positive ($P_+(J_p)$) polarizations are shown in Figure 4.6b for three carrier lifetimes. Increasing the lifetime increases both the negative and positive polarization hole currents. However, the negative polarization domains still exhibit significantly higher hole currents relative to the positive polarization domains. Increasing the hole carrier lifetime also extends the film

thickness range over which the minority carriers photogenerated in the substrate contribute significantly to the surface current.

Optimized Heterostructures

Figure 4.5 indicates that the maximum efficiency is limited in the high A* case because the hole current onset is too anodic. Figure 4.6a indicates that the maximum efficiency is limited in the greater carrier lifetime case because the electron current onset is too cathodic. Combined, these figures indicate that a near-optimal device can be obtained in a ferroelectric (which minimizes the internal recombination in the substrate) with a high lifetime for the minority carriers and fast surface kinetics for the majority carriers. This is born out by simulations, as shown in Figure 4.7a, which displays the simulated current-voltage output using a lifetime on the order of 10^{-7} s and a high A^*_n value for electrons (but a low A^*_p value for holes) for a 20 nm film. The IQE at the estimated illuminated V_{OC} is 65% and the maximum efficiency jumps to 92% (at V_a = -0.146 V (SCE)). Considering the small shift from open circuit (0.154 V), the voltage efficiency is still 81% for this heterostructure.

The inset of Figure 4.7a reveals that increasing the lifetime fundamentally shifts the minority carrier current onset to more cathodic potentials. Increasing the lifetime further (to 10^{-5} s), increasing A^*_p, or decreasing the film thickness would all result in reducing the losses even further. The efficiency can be increased slightly by increasing the substrate polarization magnitude (see Table 4.2), but the IQE_{max} is still 90% even when only one quarter of the $BaTiO_3$ polarization is applied.

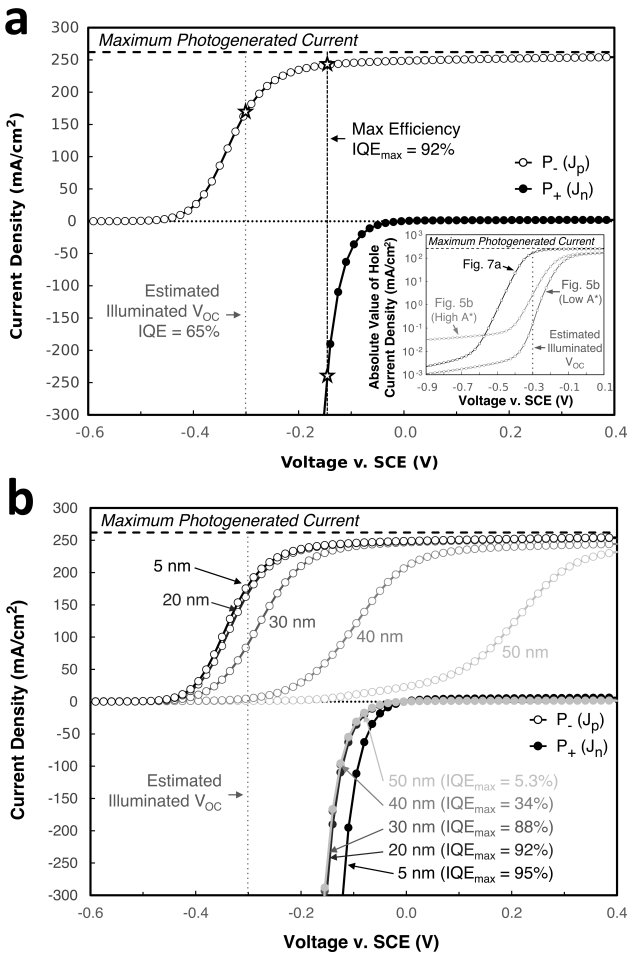

Figure 4.7: Simulated voltage dependence of electron (J_n) and hole (J_p) current densities ($A^*_n = 1{\cdot}10^7$ A m^{-2} K^{-2}, $A^*_p = 1{\cdot}10^1$ A m^{-2} K^{-2}) for $\tau = 10^{-7}$ s for $BaTiO_3$ coated with **(a)** 20 nm TiO_2(anatase) film and **(b)** various TiO_2(anatase) film thicknesses (the arrows labeling the electron currents indicate the voltage at which the IQE is maximized). The inset in **(a)** shows the semi-log J-V characteristic of the minority carrier current for a 20 nm film compared to those from Figure 4.5.

The thickness dependence of the current-voltage curve and the corresponding maximum efficiencies are displayed in Figure 4.7b. The arrows labeling the electron current density curves mark the voltage at which the electron and hole currents become equal (and IQE_{max} is achieved). There is only a small increase in performance when the film thickness is decreased to 5 nm (IQE_{max} = 95%), with the increase primarily resulting from a small

anodic shift in the majority carrier current. The minimal thickness dependence of the hole current between 5 nm and 20 nm is evident from Figure 4.6b for the 10^{-7} s lifetime. Beyond a 30 nm film thickness in Figure 4.7b, the achievable IQE quickly drops off before reaching only 5.3% for a 50 nm film. Even for the 50 nm film, the hole current density eventually saturates near the maximum theoretical value, but does so at a voltage well anodic of the electron current onset.

4.3 Discussion

The predominant result from the marker reactions in the literature was that for TiO_2(anatase)/$BaTiO_3$ heterostructures (and other similar materials), reduction reactions were more active on coated positive domains and oxidation reactions were more active on negative domains. It is evident from Figure 4.2 that negative and positive polarizations generate band bending in the substrate that favors increased hole and electron transport to the solid interface, respectively, compared to a neutral polarization. However, it is also evident that the band bending in the film impedes the transfer of these carriers that accumulate at the interface from reaching the surface and contributing to the current. The net effects of the favorable band bending in the substrate and the unfavorable band bending created in the film are evident in the currents in Figure 4.3 as a function of thickness. Below a thickness of approximately 30 nm, the band bending effects in the film are overwhelmed by those in the substrate, similar to that observed in the literature. [21]

The simulations demonstrate that negative polarizations produce the highest magnitude hole current density and the lowest magnitude electron current density, which support the qualitative explanation for domain specific reactivity.[21] It also suggests that

physical observations can be explained using only the basic assumptions about carrier excitation and transport incorporated into the computational model. In other words, tunneling through energy barriers or polarization-dependent surface potentials need not be implemented to produce the physical observations. This outcome does not change when the kinetics are more limiting, as in Figure 4.4. The simulations also imply that the net effect of a polarized substrate with multiple domains may increase the efficiency of the overall reaction (compared to an unpolarized substrate).

Another important insight from Figures 4.3 and 4.4 is that, for a minimally absorbing anatase film, thinner films result in increased hole current with hole transfer from the substrate being largely absent for films thicker than 30 nm. Published marker reaction results revealed that domain specific reactivity was clearly visible in AFM for a 10 nm film, less so for a 30 nm film, and not clearly discernible for a 50 nm film.[21] This finding is generally consistent with the computational result that the current contribution of holes photogenerated in the substrate is minimal beyond 30 nm. Therefore, in designing a TiO_2(anatase)/$BaTiO_3$ photocatalyst, the film should be as thin as possible that can also maintain chemical stability.

A primary goal of building a computational model of coated ferroelectric photocatalytic materials was to quantitatively estimate the performance and understand how the performance could be optimized. Figure 4.5 reveals that controlling the potential is crucial to achieving the optimal overall reaction rate. It is evident from Table 4.2 that, when the optimal potential is used, the performance is at least one order of magnitude higher for a polarized substrate than for an unpolarized one. To calibrate the model so that it mimicked the physical situation, values of the reactivity parameter (A*) were assumed to

reproduce reported results. Using this relatively low A* value, the IQE at V_{OC}^* is only 0.063%, which increases to an IQE_{max} of 0.31% when the potential is adjusted.

To achieve the much more desirable IQE_{max} of 43% for the high A* value, the kinetics must be fast enough to approach the behavior of a Schottky metal contact to TiO_2. In particular, it is the effect of A^*_n on the majority carrier current onset that enables such a high increase in IQE_{max}, because the majority carrier onset voltage on positive domains becomes increasingly anodic with increased surface kinetics (A*). However, it is clear that A* is a surface parameter, and therefore has a much more significant effect on the majority carrier than it does on the minority carrier (which is not necessarily present in high concentrations near the surface). To increase the efficiency beyond 43%, the minority carrier recombination lifetime should be increased. In the simulations, this was achieved by increasing τ by two orders of magnitude from the 1 ns obtained from the literature.[127] There is a wide range of carrier lifetimes reported in the literature for TiO_2 and $BaTiO_3$ depending on the growth conditions and processing. A lifetime increased by two orders of magnitude by reducing the density of recombination sites results in a sharper and more cathodic hole current onset, as shown in Figure 4.6a. When combined with faster electron kinetics in Figure 4.7, the IQE_{max} is increased to 92% for a 20 nm film and 95% for a 5 nm film. These numbers were found at voltages slightly shifted from the open-circuit condition, but even accounting for the lost energy owing to the applied voltage (and for the Z-scheme nature of the two domain reactions), the efficiencies are still in the range of 80% (or 40% for Z-scheme).

This same modeling approach is extended to a 2D geometry in Chapter 5 to incorporate the influence of charge transfer between neighboring domains. It can also

ultimately be applied to optimizing the performance of visible light absorbing substrates with internal fields with the goal of developing a photocatalyst with an economically competitive solar to hydrogen efficiency.

4.4 Conclusions

A 1D computational model designed in COMSOL® was used to predict the photocatalytic performance (IQE) of TiO_2 films on ferroelectric $BaTiO_3$ and criteria were identified that enable increased efficiencies. Assumptions of classical semiconductor device behavior and a Schottky contact at the surface were sufficient to produce domain specific electron and hole current densities that generally support reported physical results. The predicted domain specificity was not significantly altered when the polarization magnitude was varied. The estimated internal quantum efficiencies of the heterostructures (previously characterized only qualitatively) are below 1%. By increasing the carrier lifetime, increasing the reduction reaction kinetics, and optimizing the potential all within physically reasonable ranges, complementary electron and hole reactions of equal magnitude can occur separately on positive and negative domains with an IQE of over 90% (45% if operated in a Z-scheme).

5 2D COMPUTATIONAL STUDY OF FERROELECTRIC DOMAIN-SPECIFIC REACTIVITY

This chapter is an extended version of the submitted manuscript:
J. J Glickstein, P. A. Salvador, and G. S. Rohrer: Multidomain Simulations of Coated Ferroelectrics exhibiting Spatially Selective Photocatalytic Activity with High Internal Quantum Efficiencies, J. Mater. Chem. A, submitted.

5.1 Overview

In Chapter 4, a one-dimensional (1D) computational model was used to improve understanding and to quantify the performance of individual domains in coated ferroelectric semiconductors.[129] The internal quantum efficiency (IQE) of $TiO_2/BaTiO_3$ heterostructures from physical marker reaction literature results was estimated to be below 1%.[129] Simulations showed that the IQE could be increased to over 90% by increasing the reduction reaction kinetics, increasing the carrier lifetime, and optimizing the potential used in the model (all within physically attainable values).[129] However, the greater than 90% IQE was based on separate evaluations of the reduction reactions on individual positively polarized domains and oxidation reactions on individual negatively polarized domains (in both cases the alternate carrier was collected at the back contact, similar to a photoelectrochemical cell electrode). The question related to photocatalytic powder reactors is: how do charge carriers photogenerated in adjacent domains with different polarizations behave? Two limiting possibilities are that the photogenerated

charge carriers driven away from the surface either (1) reach the surface of the adjacent domain to react or (2) recombine with one another to be lost, similar to a Z-scheme photocatalyst. The maximum IQE for the first case would be similar to the 1D case, ≈ 90 %, while maximum IQE of the Z-scheme photocatalyst would be ½ of the 1D case, ≈ 45%.

In this chapter, a two-dimensional (2D) model is used to simulate multidomain coated ferroelectric photocatalysts. Material parameters from Table 2.1 are used, with a few refinements that were shown in Chapter 4 to enable efficiencies exceeding 90% in the 1D model.[129] The maximum theoretical Richardson constant is used for electrons (10^7 A m^{-2} K^{-2}) while the physically estimated value is used for holes (10^1 A m^{-2} K^{-2}). Additionally, the carrier lifetime is set to 100 ns. Variations in surface majority and minority carrier current densities were determined across different domains at the illuminated open-circuit potential. These results are particularly relevant in the case of a colloidal catalyst, where the reactions occur in open-circuit conditions at a potential controlled by the solution. The influence of the electric potential on minority carrier currents between oppositely polarized domains is examined. Additionally, the dependence of the surface minority carrier current on domain width is determined. By controlling key parameters, including domain width and the potential, an optimal IQE for balancing oxidation and reduction reactions across the surface as high as 90% is demonstrated, far exceeding a pure Z-scheme mechanism and approximately equaling the 1D optimal predicted performance.

5.2 Results

The 2D model geometry used in this study is depicted in Figure 5.1. The lateral position is defined as the position parallel to the film surface, while the depth is defined as

the position perpendicular to the surface. The film was modeled as a donor-doped anatase TiO_2 film being 10 nm thick. The donor doped ferroelectric $BaTiO_3$ substrate was modeled as being 1,000 nm (1 μm) thick, to provide sufficient space for all light to be absorbed. The spatially varying polarization was applied along the substrate-film interface, switching between positive and negative values of the spontaneous polarization magnitude of $BaTiO_3$. For simplicity, the width of positive and negative domains were always equal and the spontaneous polarization was aligned to be normal to the surface. These 180° domain boundaries are marked as dashed lines at the interface in Figure 5.1. Light (of sufficiently energetic photons) was modeled as being uniformly incident at the film surface with an irradiance of I_0 and as being absorbed according to the Beer-Lambert law, resulting in a transmitted irradiance of $0.998I_0$ (0.2% absorbed) at the film-substrate interface and $0.050I_0$ (95% absorbed) at a depth (below the film surface) of 310 nm.

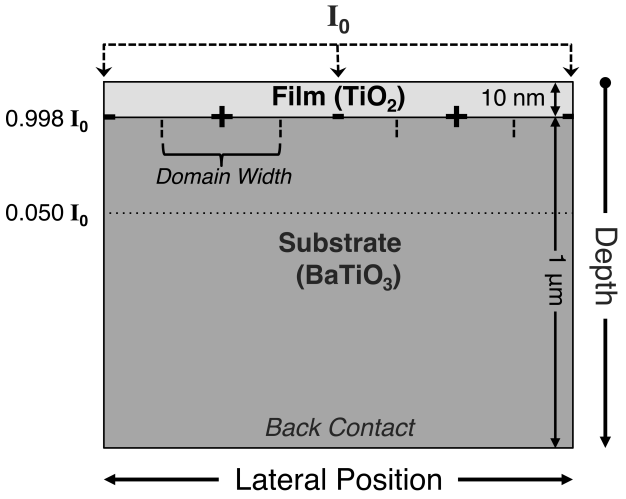

Figure 5.1: Heterostructure 2D Model Geometry

The effective Richardson constants were set to $1 \cdot 10^1$ A m^{-2} K^{-2} for holes and $1 \cdot 10^7$ A m^{-2} K^{-2} for electrons. In this way, the kinetics of the oxidation reaction are set to those values predicted from published marker reaction data and the reduction reaction kinetics are set to the maximum theoretical value (this can be achieved physically by the addition of a co-catalyst). The most important metrics for evaluating the simulated multidomain photocatalytic performance are the spatially varying electron and hole current densities, as well as their surface averages. The variation in surface currents with lateral position reveals the location and rate at which oxidation and reduction reactions are expected to occur and the extent of domain-specific reactivity can be readily observed. The surface average current densities, computed by integrating the current density for a single carrier across the film surface, can be used to determine the overall efficiency of a given half reaction over the total illuminated area. The lower of the reductive and oxidative surface average currents represents the limiting half reaction, and can be used to determine the overall IQE of the water-splitting reaction.

The previously reported marker reaction data from thin TiO_2 films on $BaTiO_3$ are reproduced in Figures 5.2a & 5.2b for oxidation and reduction reactions, respectively.[21] These figures display domain-specific reactivity on the surface of a 15 nm film. The illuminated heterostructure was submersed in an aqueous lead acetate solution in Figure 5.2a, with the areas of bright contrast representing solid PbO_2 oxidation reaction products. The same illuminated surface was submersed in aqueous silver nitrate solution in Figure 5.2b, with bright contrast now representing solid Ag reduction reaction products. The reaction products for each half reaction appear to be segregated to specific, complementary, ferroelectric domains. While quantitative reaction rates are difficult to

determine from these experiments, because the surface becomes coated during testing, the submersed sample had to be illuminated for 18 times as long to produce a comparable height of oxidation products (Figure 5.2a) as reduction products (Figure 5.2b), indicating the oxidation reaction is slower. The average domain width from these physical materials was estimated to be ≈ 250 nm. The domain boundary angles in the physical samples vary, with a high concentration of 90° boundaries visible in Figures 5.2a & 5.2b. The simulations herein were carried out using 180° domains, which model the maximum difference in the normal component of the polarization for neighboring domains.

The simulated surface oxidation (hole) and reduction (electron) current densities, evaluated at V_{OC}^{*} for 250 nm domains and a 10 nm film, are shown in Figures 5.2c & 5.2d, respectively. The full simulated surface geometry was 1,000 nm, but only 500 nm of the surface are shown for simplicity: half of a positively polarized domain, a full negatively polarized domain, and another half of a positive domain (the domain boundaries are given as vertical dashed lines). The surface average current densities ($J_{p,n}^{avg}$) are obtained by integrating across the displayed 500 nm of the surface. In Figure 5.2c, the maximum photogenerated current density (J_{ph}^{max}) and twice the maximum photogenerated current density ($2J_{ph}^{max}$) are also shown as horizontal dotted lines. The maximum photogenerated current, fixed by the irradiance to be 262 mA cm^{-2}, is the maximum possible value of the surface average hole current density. It can be exceeded by the local hole current density, however, if lateral driving forces are present that allow holes to accumulate in certain regions on the surface. The $2J_{ph}^{max}$ current represents the value if all photogenerated holes uniformly reacted on the surface of the negative domain (½ of the surface).

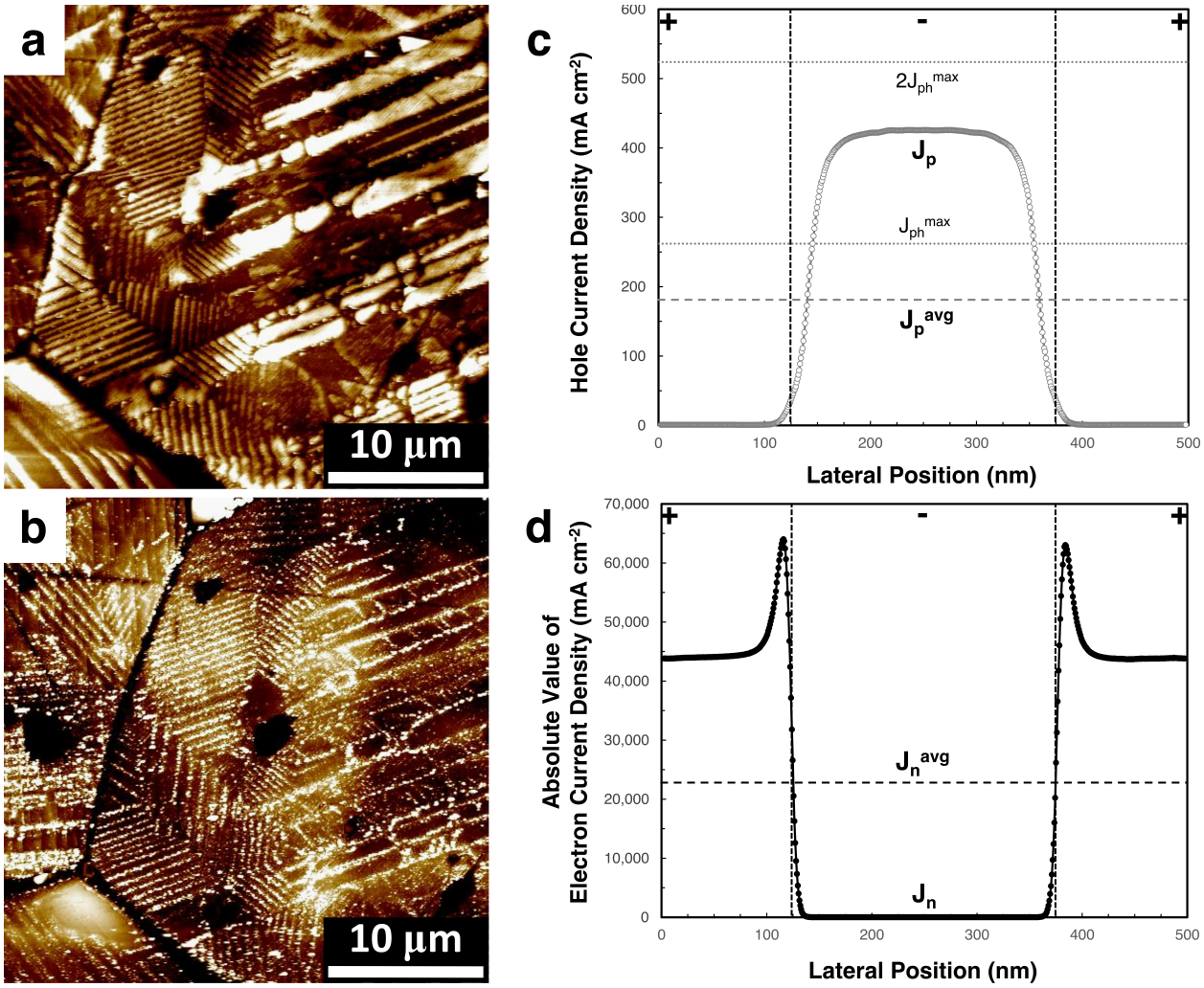

Figure 5.2: Comparison of experimental marker reaction data (a,b)* and simulated Faradaic current variation across the surface (c,d) for oxidation (a,c) and reduction (b,d) reactions. Marker reaction results are for an illuminated 15 nm TiO_2 film on $BaTiO_3$ exposed to aqueous lead acetate solution (a) and aqueous silver nitrate solution (b), while simulated photoelectrochemical results are for an illuminated 10 nm TiO_2 film on $BaTiO_3$ fixed at V_{OC}^* with alternating 250 nm wide negative and positive domains.

*Figures a & b reproduced from [21]

Examining Figure 5.2c, the hole current density is nearly zero (< 1 mA cm^{-2}) at the surface of positive domains, increases near the domain boundary, and peaks above 420 mA cm^{-2} at the center of the negative domain. The domain-specific simulated hole current in Figure 5.2c is qualitatively comparable to the observed physical reactivity of Pb^{2+} oxidation

in Figure 5.2a. The current density throughout the majority of the negative domain exceeds J_{ph}^{max}, but never exceeds $2J_{ph}^{max}$. The ratio of J_p^{avg} to J_{ph}^{max} can be used to calculate an IQE for the minority carrier reaction, being 69% for this simulation, confirming a performance that exceeds a pure Z-scheme (which could never be higher than 50%).

This result is very promising, assuming that the positive domains can also promote the complementary reduction reaction. Figure 5.2d displays the spatial variation of the electron current density (J_n) and its surface average (J_n^{avg}). Reductive electron currents are negative by convention, so the absolute value is plotted here for direct comparison with the hole currents. The domain specific simulated electron surface current shown in Figure 5.2d is qualitatively comparable to the observed physical reactivity of Ag^+ reduction in Figure 5.2b, and is complementary to the hole currents shown in Figure 5.2c. The magnitude of the current density is very low across the majority of the negative domain (< 10 mA cm^{-2}), increases sharply near the boundary to a peak value above 63,000 mA cm^{-2} on the edge of the positive domain, and settles to a value close to 44,000 mA cm^{-2} near the center of the positive domain. These values for J_n on positive domains greatly exceed J_{ph}^{max}, and are the result of the relatively cathodic bias and substantial donor density in the catalyst heterostructure. The significantly higher order of magnitude for electron current densities at the illuminated open-circuit potential (V_{OC}^*) compared to hole current densities parallels the much faster rate of production of marker reaction products for reduction compared to oxidation.[21] Additionally, the accumulation of the electron current near the boundaries of positive domains is comparable to physical marker reaction observations for 180° domain boundaries that show deposits concentrated near the boundaries.[22] Finally, in comparing the quantitative results from Figures 5.2c & 5.2d, it is clear that the net reaction on negative

domains is oxidation and the net reaction on positive domains is reduction, with oxidation on the negative domains limiting the overall reaction across the entire surface.

The results from Figure 5.2c strongly suggest the existence of lateral driving forces that promote the transfer of minority carriers from positive to negative domains. Figure 5.3a plots the hole concentrations and electric fields in a 250 nm wide and 100 nm deep region of the model, containing a domain boundary in the middle separating halves of negative and positive domains. The grayscale gradient denotes the log of the local hole concentration (which drives diffusion currents) and the arrows indicate the local direction of the electric field (acting on a positive charge, which drives drift currents). The arrow length is logarithmically proportional to the electric field magnitude. In the substrate, there is a semi-circular electric field that drives holes photogenerated in the positive domain of the substrate (99.8% of absorption occurs in the substrate) across the domain boundary and towards the solid interface in the negative domain. This results in a greater than four orders of magnitude difference in the hole concentration near the solid interface in the positive domain compared to in the negative domain. Within the film on the negatively polarized substrate, the electric field actually drives holes away from the surface and back towards the solid interface, but the high hole concentration near the interface leads to diffusion currents that results in a net hole current at the surface.

The lateral hole currents across the domain boundary are quantified in Figure 5.3b, with hole transfer from positive to negative domains defined as negative lateral hole current and transfer from negative to positive domains defined as positive lateral hole current. Transfer from positive to negative domains is considered favorable, because it contributes to decreasing recombination and separating oxidation and reduction reactions

to oppositely polarized domains. The lateral transfer throughout the substrate is entirely favorable and peaks near a depth of 50 nm (with a magnitude of 250 mA cm^{-2}) before attenuating to negligible lateral transfer at a depth of 400 nm. There is net lateral transfer of holes in the opposite direction in most of the film, representing unfavorable (leakage) current. Though the electric field direction from Figure 5.3a favors hole transfer from positive to negative domains within the film, the diffusion current dominates and there is a net leakage across the film boundary. However, this leakage transfer is significantly lower than the favorable boundary transfer of holes from positive to negative domains throughout the substrate depth.

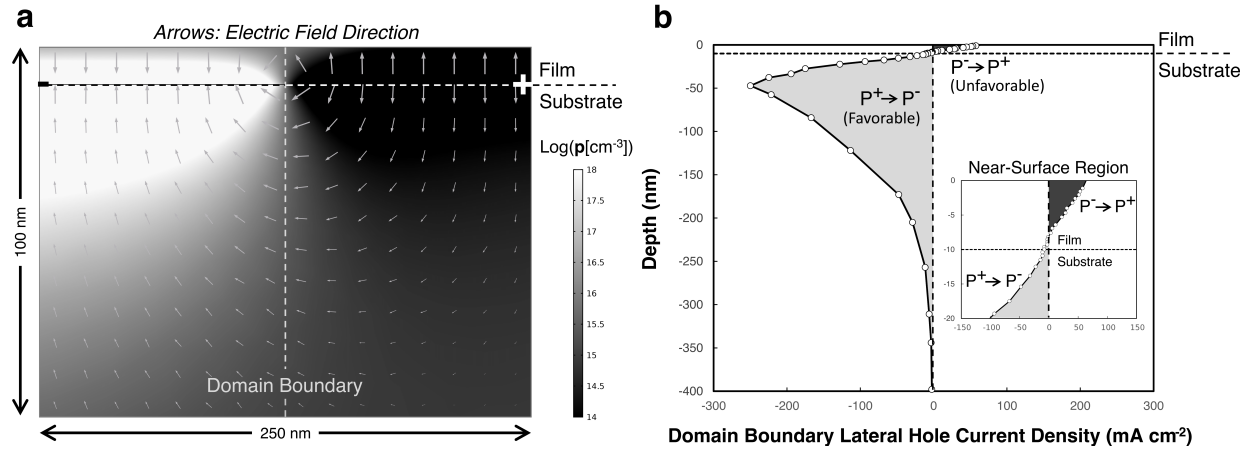

Figure 5.3: (a) Simulated steady-state hole concentration distribution at V_{OC}^{*} in the vicinity of a domain boundary between 250 nm wide negative and positive (half) domains. Arrows indicate the spatial variation of the electric field direction (acting on a positive charge), with the length of the tail being logarithmically proportional to the electric field magnitude at each coordinate. (b) Variation in the lateral hole current density (J_p^x) at the domain boundary with depth. Negative J_p^x values correspond to hole transfer from positive to negative domains and positive J_p^x values represent hole transfer from negative to positive domains.

It is evident from Figure 5.3 that the polarization gives rise to a strong driving force for charge transfer across domain boundaries, which enables an efficiency that is not limited by a Z-scheme. Table 5.1 summarizes the variation in the surface average hole current density and corresponding limiting IQE for different multiples of the $BaTiO_3$ polarization magnitude. There is a significant increase in the IQE from the zero polarization case for even one quarter of P_{BTO}. The IQE increases with increasing polarization but with diminishing returns as the polarization increases.

With the minority carrier transfer between domains being of extreme importance in producing high efficiencies, it is important to evaluate how the domain width affects this transfer. Figure 5.4a displays the surface average hole current density for a variety of different domain widths, spanning two orders of magnitude from 10 to 1,000 nm. The Z-scheme line marks the value (90 mA cm^{-2}) that represents half of the 1D simulated performance for a negative domain (180 mA cm^{-2}). For very low domain widths, J_p^{avg} is below the Z-scheme line. The surface average hole current sharply increases with increasing domain width before reaching a peak value near 180 mA cm^{-2} (the 1D J_p for a negative domain). There is a wide range of physically reasonable domain widths, including 100 – 400 nm, that are above 90% of the maximum value, including the 250 nm domains used to produce 5.2 & 5.3. As the domain width is increased further, the surface average hole current gradually decreases. It is expected that J_p^{avg} will eventually approach the Z-scheme line for sufficiently wide domains, representing the width at which any lateral transfer at domain boundaries no longer has a significant impact on the surface average currents. Nevertheless, even at 1 μm domain widths, the IQE is still above the Z-scheme value.

Table 5.1: Variation in Surface Average Hole Current and Corresponding IQE with Polarization Magnitude

	$P_{BTO} = \pm 26\ \mu C\ cm^{-2}$				
	0	**$0.25P_{BTO}$**	**$0.5P_{BTO}$**	**P_{BTO}**	**$2P_{BTO}$**
J_p^{avg} (mA cm^{-2})	54	100	130	180	220
IQE (%)	21	38	50	69	84

An analysis of the electric potential variation across the solid interface for small domain widths provides an explanation for the decreasing surface average hole current below a width of 100 nm. The oppositely oriented polarization-induced electric fields, when placed in close proximity, partially cancel each other out for very narrow domains, as can be seen in Figure 5.4b for 10 nm domains. The difference in electric potential measured at the solid interface (where the polarization is applied) between the center of negative and positive domains is only 0.17 V for a 10 nm domain, compared to 0.60 V for a 250 nm domain, shown in Figure 5.4c. As is evident from Figure 5.4d, the electric potential difference between negative and positive domains is the same (0.60 V) for 1,000 nm wide domains as it is for 250 nm domains, with the only difference in electric potential being that the boundary region transition is sharpened for 1,000 nm domains. This illustrates that, as the domain width is increased, the difference in electric potential quickly reaches a maximal value (0.6 V in this simulation).

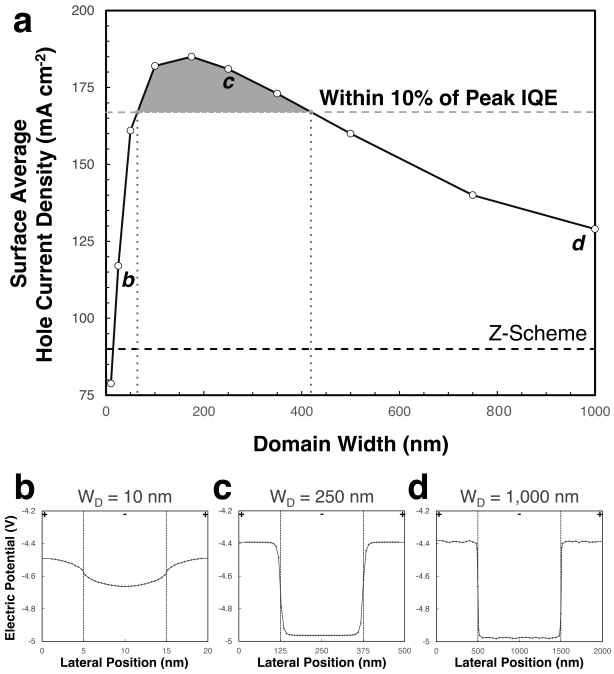

Figure 5.4: (a) Simulated dependence of the surface average hole current density on domain width at V_{OC}^{*}. (b) Electric potential variation with lateral position for 10, 250, and 1,000 nm domain widths.

The effects of decreasing electric potential gradients for narrower domains and lower values of lateral currents across domain boundaries for wider domains are balanced within the shaded region in Figure 5.4a, where the currents are above 90 % of the 1D value. It should be noted that the minority carrier lifetime, which was fixed in this work, will affect the recombination rate at the larger domain sizes, resulting in a decreased IQE with a decreasing lifetime.

The simulations thus far show that the multidomain IQE greatly exceeds a pure Z-scheme performance and that 250 nm domains are the near-optimal domain width (for the values investigated). In the previously reported 1D simulations,[129] the IQE was a strong function of the applied potential. The data presented thus far in the 2D model was

simulated at -0.3 V vs. SCE, the estimated illuminated open-circuit potential. However, at this potential, the electron current magnitude far exceeds the hole current magnitude (as shown in Figure 5.2), and the hole current is the limiting half reaction. If the anodic bias is increased until the surface average currents become nearly equal, a more optimal performance can be obtained. In the 1D model, application of a small anodic potential resulted in an IQE of over 90%.[129]

The absolute value of the electron and hole current densities for 250 nm domains are displayed in Figure 5.5 at an optimal potential (V_{opt}) of -0.135 V vs. SCE (+0.165 V vs. V_{OC}^{*}). The electron current is significantly lower in magnitude but takes the same general shape as in Figure 5.2d, with the highest current being near the domain boundaries.

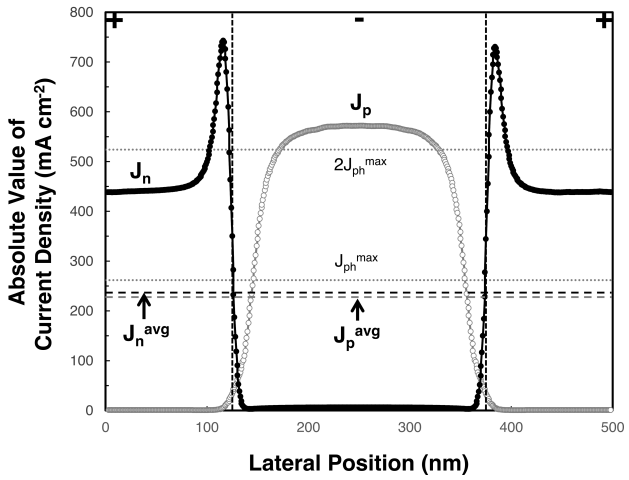

Figure 5.5: Simulated electron (J_n) and hole (J_p) currents across the surface for 250 nm domains at V_{opt}.

The surface average electron current density magnitude is reduced to 240 mA cm^{-2}. The surface average hole current density magnitude is increased to just below that of electrons, at 230 mA cm^{-2}. At this more positive voltage, the hole current density actually

exceeds $2J_{ph}^{max}$ at the center of the negative domain (this is possible because the current density does not take the precise shape of a step function). At this voltage the electron and hole currents are nearly equal and the limiting (hole) current has been increased, resulting in an enhanced IQE of 88%. The voltage adjusted IQE is 76%, which still exceeds the open circuit values. In a particulate photocatalyst, the optimal potential can be achieved by changing the solution pH to achieve and operate at the full efficiency.

In Table 5.2, a summary of the surface average electron and hole current densities is compared with corresponding 1D results at both V_{OC}^{*} and V_{opt}. The 1D currents were obtained by using a modified version of the previously described model,[129] and were determined separately for individual negative and positive domains.

Table 5.2: Comparison of Hole Currents for 1D (Single Domain) and 2D (Multi-Domain, 250 nm Domain Width) Simulations at Illuminated Open-Circuit and Optimal Voltages

		Voltage vs. SCE (V)	
		-0.3 (V_{OC}^{*})	**-0.135 (V_{opt})**
J_n (mA cm^{-2})	1D J_n (P^+)	-39000	-250
	2D J_n^{avg}	-23000	-240
J_p (mA cm^{-2})	1D J_p (P^-)	180	240
	2D J_p^{avg}	180	230
2D IQE (%)		69	88

At the estimated illuminated open-circuit potential, the surface average electron current in 2D is slightly more than half of the 1D value for a positive domain, whereas the surface average for holes in 2D is equal to the 1D value for a negative domain. This results in an overall IQE, limited by the oxidation reaction, of 69%. At the optimal voltage, both the electron and hole surface average currents (in 2D) are marginally below their 1D single

domain values, and the overall IQE is increased to 88%. When the slightly higher performing peak domain width (175 nm) is extracted from Figure 5.4a and evaluated at -0.135 V vs. SCE, a 2D limiting IQE of 90% is obtained. Therefore, by optimizing the domain width and potential, oxidation and reduction reactions can be spatially separated on adjacent oppositely polarized domains with an overall IQE as high as 90%, far exceeding a pure Z-scheme and nearly matching the predicted combined optimal performance of isolated positive and negative domains. A significant percentage of the remaining losses in the system can be recovered by further increasing the carrier lifetime, to values that may be physically achievable.[135] When the lifetime is set to 0.1 s with the potential and domain width optimized, the IQE is increased to 97%.

5.3 Discussion

Coated ferroelectrics that exhibit spatially selective reactivity have the potential to be highly efficient water-splitting photocatalysts by separating the two half reactions on a single surface. Marker reactions, which are primarily qualitative, have been used previously to demonstrate domain-specific reactivity on the surface of thin TiO_2 coatings on ferroelectric $BaTiO_3$.[21] However, the performance of the samples used to produce the data in Figures 5.2a & 5.2b has been estimated to have a limiting IQE below 1%.[129] The spatial separation of oxidation and reduction reactions depicted in Figures 5.2a & 5.2b is evident from the simulated data in Figures 5.2c & 5.2d. The observation that J_p significantly exceeds J_{ph}^{max} throughout much of the negative domain strongly suggests that minority carriers photogenerated in positively polarized regions are being transferred to negatively polarized regions before ultimately being transferred to the surface. A 1D model of a

negative domain (which favors the oxidation reaction) produced a hole current density magnitude of 180 mA cm^{-2}, which is approximately equal to the surface averaged value J_p^{avg} in the 2D model, indicating that roughly the same percentage of photogenerated holes are collected whether the surface is one large negative domain or is divided equally into two 250 nm wide oppositely polarized domains. In this way, the local hole current in the multidomain simulations at the surface of a negative domain is actually much higher than that expected for an isolated negative domain. The limiting IQE is 69% at the illuminated open-circuit potential, a value similar to the 1D case and roughly twice that expected from a Z-scheme. Achieving a high carrier lifetime to enable this greatly enhanced efficiency has recently been shown to be feasible in ferroelectrics.[135] Increases in carrier lifetimes of up to four orders of magnitude were observed in $BaTiO_3$, and were attributed to the reduction in recombination enabled by polarization-induced internal fields.[135] Coupled with the incorporation of a co-catalyst, such as Pt, to improve the reduction kinetics (on the positive domains), these results provide a pathway for designing highly efficient coated ferroelectric photocatalysts.

Figure 5.3 enhances the understanding of the mechanism by which minority carriers photogenerated in positive substrate domains are ultimately collected on the surface above negative domains. Electric fields drive high concentrations of holes across the domain boundary towards the solid interface in negative substrate domains, with diffusion ultimately resulting in hole transfer through the film to generate current. Because the polarization induces these driving electric fields, the magnitude of the polarization (or the component of the polarization oriented along the surface normal) has a large influence on the IQE, as seen in Table 5.1. It is important to note that the polarization dependence is

more significant than that seen for single domains,[129] which is attributable to the significance of lateral polarization-induced electric fields on the results of multidomain simulations. It is evident that the polarization magnitude should be maximized to increase the driving force that results in a higher limiting IQE. This is relevant when considering other materials that have a different spontaneous polarization or even a different source of surface charge, such as the charged terminations in coated $SrTiO_3$ (investigated in Chapters 6 & 7).[16,32]

This finding is also important when considering a more physically realistic coated $BaTiO_3$ surface that does not contain purely 180° domain boundaries with the polarization oriented normal to the surface. Much of the spatially selective reactivity seen in Figures 5.2a & 5.2b is across 90° domain walls. Furthermore, the marker reaction product step heights used to estimate an IQE below 1% were measured across 90° domains.[129] For these domain boundaries, the component of the polarization that is normal to the surface can be compared to the model, though the component that is parallel to the surface may also contribute to the lateral charge transfer (those effects are not modeled here). Considering only the component of the polarization that is normal to the surface, these results suggest that spatial selectivity should be more pronounced across 180° domains than 90° domains. The increase in efficiency from below 1% estimated for the physical samples to 69% for simulated 180° domains at open-circuit can be attributed to multiple factors. The first major factor is a low estimated effective Richardson constant for electrons in the physical samples, which results in electrons severely limiting the overall current at the illuminated open-circuit potential (and all more anodic potentials) when the carrier lifetime is 100 ns.[129] If a reduced effective Richardson constant for electrons had been used in this study,

the minority carrier currents would be largely unchanged, but the majority carrier currents at more anodic voltages would be significantly reduced and there would be no potentials at which such high efficiencies could be achieved. However, minority carrier currents were also estimated to be low at the illuminated open-circuit potential for the reported data on physical samples.[129] The major factor that contributes to the decreased hole currents in the reported physical results may be the predominance of 90° domains across the surface. The electric fields demonstrated in this work that drive minority carriers across 180° domain walls will be oriented differently for 90° domains, and the distance that minority carriers must travel before reaching the surface will likely be much longer. Therefore, the 250 nm domains that are shown here to be nearly ideal, may be wider than optimal for 90° domains. Furthermore, the normal component of the polarization (which drives carriers to the surface to be collected) is reduced for 90° domains, and this in turn may effectively shorten the carrier lifetime, which has been shown to be enhanced by the ferroelectric polarization.[135] Therefore, to produce physical photocatalysts that can achieve the IQEs demonstrated in this work, the kinetics of the majority carrier reaction must be improved and the domain structure must be designed to minimize the distance that minority carriers must travel before reaching the surface while simultaneously maximizing the polarization-enhanced carrier lifetime.

The concentration of majority carrier current near the domain boundaries revealed in Figure 5.2d and Figure 5.5 sheds light on the predicted distribution of marker reaction products on these surfaces. In the simulations, electrons are swept from negative to positive domains (across 180° domain boundaries) due to the strong electric fields, resulting in the region near the boundaries being the most reactive. Highly reactive 180°

domain walls (that are more reactive than the bulk of the domains) have been observed in majority carrier marker reaction experiments conducted on $BaTiO_3$ with and without a TiO_2 coating.[14,22] Enhanced majority carrier reactivity at 180° domain walls has also been observed in another ferroelectric material, $LiNbO_3$, with Ag marker reaction deposits shown to be concentrated at the boundary.[136,137] The enhanced local activity was attributed to the steep gradient in electric field near the boundary, which is evident for coated $BaTiO_3$ as well from Figures 5.4b-d.

With lateral minority carrier currents enabling higher efficiencies, it would be logical to hypothesize that narrower domains may lead to increased performance by decreasing the distance that holes must travel before being collected. These long distances do result in losses for wide domains. However, there are two counteracting phenomena that give rise to the peak observed in Figure 5.4a. The first is that for very small domain widths, the polarizations are in such close proximity that their effects cancel each other. In the limit of infinitesimal domain widths, the surface currents approach the values for zero polarization, which results in a significantly reduced efficiency. The second balancing phenomena is that, the holes photogenerated in positive domains must travel longer distances without recombining, before being collected at the surface of negative domains, as the domain width increases. When the domains are wide enough, relative to the carrier lifetime or diffusion lengths, fewer holes photogenerated in the central region of the positive domains should contribute to the surface averaged current, which results in the decreased surface average hole current for 1,000 nm domains observed in Figure 5.4a. The minority carrier diffusion length, at a 100 ns lifetime, is roughly 250 nm. Minority carriers photogenerated in positive domains must not only be transported across the domain to the

boundary, but must then travel through the depth of the heterostructure to the film surface before being collected. This extended minority carrier transport distance is balanced by the drift forces shown in Figure 3, which are enhanced for wider domain widths. Ultimately, a large range of physically reasonable domain widths from approximately 100 – 400 nm are desired to balance these two effects. Therefore, the results show that the minority carrier current density is maximized approximately where the domain width is equal to the diffusion length.

To increase the IQE beyond 69% for 250 nm domains, the voltage must be optimized to obtain nearly equal electron and hole currents, as shown in Figure 5.5. The limiting IQE is improved to 88% at -0.135 V vs. SCE. The IQE can be optimized further to 90% by using a slightly reduced domain width and up to 97% by increasing the carrier lifetime to 0.1s. These relatively small adjustments to the potential (0.165 V) could be achieved without an external bias (which lowers the overall efficiency and would not be practical for a colloidal catalyst) by altering the pH of the solution to reach the desired electrochemical potential). These multidomain simulations provide a framework for obtaining 90% internal quantum efficiencies in coated ferroelectric photocatalysts. The conclusions supported here can be applied to achieve enhanced internal quantum efficiencies in material systems with higher achievable solar-to-hydrogen conversion efficiencies.

5.4 Conclusions

A 2D COMSOL® model of thin TiO_2 films on ferroelectric $BaTiO_3$ was shown to produce oxidation currents localized on negative domains and reduction currents localized on

positive domains, with an overall efficiency that far exceeds a pure Z-scheme mechanism. The IQE varies by less than 10% over a wide range of domain widths from 100 – 400 nm. When the domain width and potential are optimized, oxidation and reduction currents are spatially separated to adjacent oppositely polarized domains with an overall IQE as high as 90%.

6 PHYSICAL PHOTOELECTROCHEMICAL STUDY OF TERMINATION-SPECIFIC REACTIVITY

6.1 Overview

In Chapters 4 & 5, a computational model was developed and implemented to quantify and optimize the performance of TiO_2-coated $BaTiO_3$ photocatalytic surfaces. Optimization of the applied potential was determined to enable significantly enhanced efficiencies. In this chapter, a similar material ($SrTiO_3$), with an analogous mechanism for promoting spatially selective reactivity,[16,32] is characterized using physical photoelectrochemistry (see Section 3.1) to analyze the voltage-dependence of the photocatalytic performance. Physical photoelectrochemical testing enables direct comparison with the computational model outlined in Section 3.2 to estimate unknowns such as the reactivity parameters ($A^*_{n,p}$), which were shown in Chapter 4 to significantly influence the performance in similar materials. The net Faradaic current across the surface is determined through measurement of the net current through the back contact.

Heavily doped (100) and (111) oriented $SrTiO_3$ single crystals were tested after exposure to different annealing environments to test the hypothesis that the reactivity of the (111) surface varies with annealing environment while the reactivity of the (100) surface has no dependence on the annealing environment. The physical photoelectrochemical results reveal a decreased performance at the illuminated open-

circuit potential after annealing and a significant dependence of the reactivity on the annealing environment for both (111) and (100) annealed surfaces.

6.2 Design

The experimental setup used for the photocurrent measurements can be seen schematically in Figure 6.1. The sample was connected to a potentiostat as the working electrode. The reference electrode used was a saturated calomel electrode (SCE), an electrode that was filled with saturated KCl solution and held a constant potential of 0.244 V vs. the normal hydrogen electrode (NHE).[138] A high-surface area platinum wire was used as the counter electrode, which performed the complementary reaction to that at the working electrode and completed the overall circuit.

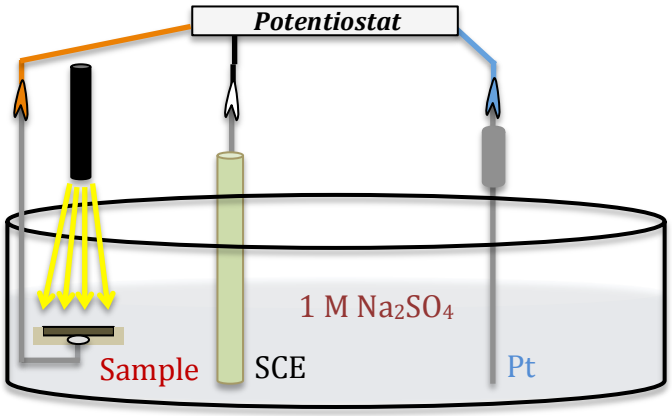

Figure 6.1: Photoelectrochemical Experimental Setup

These three electrodes were connected to the SP-200 potentiostat from Bio-Logic Science Instruments SAS headquartered in Claix, France. The electrolyte used for all testing

was a 1M Na_2SO_4 aqueous solution to provide sufficient conductivity to the electrolyte without introducing redox species that might have been reactive with (corrosive to) the $SrTiO_3$ surface. The electrolyte was regularly refreshed throughout repeated testing.

The lamp used in this work was the model 6255 150 W Xe Ozone Free lamp from Newport Corporation headquartered in Irvine, CA. The output spectrum for this lamp, shown in Figure 6.2, approximated that of the sun, and was thus a UV and visible source.

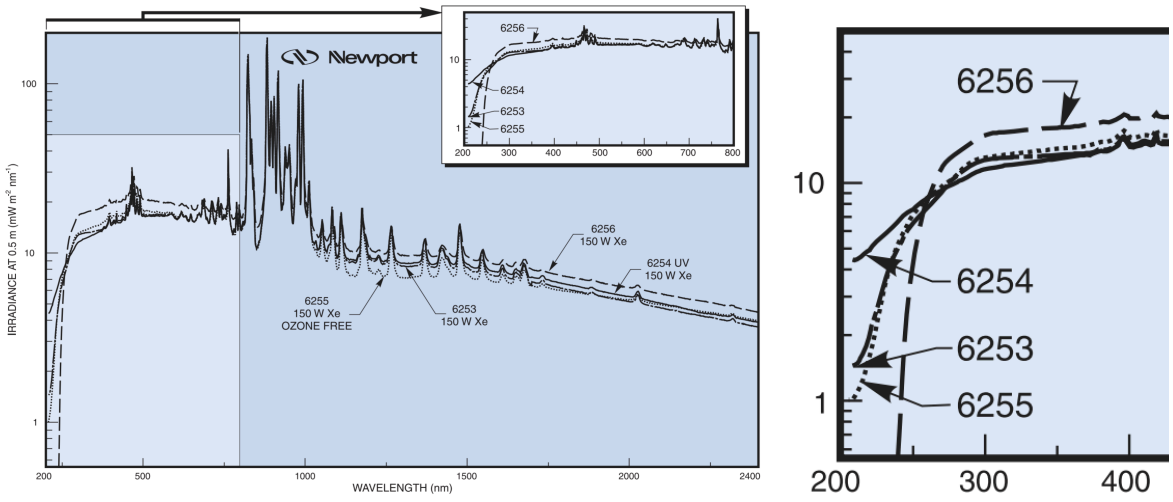

Figure 6.2: Output Spectrum for 6255 150 W Xe Ozone Free Newport Lamp
Figure Reproduced from www.newport.com.

An optical fiber was attached to the lamp and used to illuminate the samples. A collimator was attached to the end of the optical fiber to narrow the beam over the sample area. The experiments were conducted at a separation distance between the edge of the collimator and the sample surface of 8.1 cm. A PS 19 low power thermopile sensor was obtained from Coherent, Inc. headquartered in Santa Clara, CA. and was used to measure the power density at various separation distances.

After fitting the data to an approximately inverse square relationship, a power density of 1,260 W/m^2 was computed for the 8.1 cm experimental separation distance. While this power density is comparable to the approximate irradiance of 1.5G solar irradiation, where 1,000 W/m^2 equates to one sun, the Xe spectrum has notable differences from the solar spectrum. Referencing Figure 2.4, and translating the band gap of $SrTiO_3$ of 3.2 eV to a wavelength of around 390 nm, the maximum efficiency for a Xe lamp without a water filter (no water filter was used here) is relatively similar to that of an AM 1.5G solar output. What this means is that, for a band gap of 3.2 eV, the ratios of super-band-gap radiation to sub-band-gap radiation are similar for the two sources compared in Murphy et al.,[46] the study that produced Figure 2.4. However, it is important in this work to compare the efficiencies of the solar irradiance and the specific Xe lamp used, since the irradiance (particularly in the UV region) for Xe lamps can vary widely and the lamp's performance changes with extended use.

The parameter of interest, for both the calculation of efficiencies based on physical photoelectrochemical tests and for input as the relevant irradiance in the simulations of Chapter 7, is the combined irradiance of photons more energetic than the band gap of $SrTiO_3$, as opposed to the total irradiance incorporating all wavelengths reported above. Using detailed tables of the lamp irradiance from Newport and the reported detection range of the Coherent sensor, it was determined that approximately 10% of the irradiance from the Xe lamp in the detectable range of the PS 19 sensor was energetic enough to be absorbed by $SrTiO_3$. Therefore, 10% of the total detected power density of 1,260 W/m^2, or 126 W/m^2, was the irradiance that could be used to evaluate the EQE of the device. Traditionally, the EQE is measured by separating the light source beam by wavelength and

measuring the current output when the sample is exposed to a single monochromatic wavelength (or more practically a narrow range of wavelengths). Since the EQE measures reacted carriers per photon, the number of photons must be determined by knowing both the irradiance and the energy of each photon present to compute the area flux of photons. This is a straightforward process when the photons present all have the same energy, but is difficult to compute for a large range of photon energies. In this work, because of the relatively narrow band of wavelengths emitted by the source that can be absorbed by $SrTiO_3$, both for simplicity and ease of comparison to the simulations, the 126 W/m^2 were approximated to be monochromatic for calculations and simulations with a representative photon energy of 3.82 eV determined from detailed analysis of Figure 6.2.

This approximate EQE is the most relevant efficiency to calculate from the physical experimental data, since it reveals how well the device converted absorbed energetic photons into reacted charge carriers. This efficiency is, therefore, independent of the ratio of sufficiently energetic photons emitted from the Xe source to those that are not energetic enough to be absorbed. The photoconversion efficiency, discussed in Section 2.4, would strongly reflect the specific spectral output of the Xe lamp used, which was not easily related to other literature reports and industry goals. The photoconversion efficiency, which reflects the fraction of the total incident energy that is converted into chemical energy, will be a more valuable tool for computational optimization results.

6.3 Sample Preparation

The samples used in this work were (100) and (111) oriented 0.7 wt% Nb-doped $SrTiO_3$ single crystals obtained from MTI. All samples were cleaned ultrasonically in methanol and acetone before being rinsed with DI water and dried. For the samples to be annealed, three 99.6% alumina crucibles and covers, obtained from AdValue Technology based in Tuscon, AZ, were prepared. The first was not exposed to any pre-treatment and was used as received. The second was coated on the inside with a thin layer of TiO_2 powder, annealed with a cover for 6 hours at 1450 °C, inverted to allow excess powder to settle on the inside wall of the cover, and annealed at 1450 °C for another 3 hours before cooling to room temperature. This same procedure was repeated for the third crucible but with $SrTiO_3$ powder used in place of the TiO_2 powder. One sample of each orientation was then separately placed, polished side up, into each of the three crucibles and individually annealed for 10 hours at 1250 °C. These six annealed samples, for convenience, will be referred to both by their orientation and as being 'AR annealed', 'pre-TiO_2 annealed', or 'pre-$SrTiO_3$ annealed', depending on the crucible used. Another sample of each orientation was placed in the crucible that was pre-annealed with $SrTiO_3$ powder and annealed at 700 °C for 30 minutes (not including heating and cooling times). These two samples will be referred to by their orientations and as being 'pre-$SrTiO_3$ 700 °C annealed'. A final two samples, one of each orientation, were not annealed at all and were simply cleaned with solvents as described above. These samples will be referred to as being 'unannealed'. A summary of the processing for the prepared samples and their abbreviated names is displayed in Table 6.1.

Table 6.1: Summary of Processing Conditions for Nb-doped $SrTiO_3$ Single Crystal Samples Used in this Work

Crystal Orientation	Annealing Temp. (°C)	Annealing Time (hours)	Powder Pre-Annealed in Crucible	Name Given for Reference
(100)	1250	10	None	(100) AR annealed
(111)				(111) AR annealed
(100)			TiO_2	(100) pre-TiO_2 annealed
(111)				(111) pre-TiO_2 annealed
(100)			$SrTiO_3$	(100) pre-$SrTiO_3$ annealed
(111)				(111) pre-$SrTiO_3$ annealed
(100)	700	0.5	$SrTiO_3$	(100) pre-$SrTiO_3$ 700 °C annealed
(111)				(111) pre-$SrTiO_3$ 700 °C annealed
(100)	Unannealed	-	-	(100) unannealed
(111)				(111) unannealed

Each sample was prepared for photoelectrochemical testing by applying a mixed silver paste/paint contact to the unpolished backside, which was then compressed against an exposed copper wire while drying. After establishing the metal contact, non-conducting epoxy was coated over the contact and all exposed material on the back and side edges, leaving only the top polished surface exposed to solution during testing. After allowing the epoxy to dry for a minimum of five hours, the wire connected to the sample was connected as the working electrode, as shown in Figure 6.1, with the exposed polished surface facing up and carefully aligned directly underneath the illumination source.

6.4 Results

Before beginning photoelectrochemical testing, it was important to demonstrate that some extent of spatially selective reactivity (that has been observed previously[16,32] on undoped samples) could be observed using marker reactions on such heavily doped samples. The experimental setup used for this preliminary testing, shown in Figure 6.3, is replicated from past work in our group for consistency.[16,32] The sample was fixed to a glass slide with

the polished side faced upward. An O-ring was placed on top of the sample, which was filled with a large droplet of the test solution. A quartz cover slip was placed over the solution to keep it in place near the sample surface and to allow illumination from a lamp to shine through onto the sample.

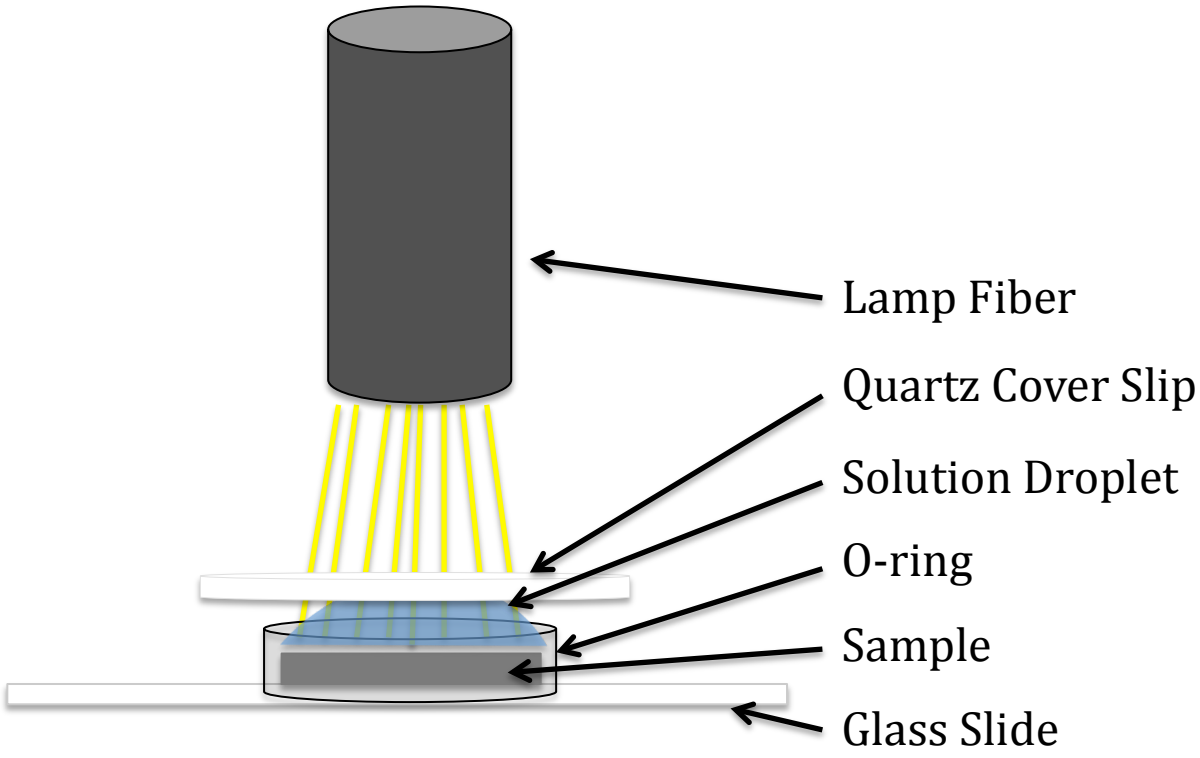

Figure 6.3: Marker Reaction Experimental Setup

The lamp used was a 300 W Hg lamp with a separation of approximately 1 cm and a reaction exposure time of 10 seconds. The test solution used in this experiment was 0.115 M $AgNO_3$ (reduction reaction). After the marker reaction was complete, the sample was rinsed in DI water and dried with compressed air. They were immediately characterized by AFM to prevent contamination of the surface from interfering with the measurement.

Silicon probes obtained from Ted Pella, Inc. in Redding, CA were used in a Solver NEXT AFM from NT-MDT based in Moscow, Russia for the characterization.

Immediately after annealing a (111) Nb-doped $SrTiO_3$ single crystal at 1250 °C in the pre-$SrTiO_3$ annealed crucible (see Section 6.3 for the annealing procedure), the sample was tested for the reduction marker reaction in $AgNO_3$ solution to observe whether the doped samples also exhibited spatial selectivity of reaction sites on the surface. An AFM image of a 30 x 30 μm^2 section of the surface after annealing and before reaction is shown in Figure 6.4.

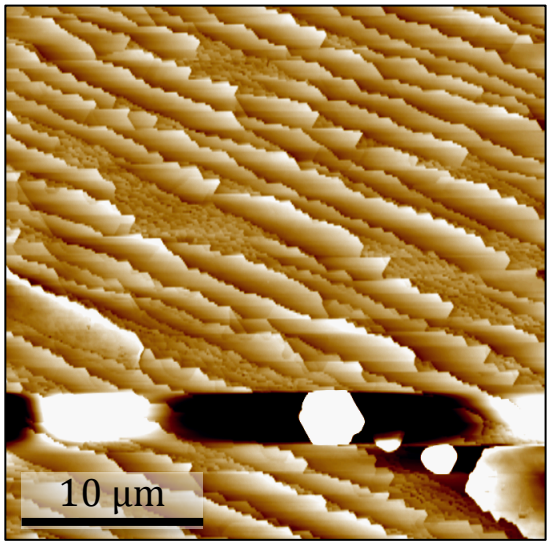

Figure 6.4: Topographic AFM Image of Pre-$SrTiO_3$ Annealed (111) 0.7 wt% Nb-doped $SrTiO_3$ Before Reaction

Terraces are visible on the surface of the (111) sample after extended annealing, as expected. The large white spot on the image is representative of a relatively thick object on the surface, which is likely a dust particle. The topographic AFM images display features higher in a direction normal to the surface as brighter and features lower on the surface as darker contrast.

To test if the Nb-doped samples show spatial selectivity, the sample was exposed to $AgNO_3$ under illumination from a Hg lamp and allowed to react for 10 seconds before the lamp was turned off. AFM images registered from different areas on the sample surface after the marker reaction are shown in Figure 6.5.

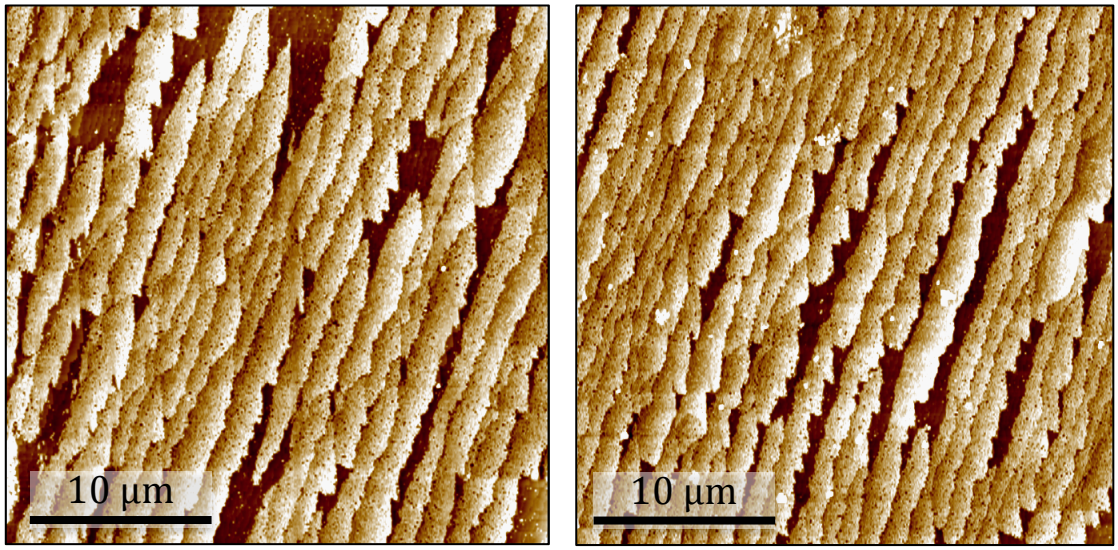

Figure 6.5: Topographic AFM Images of Pre-$SrTiO_3$ Annealed (111) 0.7 wt% Nb-doped $SrTiO_3$ After Reaction in 0.115 M $AgNO_3$ (Different Areas of the Surface)

The bright contrast represents areas where Ag reaction products have been deposited and the dark areas are unreactive terraces. The majority of the surface is reactive, but there is still some spatial selectivity of reaction products. To help confirm that the contrast in the images is, in fact, due to deposited marker reaction products, the sample was sonicated in methanol for 20 minutes, which should remove any Ag on the surface. The AFM image in Figure 6.6 shows that the surface has been cleaned of the reaction products by the solvent treatment as no significant contrast remains in the image except for that from the native terraces (it is similar to Figure 6.4).

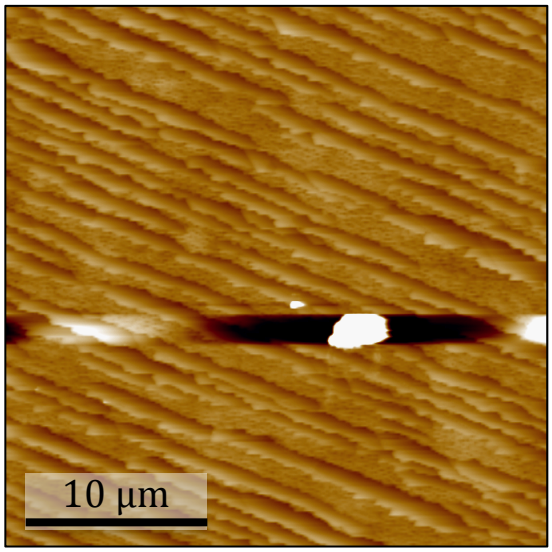

Figure 6.6: Topographic AFM Image of Pre-$SrTiO_3$ Annealed (111) 0.7 wt% Nb-doped $SrTiO_3$ After Reaction in 0.115 M $AgNO_3$ Followed by Methanol Ultrasonic Cleaning

It appears that the surface of the (111) Nb-doped $SrTiO_3$ surface does exhibit spatially selective reactivity with the vast majority of terraces being active for the reduction marker reaction after pre-$SrTiO_3$ annealing. Published marker reaction results on undoped samples[32] demonstrated surface coverage percentages of photocathodic terraces that varied with the annealing environment, with a higher percentage of terraces active for Ag reduction when annealed in air (55%) or in the presence of high concentrations of $SrTiO_3$ mixed with TiO_2 (45%) compared to in the presence of high ratios of TiO_2 to $SrTiO_3$ (14%). However, the percentage of photocathodic terraces for the heavily doped sample in Figure 6.5 appears to exceed that of all undoped samples reported (which never exceeded 55%).[32]

Before generating current-voltage plots for each sample, it is important to determine the open-circuit voltage of the measurement both in the dark and under

illumination. In theory, this measurement when taken in the dark should be independent of the sample used, so long as the sample was able to reach equilibrium with the solution and the electrochemical potential near the surface could be measured at the back contact. The semiconductor Fermi level would equilibrate to the electrochemical potential of the solution as charge carriers are exchanged at the surface. The blue curve in Figure 6.7 shows this equilibration over time in the dark at the surface of an unnanealed (100) Nb-doped $SrTiO_3$ single crystal. The open-circuit potential (V_{oc}) ultimately reaches a value of 0.13 V vs. SCE, which is representative of the electrolyte.

The red curve in Figure 6.7 represents the same measurement repeated with the Xe lamp turned on, illuminating the sample. There is a significant change in the potential to more negative values (which can be equated to the Fermi level moving up on an energy diagram) and a final value was reached in much less time than when the measurement was performed in the dark. The value of the illuminated open-circuit voltage (V_{oc}^*) for this sample is approximately -0.57 V vs. SCE. The difference between the open-circuit potential in the dark and under illumination is a measurement of the photovoltage, which was ≈ 0.7 V in this work.

While V_{oc} is largely dependent on the electrolyte, V_{oc}^* (under illumination) is dependent on the spectrum of the source, the proximity of the source, the light absorbing properties of the semiconductor, and the carrier concentrations near the surface. The photovoltage lifts the Fermi level for an n-type material and reduces the upward band bending at the surface due to the high density of photogenerated carriers near the surface. This state under illumination is a non-equilibrium condition, and the Fermi level in the semiconductor is separated from the solution level. In this way, the photovoltage can be

thought of as an additional bias applied to the semiconductor under illumination, and V_{oc}^* (illuminated open-circuit potential) is the value that will be of most interest for evaluating efficiencies. Any additional bias that must be applied to the system to increase performance must be measured relative to V_{oc}^*.

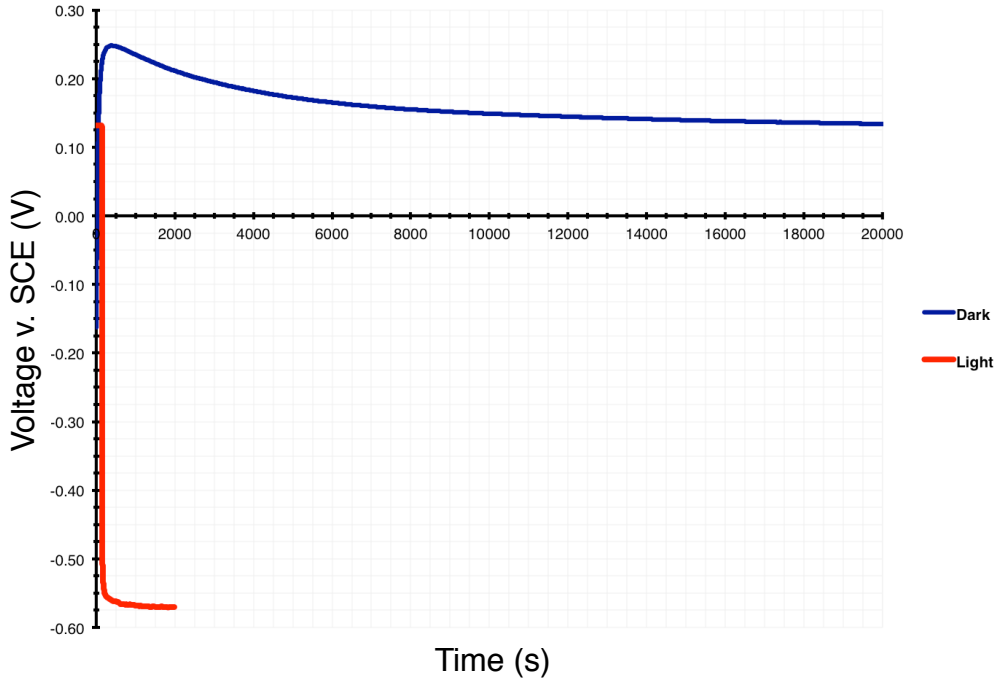

Figure 6.7: Open-Circuit Voltage Measurement for Unannealed (100) Nb:$SrTiO_3$ in 1 M Na_2SO_4

To unveil the performance at V_{oc}^* and at other voltages, the I-V characteristic must be measured for each sample. Unless otherwise noted, the data shown here was taken by sweeping the potential of the sample from cathodic to anodic biases at a rate of 10 mV/s with the Xe lamp illuminating the sample and measuring the current at each potential step. Figure 6.8 shows the I-V characteristic for the (100) unannealed sample both under illumination and in the dark. Fundamentally, it resembles the shape of the theoretical plot

given in Figure 3.1. The light and dark current densities are nearly equal in the cathodic region, and as the potential is swept in the anodic direction to more positive values, anodic hole current onsets under illumination and ultimately saturates at high anodic bias. A small feature after the onset near -0.7 V vs. SCE was observed, which could be attributed to a variety of factors that cannot be resolved without further testing. The current at V_{oc}^{*} (-0.57 V vs. SCE) is relatively small compared to the saturated value, and can be increased significantly with applied bias.

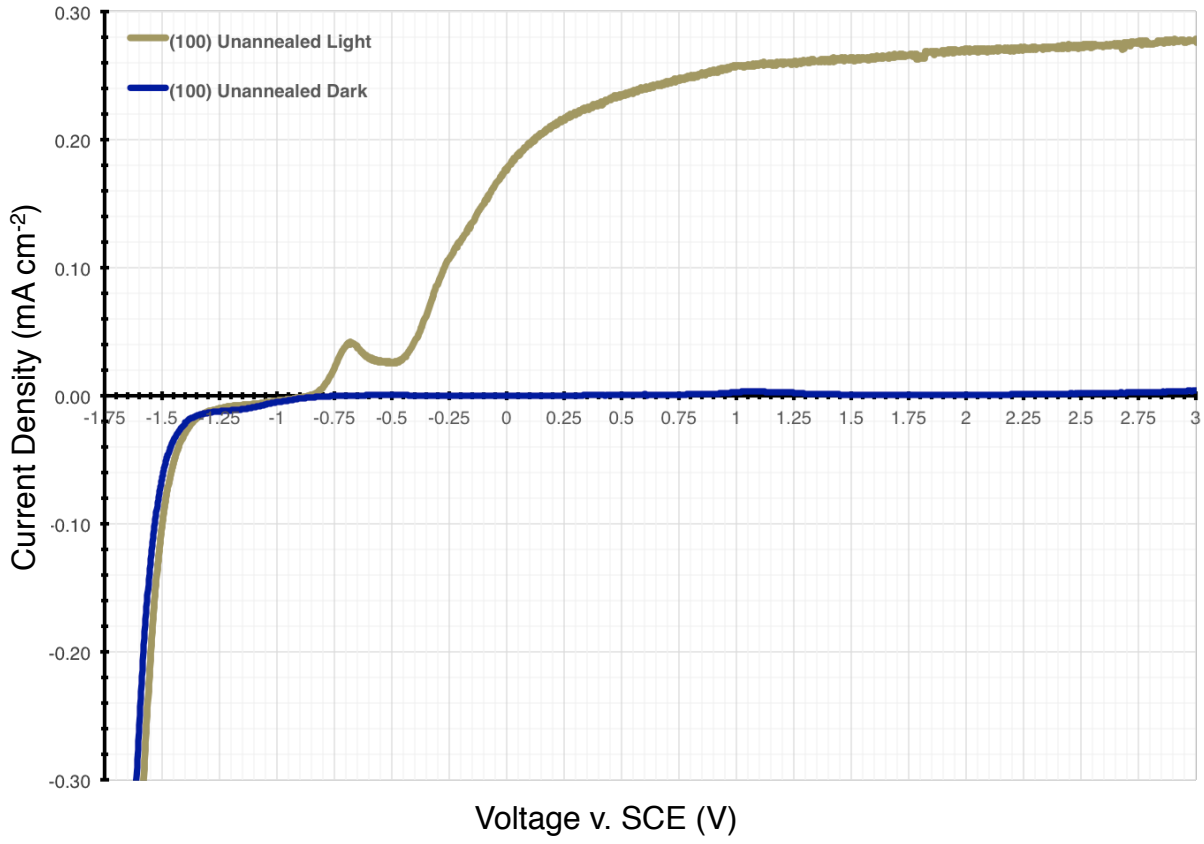

Figure 6.8: Measured Current-Voltage Characteristic for (100) 0.7 wt% Nb-doped $SrTiO_3$

The onset occurs close to the expected value for the material that can be calculated for the experimental electrolyte used here based on measured values by Butler & Ginley for reduced $SrTiO_3$.[51] Changes in E_{fb} as a result of the specific doping level and preparation are not expected to be revealed through current-voltage measurements, which are not the most precise in measuring flat-band potentials. Nevertheless, the similar onset potential and the general accordance of the shapes of the cathodic and anodic current suggest a good contact to the material and a reasonably well performing photoanodic surface.

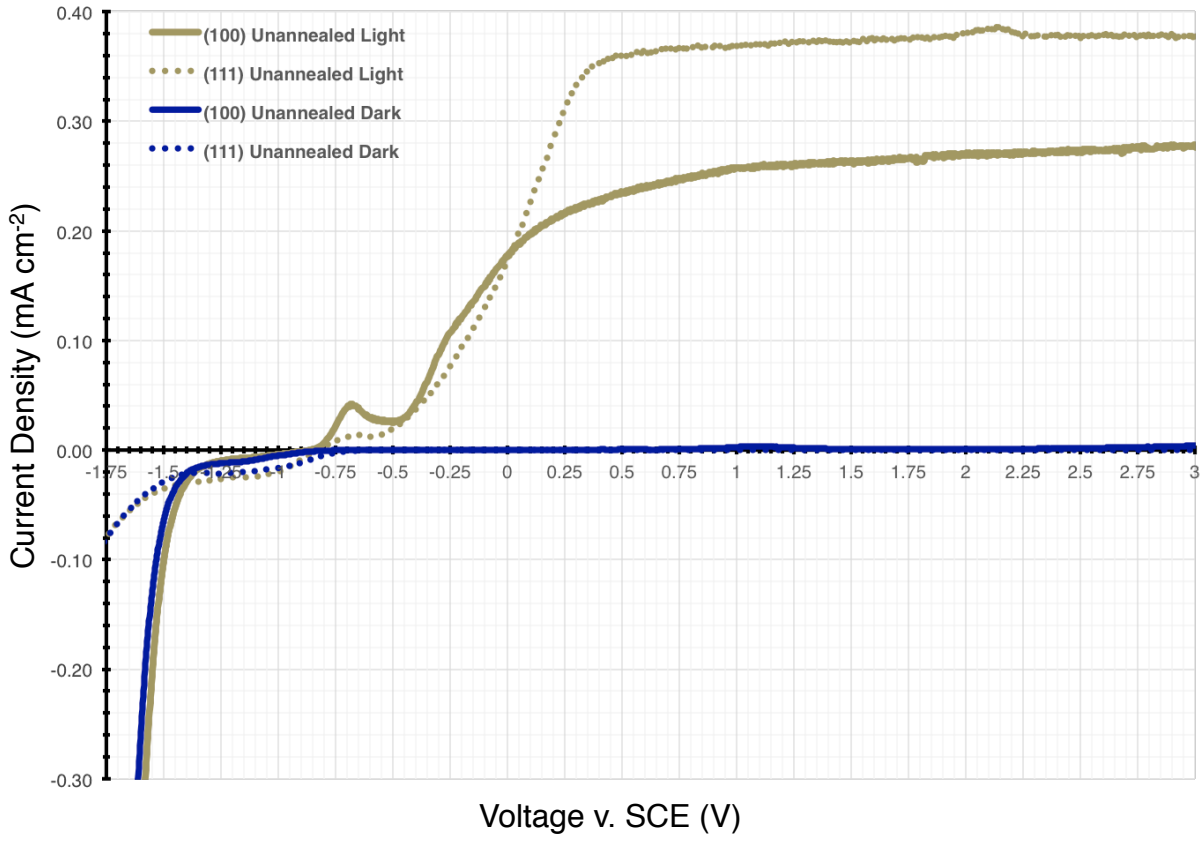

Figure 6.9: Measured Current-Voltage Characteristics for (100) and (111) 0.7 wt% Nb-doped $SrTiO_3$

Figure 6.9 shows the I-V plot of the (111) unannealed sample compared with that of the (100) unannealed sample from Figure 6.8. The saturated anodic current values are relatively different, but this is very likely a result of improved lateral alignment techniques of the illumination source beam and the sample surface that were adopted after the initial measurements on the (100) unannealed sample. The observations of most importance are that the (111) sample shows less cathodic current, similar points of cathodic and anodic onset current (flat-band potential), and similar slopes of the onset of anodic photocurrent relative to the (100) sample.

The surfaces of these two unannealed samples have, with the exception of ultrasonic solvent cleaning, not been altered since being grown, polished, and transported. A relatively low temperature annealing should serve to clean up the surface and remove some of the imperfections from the polishing and transportation processes. The I-V characteristics for both orientations after annealing for 30 minutes at 700 °C is shown in Figure 6.10, with the unannealed sample data displayed for comparison.

Dotted lines correspond to the (111) orientation while solid lines are used for (100) samples. The colors separate samples by annealing with the red curves being for unannealed samples and the dark purple being for samples pre-$SrTiO_3$ annealed at 700 °C. The annealed samples exhibit sharper onsets than the unannealed samples, allowing them to reach saturated values with less applied anodic bias. The onset potentials and approximate saturated photocurrent values are largely unchanged by the pre-$SrTiO_3$ annealing. It was thought that annealing in the pre-$SrTiO_3$ crucible might lead to significant differences in the I-V plot for the (111) orientation due to the preferential growth of

terraces with specific terminations on the surface. However, this is not observed, potentially due to the short annealing time and relatively low temperature.

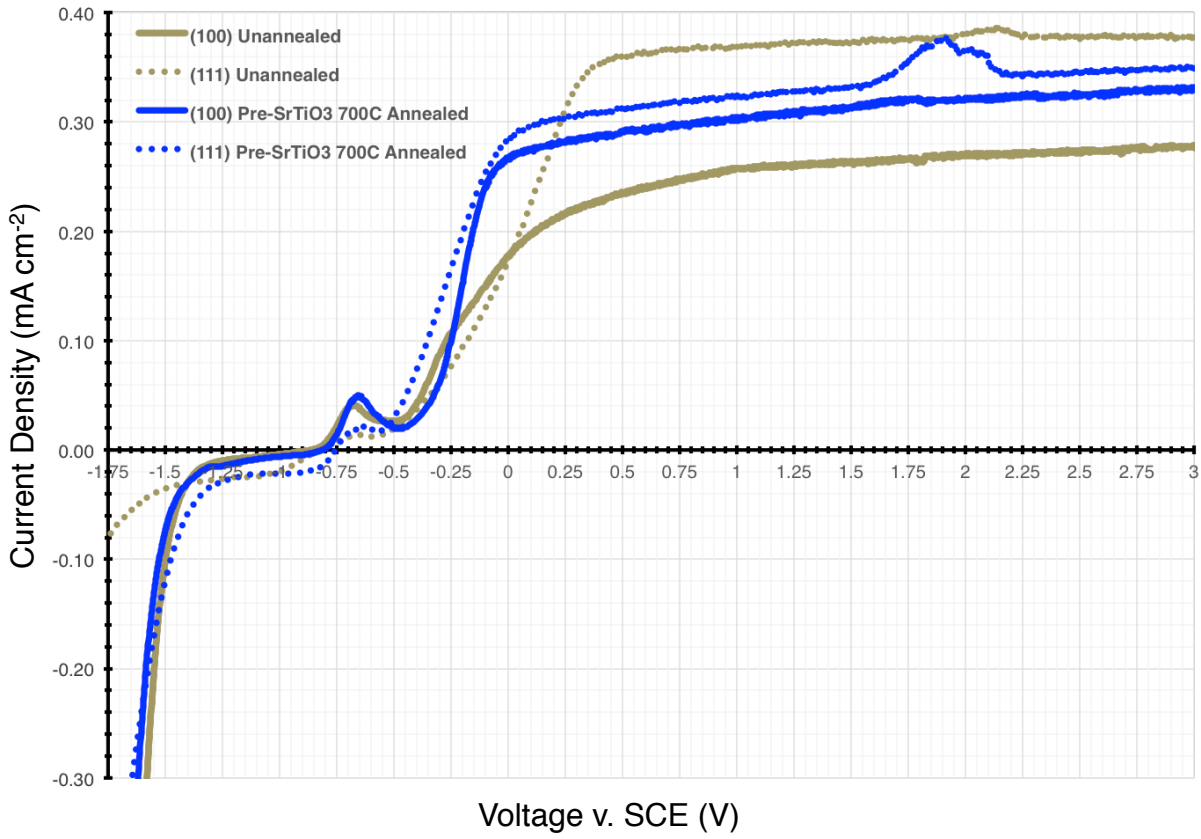

Figure 6.10: Measured Current-Voltage Characteristics for (100) and (111) 0.7 wt% Nb-doped $SrTiO_3$ Annealed at 700 °C in Crucible Pre-Annealed in $SrTiO_3$

Annealing at higher temperature (1250 °C) and for longer time (10 hours) should be sufficient to observe any more significant effects of the annealing. Figure 6.11 shows the measured current-voltage data for (100) and (111) pre-$SrTiO_3$ samples annealed at 1250 °C. The data for the (111) unannealed sample is also shown for comparison to directly observe the effects of the annealing.

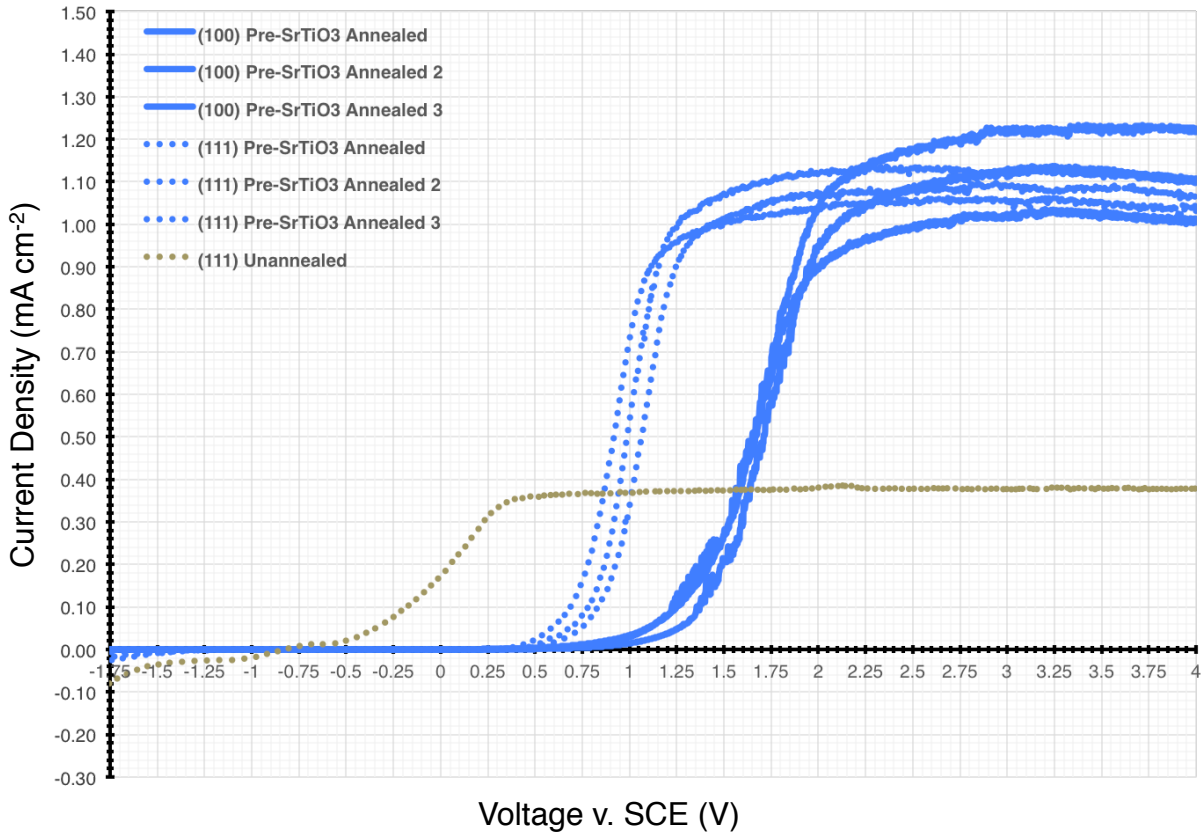

Figure 6.11: Measured Current-Voltage Characteristics for (100) and (111) 0.7 wt% Nb-doped $SrTiO_3$ Annealed at 1250 °C in Crucible Pre-Annealed in $SrTiO_3$

For both pre-$SrTiO_3$ annealed samples (one of each orientation), three different curves are shown, which were taken after dismantling and re-establishing the setup every time for each sample, as a means of demonstrating the reproducibility of the measurement. This serves as a display of the inherent error in the measurement resulting from connections and alignment, such that only observations beyond the error are considered.

Relative to the (111) unannealed curve, which is representative of the approximate saturated photocurrent and onset potential of unannealed and low temperature annealed samples of both orientations (see Figure 6.10), the pre-$SrTiO_3$ annealed samples exhibit

much more anodic apparent onset potentials and more than double (and up to three times) the saturated photocurrent magnitude at high anodic bias. The (111) sample exhibits a more cathodic onset relative to the (100) sample, reaching a nearly saturated current value roughly 1.75 V apart.

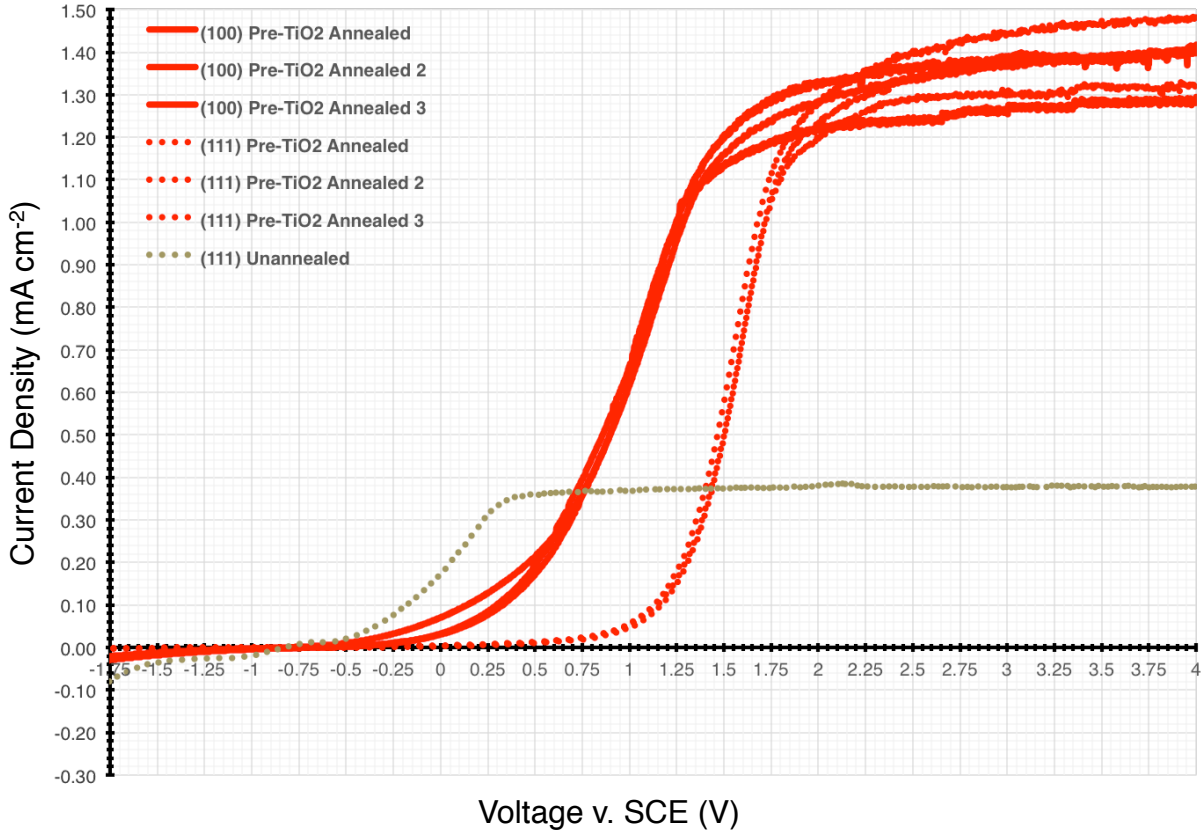

Figure 6.12: Measured Current-Voltage Characteristics for (100) and (111) 0.7 wt% Nb-doped $SrTiO_3$ Annealed at 1250 °C in Crucible Pre-Annealed in TiO_2

The (111) pre-$SrTiO_3$ annealed sample also reaches a nearly saturated photocurrent (albeit at a higher value) 1 V positive of the unannealed (111) sample. The extreme increase for both orientations in saturated value could lead to much more efficient devices. However, the onset is so far anodic of the open-circuit potential under illumination of -0.57

V vs. SCE that any increase in photoconversion efficiency is nullified by the need for significant applied bias. Nevertheless, it is worth investigating the cause of the increase and the effect of other annealing conditions on the onset potential for different orientations.

The results for the pre-TiO_2 annealed samples are displayed in Figure 6.12. For this annealing environment, the (100) orientation has a more anodic onset than the (111) sample, which is the reverse of what was observed for the pre-$SrTiO_3$ annealed samples. However, both pre-TiO_2 annealed samples similarly reach a much higher saturated photocurrent magnitude relative to the unannealed and low temperature annealed samples.

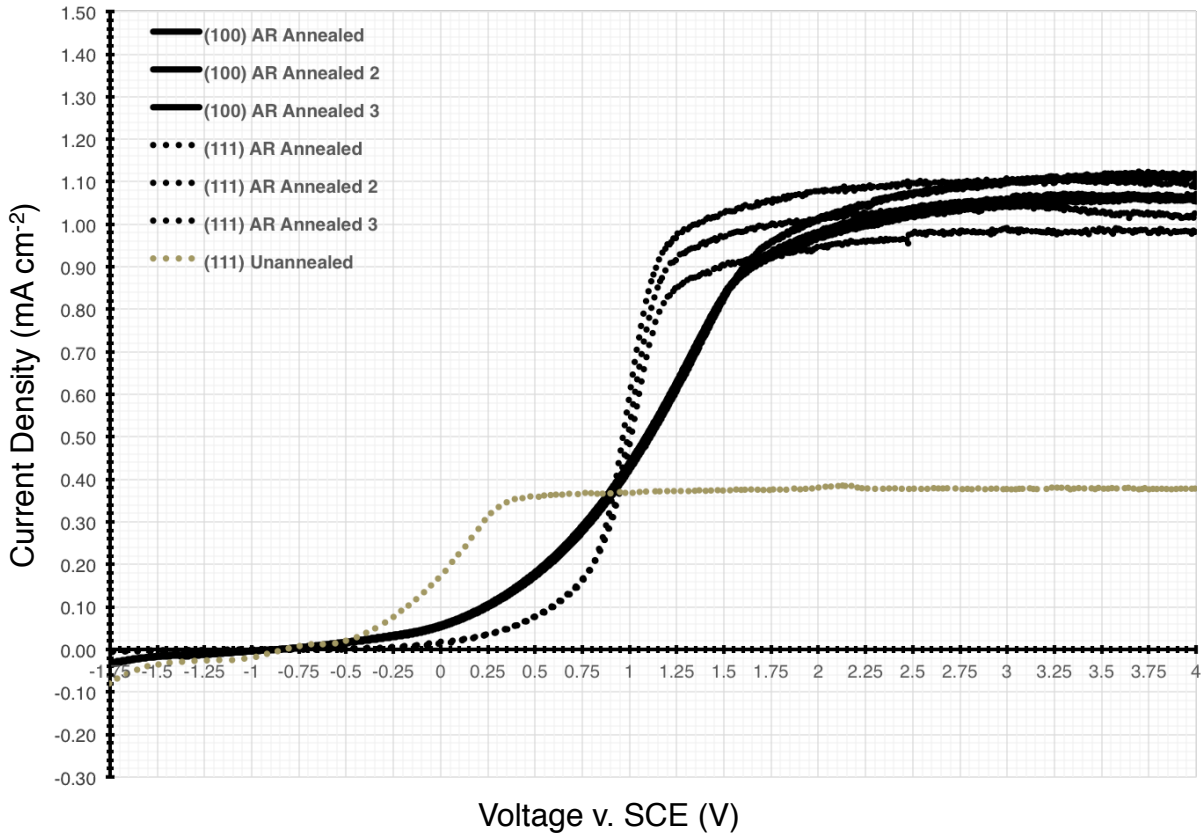

Figure 6.13: Measured Current-Voltage Characteristics for (100) and (111) 0.7 wt% Nb-doped $SrTiO_3$ Annealed at 1250 °C in As-Received Crucible

The final 1250 °C annealing environment tested in this work is AR annealed, the results of which are found in Figure 6.13. The two samples exhibit a similar anodic onset shifting and increase in saturated photocurrent magnitude consistent with the other four samples annealed at 1250 °C in different environments. For the AR annealed samples, the curves for each orientation are relatively similar. The (100) sample exhibits an earlier onset close to the potential of the unannealed samples but has a long, somewhat linear, onset before reaching saturation. The (111) AR annealed sample seems to have a slightly later onset that is slow at first and then a sharp increase to near-saturation starting around 0.8 V vs. SCE.

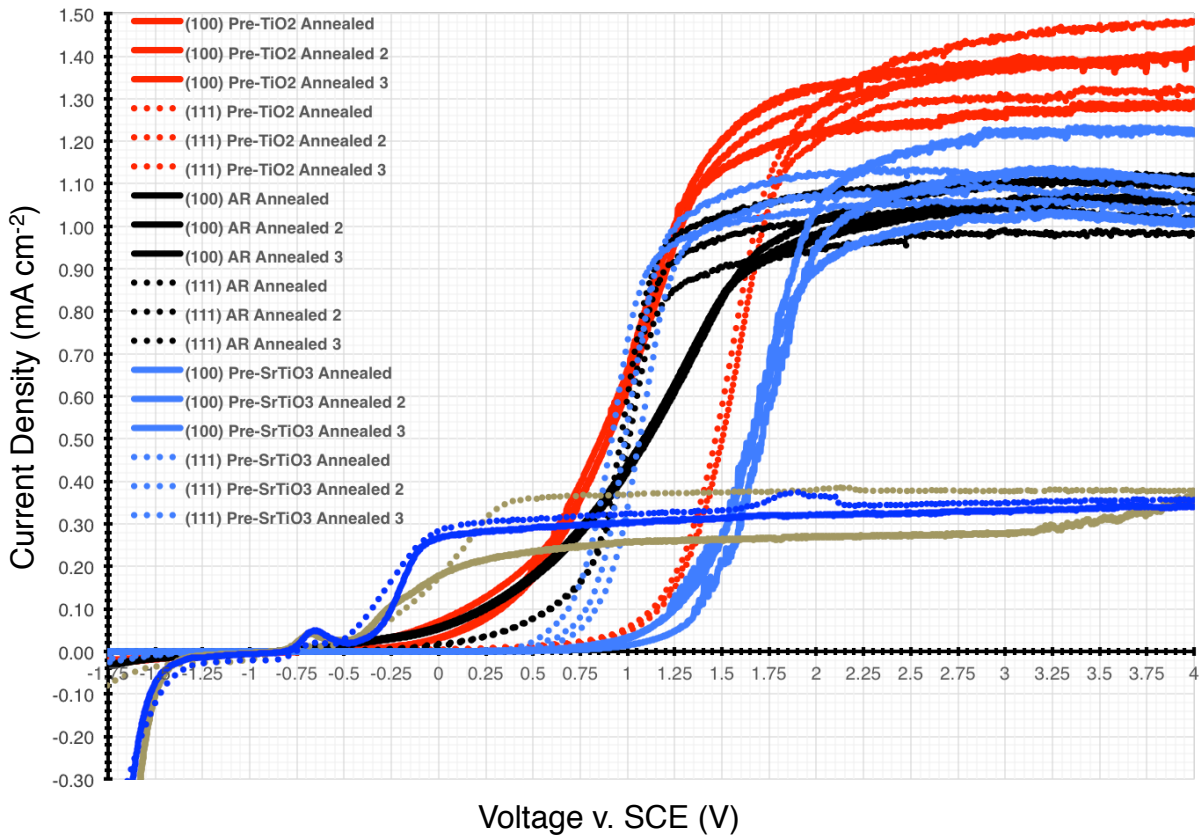

Figure 6.14: Measured Current-Voltage Characteristics for All 0.7 wt% Nb-doped $SrTiO_3$ Samples

To compare the different annealing environments and orientations, the data from above is consolidated into Figure 6.14. The saturated anodic photocurrents for the samples annealed at 1250 °C are more than double those of the unannealed and 700 °C annealed samples. The saturated photocurrent appears to be slightly higher for the pre-TiO_2 annealed samples of both orientations relative to the pre-$SrTiO_3$ and AR annealed samples. All of the high temperature annealed samples appear to have less cathodic current, at least at the potentials tested here, than the unannealed and low temperature annealed samples.

Among the 1250 °C annealed samples, there appears to be a wide array of onset potentials and slopes of increasing current which follow no universal orientation dependence for different annealing environments.

With such significant differences in the onset behavior, it is possible that new phases are formed at the surface of these samples during the high temperature annealing. To test this, the six samples described in Table 6.1 that were annealed at 1250 °C were characterized by x-ray diffraction (XRD) in the standard configuration to see if any unexpected phases had formed during the annealing process. XRD results revealed peaks corresponding to (100), (200), and (300) $SrTiO_3$ for the three (100) oriented samples and peaks corresponding to (111) and (222) $SrTiO_3$ for the three (111) oriented samples when tested for 2θ positions from 10-90°. This confirms the expected orientations and suggests that no additional phases were formed after annealing, or at least not in significant quantities to be detected by XRD. Thus, other factors are likely responsible for the observed I-V characteristics in Figure 6.14.

6.5 Discussion

To better understand the observed I-V characteristics for the unannealed, low temperature annealed, and high temperature annealed samples, the data from Figure 6.14 can be represented on a semi-log plot to observe the onset of current more clearly over several decades of current magnitudes. This will reveal whether the flat-band potentials are changing with annealing or if other factors are suppressing current to very small values at moderate anodic bias. A semi-log plot for all samples showing only the anodic (positive) current is shown in Figure 6.15.

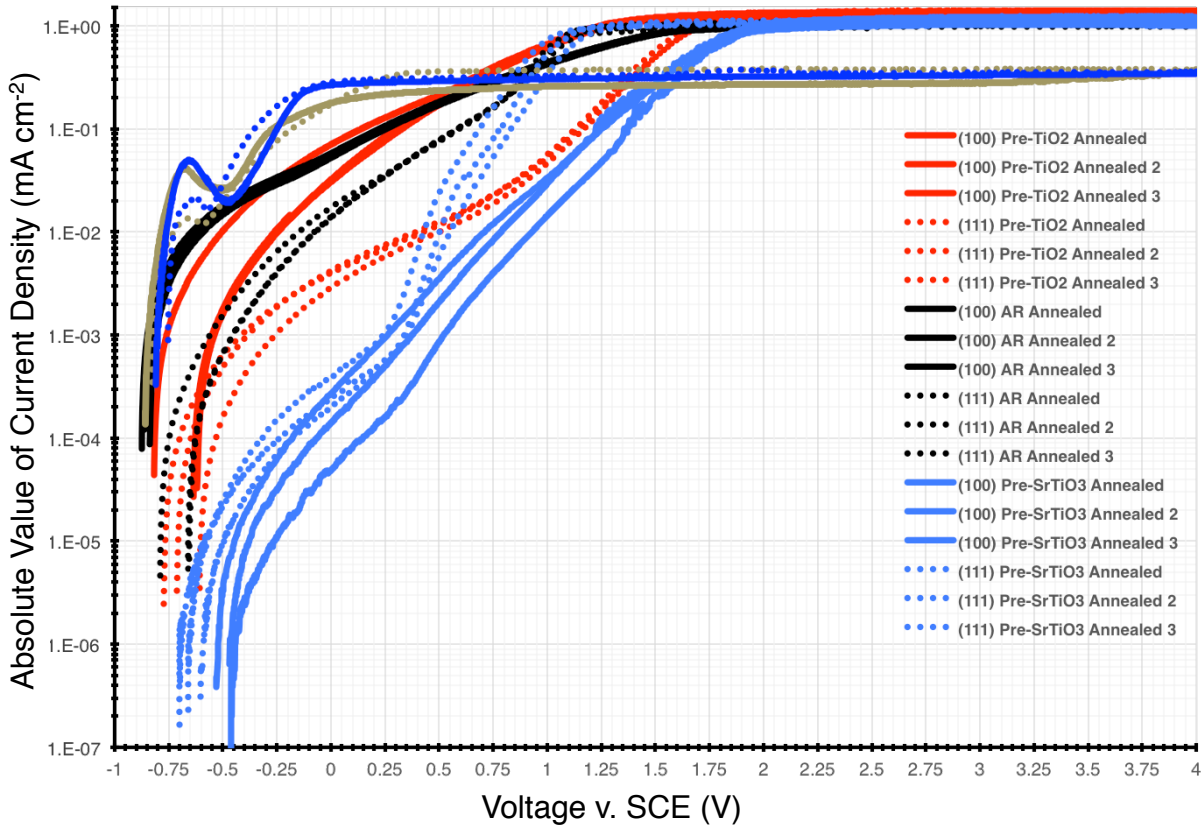

Figure 6.15: Semi-Log I-V Plots for All 0.7 wt% Nb-doped $SrTiO_3$ Samples

The flat-band potentials can be approximated as the cathodic potential at which the curve ends in Figure 6.15, since this is where the light current goes from anodic to cathodic. The more precise definition of the flat-band potential from I-V measurements is where the light current first positively exceeds the dark current, but given the variations in the current for the same sample as the voltage is swept around the flat-band potential, even this method does not produce the most precise values.

Thus, from simply looking at the light anodic current, the apparent flat-band potential shifts slightly to the right for the pre-$SrTiO_3$ annealed samples in particular, but does so by no more than 0.35 V total. However, the difference between the first point of saturation for (100) pre-$SrTiO_3$ 700 °C annealed and (100) pre-$SrTiO_3$ 1250 °C annealed samples is a much larger 2 V. Therefore, there are more significant factors contributing to the observed current other than a possibly varying flat-band potential.

Looking at Figure 6.15, both (111) and (100) pre-$SrTiO_3$ annealed samples have very muted anodic current until some mechanism changes the slope of the (111) onset around 0.3 V vs. SCE and it increases to saturation much more quickly than the (100) sample. For the pre-TiO_2 annealed samples, the (111) sample starts from cathodic biases with a steep onset similar to that of the (100) sample until it is limited by some factor before ultimately increasing in slope on the semi-log plot at 0.8 V vs. SCE to that of the (100) pre-$SrTiO_3$ sample. For the AR annealed samples, the flat-band potential of the (100) is nearly identical to the unannealed and low temperature annealed samples, and the current increases relatively quickly in line with the (100) pre-TiO_2 sample. The (111) AR annealed sample has a slow onset but quickly adopts a high slope on the semi-log plot and exceeds the current of the (100) AR annealed sample briefly at higher anodic bias.

The relative performance at open circuit under illumination for each sample can be predicted from Figure 6.15 by looking at the values of the current at -0.57 V vs. SCE. For nearly all samples the net reaction at the surface is oxidation, though the rate of oxidation is extremely low or even slightly reductive for the pre-$SrTiO_3$ annealed samples. A marker reaction investigation revealed that the majority of the (111) pre-$SrTiO_3$ annealed surface is comprised of terraces that are very active for the Ag reduction reaction. Since only a small portion of the surface favors oxidation, but the net reaction when averaged over the surface is approximately balanced (zero) for the pre-$SrTiO_3$ annealed samples, the results indicate that the oxidation reaction occurs at a faster rate than the reduction reaction where each is favored locally. The (111) pre-TiO_2 and (111) AR annealed samples have a few orders of magnitude higher performance at V_{oc}^* with the best performance being that exhibited by the (100) pre-TiO_2 and (100) AR annealed samples, which approach the performance of the unannealed and 700 °C annealed samples.

The performance at high anodic bias for each sample can also be evaluated. Calculations of the EQE can be approximated by assuming a monochromatic wavelength to represent the super-band-gap light incident on the sample. Using the equation for the EQE from Section 2.4, the percentage of incident photons with energies above the band gap of $SrTiO_3$ that are converted into reacted holes at the surface can be evaluated by extracting an average saturated anodic current density value from Figure 6.14 for the unannealed and 700 °C annealed samples, the pre-$SrTiO_3$ and AR annealed samples, and finally for the pre-TiO_2 samples. A sample calculation of the EQE for pre-TiO_2 annealed samples is shown below.

$$\frac{126\ \mathrm{W}}{\mathrm{m}^2} = \frac{126\ \mathrm{J}}{\mathrm{m}^2\mathrm{s}} \cdot \frac{\mathrm{eV}}{1.602 \cdot 10^{-19}} \cdot \frac{\mathrm{photon}}{3.82\ \mathrm{eV}} = 2.06 \cdot 10^{20}\ \frac{\mathrm{photons}}{\mathrm{m}^2\mathrm{s}}$$

$$1.35\ \frac{\mathrm{mA}}{\mathrm{cm}^2} = 1.35\ \frac{\mathrm{mC}}{\mathrm{cm}^2\mathrm{s}} \cdot \frac{\mathrm{C}}{1 \cdot 10^{3}\ \mathrm{mC}} \cdot \frac{1 \cdot 10^{4}\ \mathrm{cm}^2}{\mathrm{m}^2} \cdot \frac{\mathrm{e}^-}{1.602 \cdot 10^{-19}\ \mathrm{C}} = 8.43 \cdot 10^{19}\ \frac{\mathrm{e}^-}{\mathrm{m}^2\mathrm{s}}$$

$$\mathrm{EQE} = \frac{8.43 \cdot 10^{19}\ \frac{\mathrm{e}^-}{\mathrm{m}^2\mathrm{s}}}{2.06 \cdot 10^{20}\ \frac{\mathrm{photons}}{\mathrm{m}^2\mathrm{s}}} \cdot 100\% = 41\%$$

The EQE for pre-TiO_2 annealed samples with a saturated photocurrent density of roughly 1.35 mA/cm^2 is 41%. Accordingly, the maximum photocurrent density possible assuming only absorption of photons more energetic than 3.2 eV is approximately 3.3 mA/cm^2. Repeating the EQE calculation for an average saturated photocurrent density of 0.35 mA/cm^2 for unannealed and 700 °C annealed samples and 1.1 mA/cm^2 for pre-$SrTiO_3$ and AR annealed samples yields efficiency values of 11% and 33%, respectively. Therefore, simply annealing in pre-TiO_2 can increase the approximate efficiency at 4 V vs. SCE from 11% to 41%. However, when considering the photoconversion efficiency, the saturated photocurrent at such significant applied bias is irrelevant in practice because a smaller potential could be used to simply drive the electrolysis process from Figure 2.1. It is also important to note that, since many of these 1250 °C annealed samples are expected to exhibit spatially selective reactivity, any areas on the surface that are active for reduction during the physical photoelectrochemical experiment are actually acting to reduce the net current. At such significant anodic potentials of 4 V vs. SCE though, it's unlikely that any significant area fraction of the surface favors reduction. Understanding the increase in saturated photocurrent with annealing and the differences in onset with orientation and

annealing environment are both scientifically interesting and potentially useful for engineering an optimized material with increased saturated photocurrents closer to V_{oc}^{*}.

Figure 6.16 shows the samples annealed at 1250 °C on a semi-log plot with the absolute value of current plotted on the ordinate. Plotting the absolute value on the semi-log plot permits the visualization of the symmetry between the cathodic and anodic currents. There is a high degree of symmetry in the plots with the cathodic current exhibiting matching trends to the moderate anodic bias region with the exception of the (111) pre-$SrTiO_3$ annealed sample which seems, in the cathodic region, to increase with roughly the same slope as the curve does deep in the anodic region beyond 0.3 V vs. SCE.

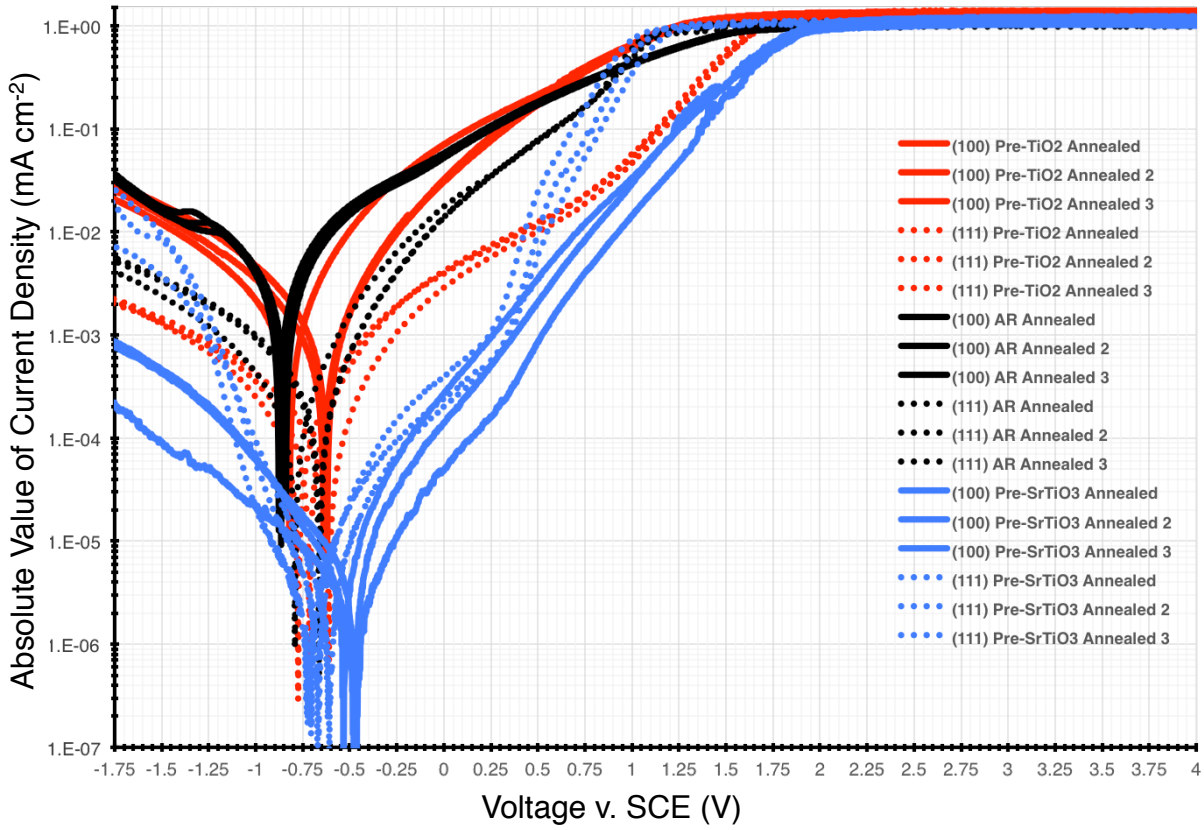

Figure 6.16: Semi-Log Absolute Value I-V Plots for 1250 °C Annealed 0.7 wt% Nb-doped $SrTiO_3$ Samples

One possible mechanism that could lead to suppressed onset for some of the samples is a high density of trapping sites that can act to trap charge carriers and limit current. One typical characteristic of materials exhibiting a high trap density is a hysteresis in the I-V characteristic due to the dependence of trapping behavior on the direction of the voltage scan. Figure 6.17 shows cyclic voltammetry (CV) plots that scan the pre-TiO_2 annealed samples from negative to positive and then back to negative voltages.

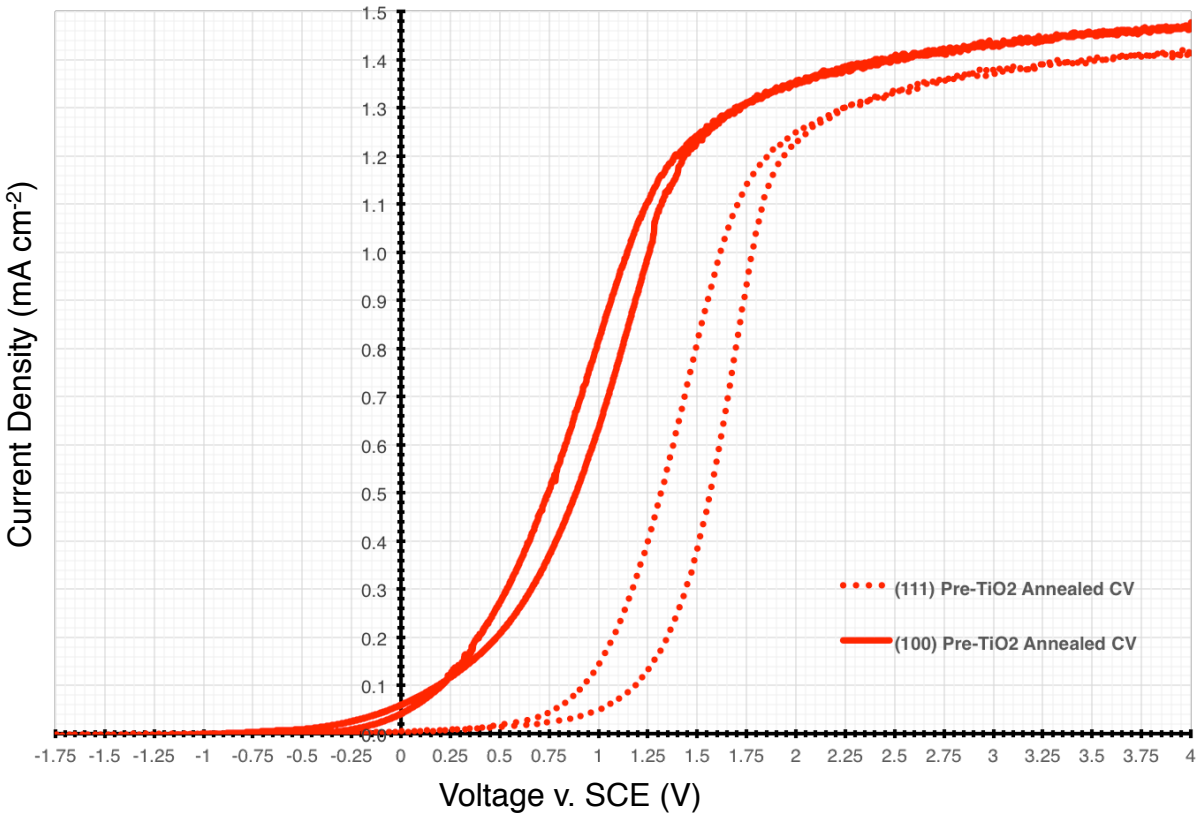

Figure 6.17: Measured Cyclic Voltammetry for Pre-TiO_2 Annealed 0.7 wt% Nb-doped $SrTiO_3$ Samples

Some hysteresis is certainly seen with slightly more for the (111) sample, but the hysteresis does not appear to be significant enough to be the driving factor leading to the suppressed anodic current between the two samples. Similar levels of hysteresis were seen for CV plots of the pre-$SrTiO_3$ samples.

There are many possible contributing factors to the observed current-voltage behaviors of the samples revealed by the physical photoelectrochemical tests. Whether it be due to differences in the electric field from the terminating layers, the differential reactivity of the terminating layers, variation of the flat-band potential, changes in the recombination lifetimes, migration of dopant atoms, or a combination of these and other factors, it is very difficult to analyze the underlying mechanisms driving the observations made from the physical photoelectrochemical results. However, the observation that annealing can give rise to increased saturated photocurrent magnitudes (with EQE increasing from 11% to 41%) and that the onset behavior varies dramatically for both the (100) and (111) oriented samples annealed at 1250 °C for different annealing environments makes understanding the source of these observations crucial to being able to optimize the material for photocatalytic and other applications. Simulations modeling the photoelectrochemical behavior of $SrTiO_3$ can be used to test the effect of many of these potential contributing factors and to compare the output with the physical observations to improve the understanding of the operation of the photocatalytic material. These simulations and their findings are described in Chapter 7.

6.6 Conclusions

Both (111) and (100) surfaces exhibited significant dependence in the I-V characteristic on the annealing environment. The degree of variation in the results with annealing environment seemed to be comparable, regardless of whether the terminations were polar or nonpolar. Therefore, the polarity of the idealized bulk termination layer is not thought to be the primary factor driving the selectivity of reaction products in these samples. Additionally, annealing itself was shown to have a significant effect on the I-V characteristic, producing an anodic shift in the photocurrent onset and an increased saturated photocurrent density magnitude.

7 COMPUTATIONAL PHOTOELECTROCHEMICAL STUDY OF TERMINATION-SPECIFIC REACTIVITY

7.1 Overview

The I-V characteristics of annealed (and unannealed) Nb-doped $SrTiO_3$ single crystals were measured in Chapter 6. In this chapter, finite element simulations in COMSOL Multiphysics®[130] were used to model the physical experiments. Direct comparisons were made to the physical results from Chapter 6 to estimate unkown key parameters in the model. The physical results do not support the hypothesis that the electric fields resulting from charged terminating layers drives the spatially selective reactivity on heavily doped $SrTiO_3$ surfaces. Additionally, it was observed physically that the I-V characteristic changed significantly after the annealing itself. Therefore, the objectives of the simulations in this chapter were to estimate unkown parameters, to test competing hypotheses for alternate sources of spatially selective reactivity (other than the charge of the terminating layers), and to identify parameters that could be contributing to the observed change in I-V characteristic after high-temperature annealing. The computational results sugggest that termination-dependent kinetic rates of the oxidation reaction may be responsible for the observed variation in the I-V characteristic with annealing environment. The simulations also demonstrate that near-surface non-uniformities in key parameters may result in the physically observed changes in the I-V characteristic after annealing.

7.2 Design

The fundamental equations and setup of the simulations were detailed in Section 3.2. Values for key material parameters of $SrTiO_3$ from the literature and from the source of the single crystals, MTI, are listed in Table 2.2. Figure 7.1 shows the geometry of 1D simulations relative to the physical samples and photoelectrochemical setup.

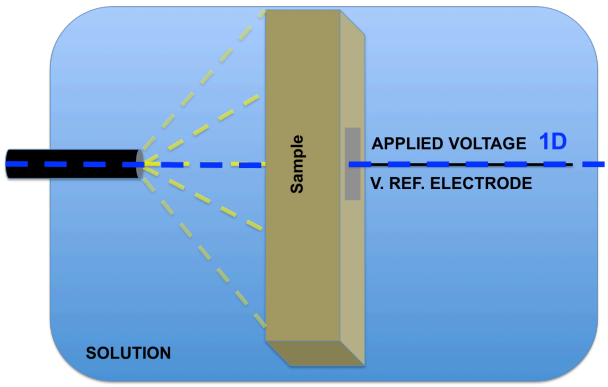

Figure 7.1: Geometry and Orientation of Simulations Relative to Physical Experiments

The 1D geometry was represented by a line through the depth of the material, perpendicular to the surface plane. It is shown going through the center of the surface which represents the approximation that no edge effects are considered. The left edge of the line is the surface with solution, with a Schottky contact representing the interface with the solution. The right edge of the line was modeled as an Ohmic contact to complete the circuit. Because, in the simulations, the current outputs can be measured directly at the surface (without measuring at a back contact like in the physical experiments), the entire thickness of the material need not be modeled.

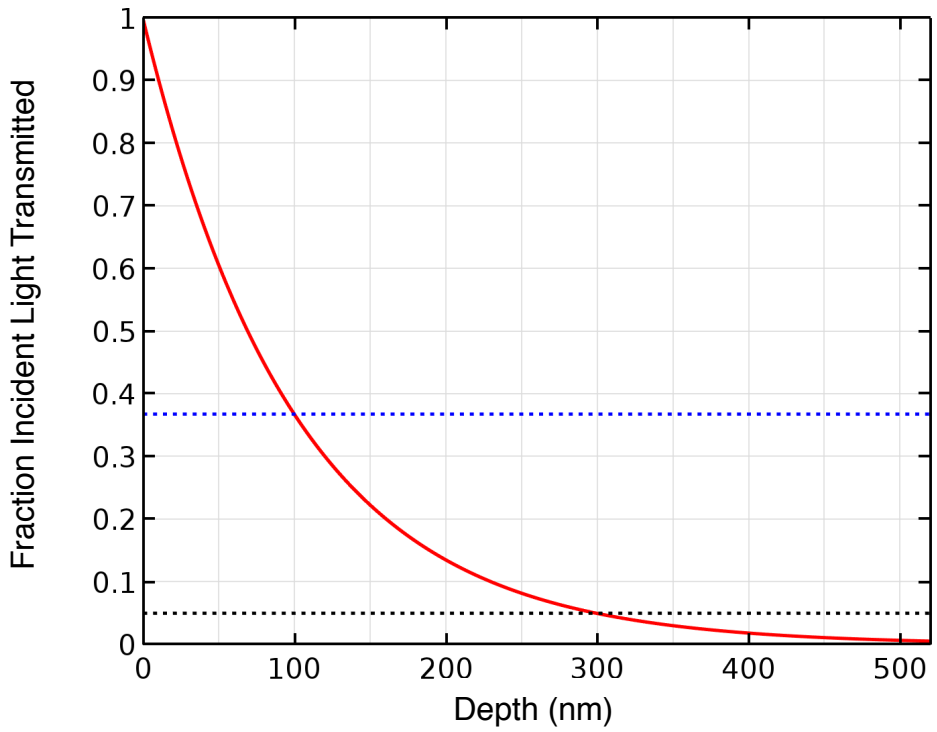

Figure 7.2: Simulated Absorption Depth for Xe Lamp Illumination in $SrTiO_3$
Blue Dotted Line: 63% Incident Light Absorbed (e^{-1} transmitted fraction)
Black Dotted Line: 95% of Incident Light Absorbed

To determine the required thickness of the material such that no performance is lost, the absorption depth of the material was investigated. Figure 7.2 shows the decay in the fraction of incident light that is transmitted through the thickness of simulated $SrTiO_3$. The dotted blue line represents a transmittance fraction of 1/e of the incident light, which is commonly defined as the absorption depth. This line intersects the curve at a material depth of 100 nm. The black dotted line represents the point where 95% of the light has been absorbed, and only nearly negligible photogeneration occurs beyond this depth. This occurs after 300 nm into $SrTiO_3$. Only one absorption coefficient of $1 \cdot 10^5$ cm^{-1} is used as an approximation to represent absorption over the whole spectrum of sufficiently energetic light. In order to ensure that there is more than enough room in the model geometry to

contain all relevant activity, the material in the simulated work was set to a thickness of 5,000 nm (or 5μm).

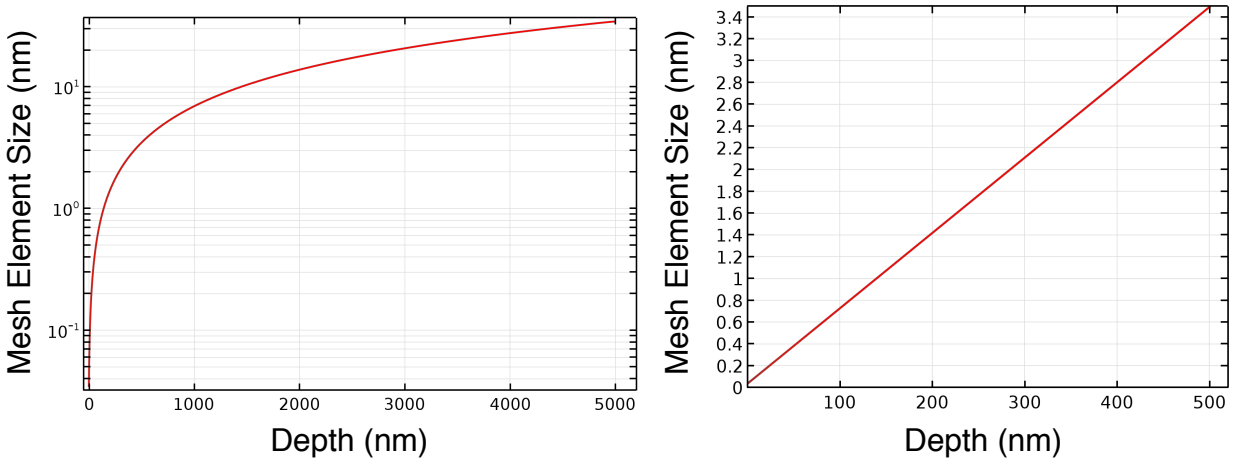

Figure 7.3: Mesh Size Variation with Depth for 1D Simulation

The finite element method used in these simulations requires dividing the 1D geometry into discrete segments constituting the overall mesh. Since the majority of holes are photogenerated near the surface, the mesh was defined to be finer (shorter discrete segments) near the surface and coarser towards the rear Ohmic contact. Figure 7.3 displays a semilog plot of the mesh element size variation with depth on the left and a linear plot of the element size near the surface on the right. In the region where the majority of light is absorbed near the surface, the element size is less than one nanometer. In total, there are 1,000 elements through the entire thickness of the device.

The total illumination irradiance input into the simulations was only that which is sufficiently energetic to be theoretically absorbed by $SrTiO_3$. Correspondingly, all

illumination in the simulations contributes to the photogeneration rate. Section 6.2 detailed the determination of an approximate experimental irradiance of sufficiently energetic light to be absorbed by $SrTiO_3$ of 126 W/m^2 with a representative photon energy of 3.82 eV. Similar analysis of the AM1.5G spectrum led to the calculation of an irradiance of sufficiently energetic light of 35 W/m^2, which can be approximately represented by the same photon energy. Unless otherwise noted, the illumination used was 126 W/m^2 to model the physical experimental results.

The simulations are ultimately solving for the steady-state current achieved given a constant illumination and photogeneration rate after having allowed sufficient time for all processes occurring in the material to reach constant rates. Time-dependent studies were used in this work to allow for the investigation of the evolution of effects over time, but the data presented here was after sufficient time for a virtual steady state to be reached, generally after a minimum of 0.1 ms. The fundamental equations from Section 3.2 were solved in the simulation using Newton's method and a built-in direct MUMPS solver.[130]

7.3 Results

Given the finding from the results in Chapter 6 that both (100) and (111) $SrTiO_3$ 1250 °C annealed surfaces exhibit strong dependence in the I-V characteristic on annealing environment, it seems unlikely that the primary source of the variation is related specifically to the charge of the terminating layer. Therefore, the simulations can be used to explore other causes of the observed I-V characteristics and to explore ways of improving the photocatalytic performance of the device.

Simulating a semiconductor with the same dopant density as the physical samples, exposed to the illumination irradiance from the physical experiments, and with the approximate assignment of $SrTiO_3$ material parameters according to the literature (noting that the effective Richardson constant is not known), the I-V characteristic produced is shown in Figure 7.4 below. An extremely high Richardson constant (A*) value was chosen for holes so as not to be limiting, in order to first investigate other limiting factors. A very low A* value for electrons was estimated as a starting point for comparison to the physical results (given the relatively low cathodic currents observed physically).

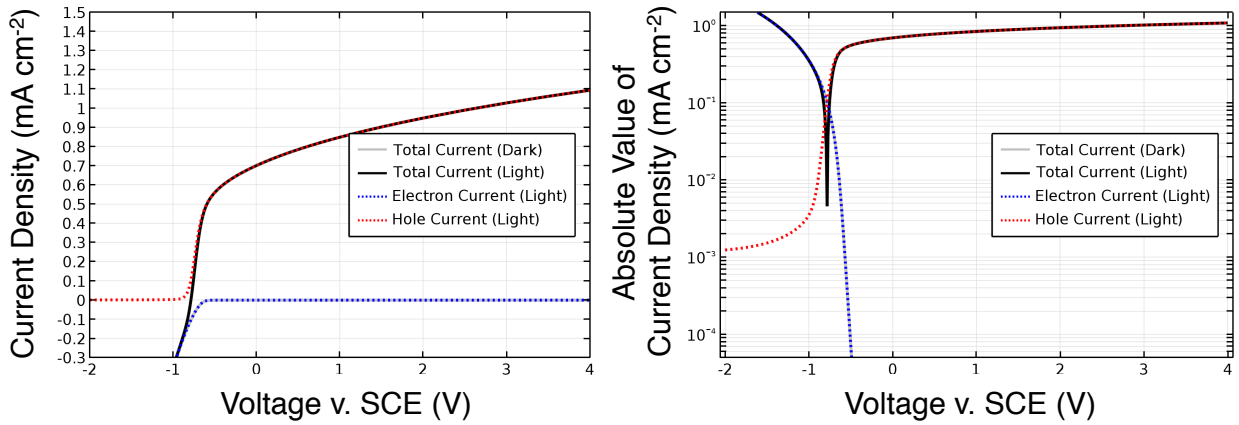

Figure 7.4: Linear and Semi-Log Simulated $SrTiO_3$ I-V Characteristic
$A^*_p = 1{\cdot}10^{13}\ A/(m^2K^2)$ | $A^*_n = 1{\cdot}10^{-6} A/(m^2K^2)$

The electron current is significant for more cathodic biases both in the light and in the dark while the hole current increases from zero around the flat-band potential in the light before reaching saturation. No hole current is observed in the dark with this being a heavily doped n-type material. Since this behavior of the dark current is prevalent throughout all simulations, the remaining results presented in this work are all under illumination unless noted otherwise.

The general shape of the I-V characteristic both in the light and in the dark resembles the expected theoretical n-type semiconductor I-V characteristic in Figure 3.1. It is also similar to the observed behavior of the unannealed and 700 °C annealed samples from Figure 6.10. There are noticeable differences, though, both in the sharpness of the onset in the simulated pattern and the higher saturated photocurrent magnitude in the simulation relative to that observed for the unannealed and 700 °C annealed samples. The lower saturated photocurrent could be the result of a variety of loss mechanisms in the catalyst. Notably, the simulated saturated photocurrent from Figure 7.4 is very comparable to that of the 1250 °C annealed samples in Figure 6.14.

A significant determinant of the saturated photocurrent magnitude is the recombination lifetime, as demonstrated in Chapter 4. The dependence of the current on the bulk recombination lifetime is shown in Figure 7.5. For very low lifetimes, there is virtually no anodic hole current because photogenerated carriers recombine before they can reach the surface. For lifetimes shorter than those shown here, the current approaches zero even at high anodic bias. As the lifetime is lengthened, the onset potential of anodic current becomes slightly more cathodic and the saturated photocurrent magnitude increases significantly as minority carriers beyond the space charge depth have increased diffusion lengths. At the longest lifetime tested of $1 \cdot 10^{-5}$ s, the saturated value is nearly equal to the theoretical maximum current density calculated for $SrTiO_3$ under the Xe lamp illumination of 3.3 mA/cm^2.

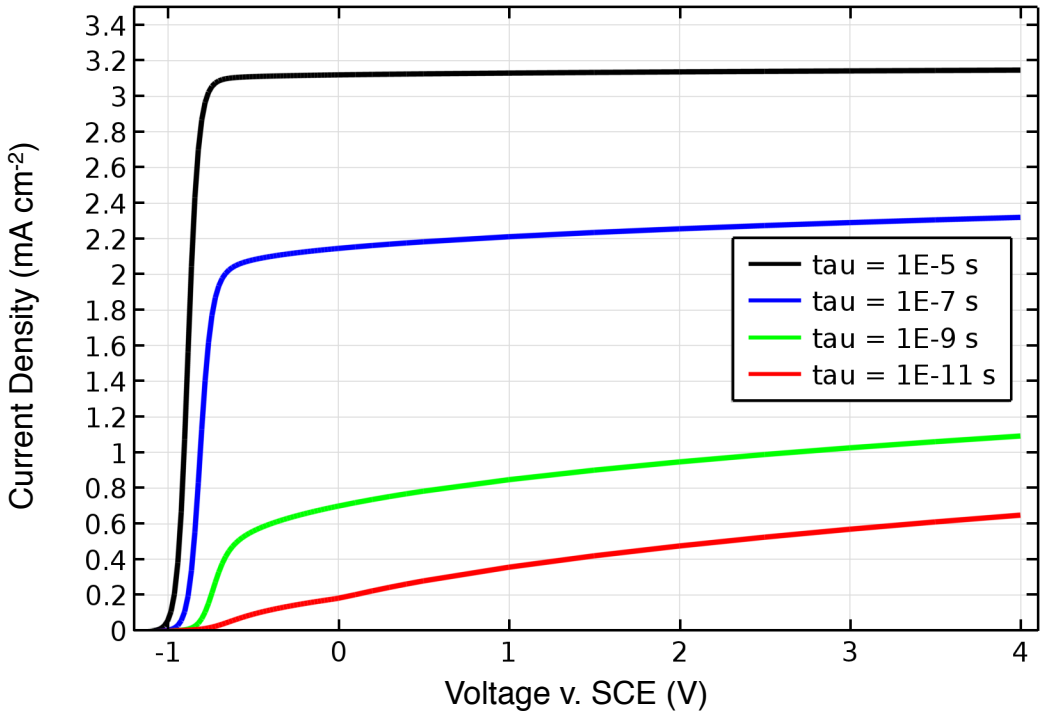

Figure 7.5: Variation in Simulated $SrTiO_3$ I-V Characteristics with Recombination Lifetime
$A^*_p = 1 \cdot 10^{13}\ A/(m^2K^2)$ | $A^*_n = 1 \cdot 10^{-6} A/(m^2K^2)$

Longer lifetimes beyond those shown here continue to approach this value with little change in the overall I-V characteristic, as the photogeneration rate becomes the limiting factor. Another observable trend is that, as the lifetime becomes longer, the current reaches more of a true saturation at more cathodic bias. In the case of the shorter lifetimes, the linear increase in current even at high anodic bias is indicative of increased space charge width (with increasing applied potential) continually capturing more and more of the carriers that recombined at more moderate anodic biases.

The lifetime that was taken from the literature for $SrTiO_3$ and input into the model is $1 \cdot 10^{-9}$ s, [90] which produces a saturated photocurrent magnitude in the simulation similar to the maximum current observed in the physical experiments. The unannealed and 700 °C annealed samples exhibit saturated photocurrents more reflective of a lifetime below $1 \cdot 10^{-}$

[11] s, but the lower saturated value could also be due to other factors. Therefore, the input lifetime of $1 \cdot 10^{-9}$ s is thought to be a reasonable value to use to represent the $SrTiO_3$ samples studied in this work. It is important to understand the source of the inherent losses resulting from this lifetime relative to the longer ones from Figure 7.5.

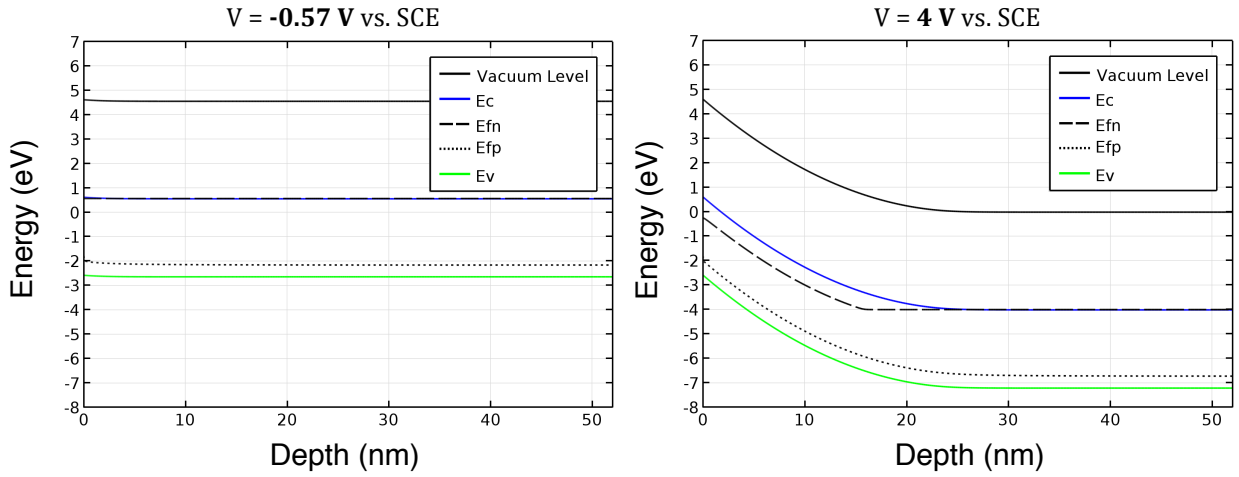

Figure 7.6: Simulated $SrTiO_3$ Energy Level Diagrams for Applied Anodic Biases

The large variance with lifetime is indicative of a space charge width that is more narrow than the absorption depth, leaving a high percentage of the carriers to only be captured by diffusing towards the surface with a recombination rate dictated by the lifetime. The depth at which 63% of the light has been absorbed was revealed to be 100 nm from Figure 7.2. Figure 7.6 shows the expansion of the space charge width with applied anodic bias beyond the illuminated open-circuit voltage (V_{oc}^*) by analyzing the energy level diagrams at -0.57 (V_{OC}^* as measured in Figure 6.7) and 4 V vs. SCE. Even at the highest anodic bias of 4 V vs. SCE, the space charge width is only less than one third of the absorption depth. Looking back at Figure 7.2, approximately 30% of the incident light has

been absorbed within the space charge width at a potential of 4 V vs. SCE. This is the reason why the saturated photocurrent from Figure 7.5 for a lifetime of $1 \cdot 10^{-9}$ s is only roughly one third of the maximum value. While the space charge width doesn't change for longer lifetimes, the minority carrier diffusion length increases greatly and the space charge width no longer limits the current as significantly.

Though the lifetime cannot be easily controlled to be made longer, a reduction in the dopant density would lengthen the space charge width and likely greatly improve performance for the same 1 ns lifetime. The selection of such a heavily doped material was based on the need for a high conductivity for the physical photoelectrochemical measurements. The simulations reveal, however, that in the design of a more optimal photocatalytic material, a lower density of dopants is beneficial. Figure 7.7 shows the dependence of the I-V characteristic on dopant density. Increasing the dopant density slightly from those used in this work results in a small drop in the saturated photocurrent magnitude and a slightly more cathodic onset, which are caused by a smaller space charge width and an increased electrical driving force at the surface at low bias, respectively. Decreasing the dopant density by an order of magnitude to $1 \cdot 10^{19}$ cm^{-3} results in a doubling of the saturated photocurrent magnitude. Decreasing another order of magnitude to $1 \cdot 10^{18}$ cm^{-3} results in a further increase in saturated photocurrent density approaching the maximum value for $SrTiO_3$ of 3.3 mA/cm^2 at high anodic bias. This is the same dopant density that was used computationally to achieve high photocatalytic efficiencies in coated $BaTiO_3$ in Chapters 4 & 5.

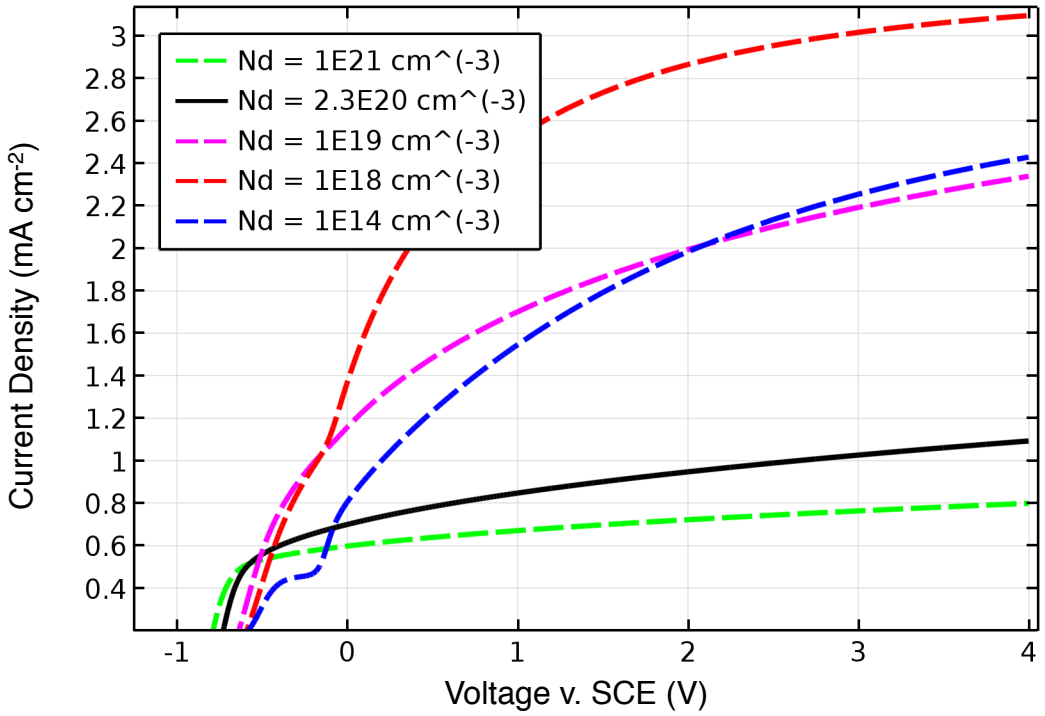

Figure 7.7: Variation in Simulated $SrTiO_3$ I-V Characteristics with Dopant Density
$A^*_p = 1{\cdot}10^{13}\ A/(m^2K^2)$ | $A^*_n = 1{\cdot}10^{-6} A/(m^2K^2)$

A corresponding shift in the onset to more anodic values is observed when the dopant density is decreased due to the decreased driving force at low anodic bias and the changing flat-band potential. Decreasing the dopant density another four orders of magnitude to $1{\cdot}10^{14}\ cm^{-3}$ results in a further shift of the onset in the anodic direction and a drop in the saturated photocurrent magnitude. This drop can be understood by analyzing the energy level diagrams, which reveal that, for $1{\cdot}10^{18}\ cm^{-3}$ doping, the space charge width exactly matches the depth at which 95% of the light is absorbed at high anodic bias. Widening the space charge width further by decreasing the dopant density doesn't capture any more charge carriers and only acts to reduce the electric field driving carriers to the surface, resulting in a slightly lower saturated photocurrent value as some of those distant

carriers recombine before drifting to the surface. To optimize the dopant density of $SrTiO_3$ for photocatalysis, the photoconversion efficiency would have to be evaluated, since increases in saturated current are met with more anodic onsets. However, for the purpose of this work, and for comparison to physical results, the dopant density used in all simulations will be that of the physical samples.

While the majority of simulation parameters used thus far seem to be appropriate in modeling the physical experiments, there is a major difference between the cathodic current in the simulated pattern in Figure 7.4 and the 1250 °C annealed samples, with the current being much higher in magnitude in the simulation. One key parameter that cannot be easily approximated from the literature, due to its specific definition in this work, is the Richardson constant (see Section 2.4), which represents the so-called reactivity parameter. Altering the Richardson constant (A*) value for electrons and holes can significantly change the I-V behavior. A low A* inhibits the transfer of charge carriers arriving at the surface to the external circuit by thermionic emission, which registers as current. A high A* prevents reaction at the surface from being the limiting factor and, if it's high enough, causes carriers to react virtually as soon as they arrive at the surface. In this regime, the current is a direct reflection of the rate of delivery of charge carriers to the surface.

Reducing the Richardson constant for electrons (A^*_n) appropriately can produce a simulated cathodic current that matches that seen in the physical experiment for the 1250 °C annealed samples. A simulated I-V curve with A^*_n reduced two orders of magnitude relative to Figure 7.4 is shown in Figure 7.8. The extremes of the cathodic and anodic currents in the semi-log representation are now very similar to that of the 1250 °C annealed samples from Figure 6.16. Some further reductions in A^*_n for specific samples

would lead to further agreement. The primary discrepancy still present between the simulated results and the physical photoelectrochemical results are the more anodic photocurrent onsets seen in Chapter 6.

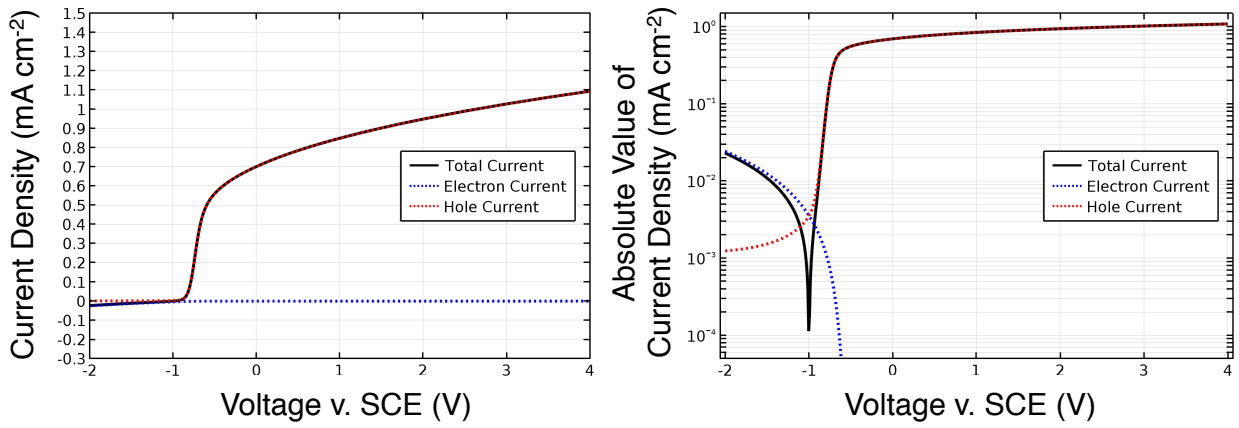

Figure 7.8: Linear and Semi-Log Simulated $SrTiO_3$ I-V Characteristic with Reduced A^*_n
$A^*_p = 1{\cdot}10^{13}\ A/(m^2K^2)$ | $A^*_n = 1{\cdot}10^{-8} A/(m^2K^2)$

The value of the Richardson constant for holes (A^*_p) used thus far was obtained from simulations sweeping different A^*_p values, which revealed that beyond $1{\cdot}10^{13}$ $A/(m^2K^2)$, there is negligible observable change in the I-V characteristics. High A^*_p values result in the most cathodic onset potentials and very sharp turn-on behavior in the vicinity of the flat-band potential. However, as A^*_p is decreased from this value, the onset becomes suppressed to more anodic values as shown in Figure 7.9.

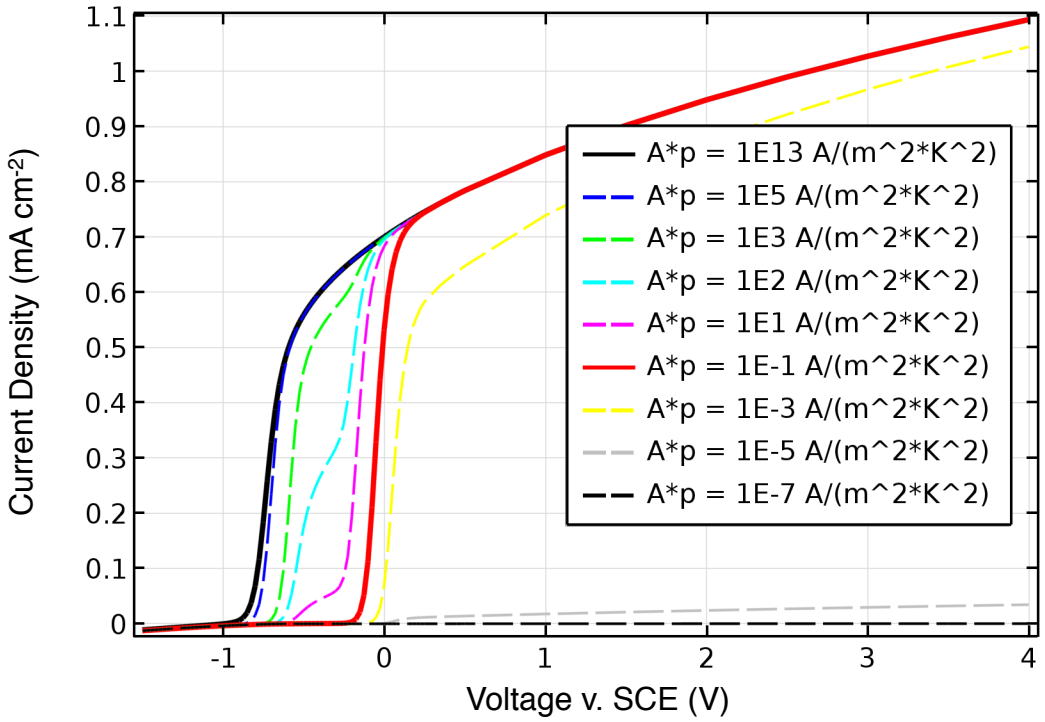

Figure 7.9: Variation in Simulated $SrTiO_3$ I-V Characteristics with Hole Reactivity Parameter (A^*_p)

This suppression of the anodic onset occurs because the recombination rate begins to dominate for lower A^*_p values. However, around 0 V vs. SCE, the current, even for lower A^*_p values, quickly rises to saturation. Analyzing the charge carrier concentrations through the material reveals that, around this potential (with slight variations for each A^*_p value), the majority carrier electrons no longer exist at the surface in greater concentration than the holes. The upward band bending at more anodic bias sweeps electrons away which sharply reduces the recombination rate, which is proportional to the product of the charge carrier concentrations. As A^*_p is decreased further to approximately $1 \cdot 10^{-3}$ A/(m^2K^2), the saturated photocurrent magnitude is no longer maintained and quickly begins to drop until falling completely to zero anodic current beyond $1 \cdot 10^{-7}$ A/(m^2K^2). This relatively quick drop-off in current occurs because, for such low values of the reactivity parameter, the

carriers do not react quickly upon arriving to the surface, and even the reduced recombination rate at anodic bias becomes the faster process, shunting the current. It is also important to note that, while a very high A^*_p value of $1 \cdot 10^{13}$ A/(m^{2}K^2) is used throughout this Chapter to represent the case where the reaction rate is not limiting, a more physically achievable value of $1 \cdot 10^{5}$ A/(m^{2}K^2) is shown in Figure 7.9 to have nearly the same I-V characteristic.

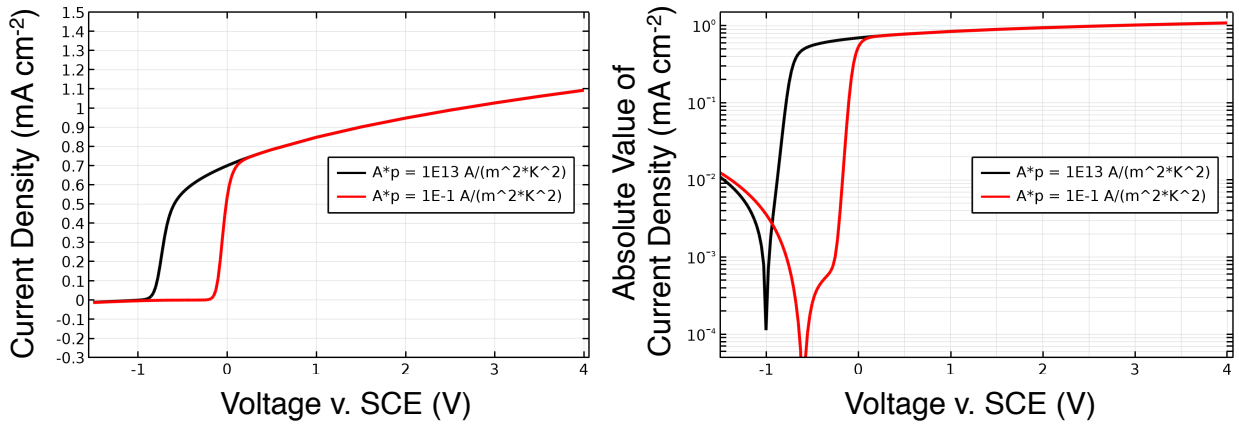

Figure 7.10: Linear and Semi-Log Simulated $SrTiO_3$ I-V Characteristics for A^*_p Values of Interest

Of the A^*_p values tested, the two which show the largest separation in onset while still reaching equivalent saturation currents are $1 \cdot 10^{13}$ A/(m^{2}K^2) and $1 \cdot 10^{-1}$ A/(m^{2}K^2). The linear and semi-log I-V characteristics for $SrTiO_3$ with these two relative extremes of the hole reactivity parameter are displayed in Figure 7.10. The suppressed onset for roughly 0.8 V with subsequent sharp rises to roughly equal saturated photocurrent magnitudes resembles some of the behavior of the physical photoelectrochemical data for the 1250 °C annealed samples. The kink in the current on the semi-log plot for the lower hole reactivity

parameter is a result of the reduced recombination rate due to electrons being swept away from the surface, which enables the reaction of holes at the surface to become the dominant process.

Shifts in the onset, while maintaining the saturated photocurrent magnitude, can also be achieved directly by varying the flat-band potential. By analyzing the equation for the flat-band potential in Section 2.4, shifts in E_{fb} can be achieved by changing the electron affinity, the Helmholtz potential, and the position of the Fermi level relative to the conduction band. Since a significant change in the electron affinity for different orientations and terminations is unlikely, and the known dopant level fixes the Fermi level position relative to the conduction band, only a difference in the Helmholtz potential can be reasonably manipulated. The source of variation in the Helmholtz potential is the difference between the local pH of the solution and the PZZP of the surface. The maximum difference attainable by varying the Helmholtz potential is approximately 1.65 V; this is the difference between a surface with local pH = 0 and PZZP = 14 and one with local pH = 14 and PZZP = 0. The Helmholtz potential is obtained by multiplying the difference between the two values by 0.059 V, following a Nernstian relationship.[138] This provides a large degree of variance in the onset potential, though it's unlikely that the local pH and PZZP vary to these extents at different areas of the same material surface in the same electrolyte. Some variation in the PZZP is very possible, though, given the different chemistry of different terminating layers. Figure 7.11 shows the I-V characteristic for $SrTiO_3$, with the expected pH and PZZP values compared with the two extremes of pH and PZZP values stated above to demonstrate the maximum shifting of the flat-band potential. Based on the

values of the flat-band potentials observed in the physical experiments, however, they don't vary from sample to sample by more than approximately 0.4 V.

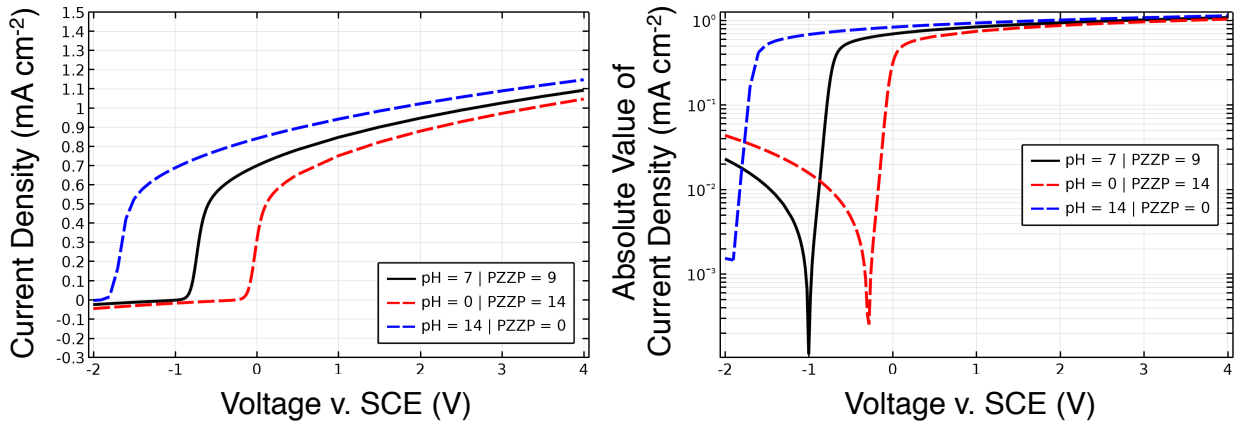

Figure 7.11: Linear and Semi-Log Simulated $SrTiO_3$ I-V Characteristics for Varying V_H & E_{fb}
$A^*_p = 1{\cdot}10^{13}\ A/(m^2K^2)$ | $A^*_n = 1{\cdot}10^{-8} A/(m^2K^2)$

While changes in the reactivity parameter and/or the flat-band potential may contribute to the observed variation in anodic onset among the 1250 °C annealed samples, it does not explain the significant increase in saturated photocurrent magnitude or onset shift for the 1250 °C annealed samples relative to the unannealed and 700 °C annealed samples from Figure 6.14. One parameter that has already been observed to produce dramatic shifts in the saturated photocurrent magnitude is the recombination lifetime. Thus, one proposed explanation for the variation in saturated photocurrent with high temperature annealing is that the polishing of the surface performed by MTI damages the crystal structure near the surface, increasing the density of trapping centers, and thereby decreasing the near-surface SRH recombination lifetime. Annealing for short time at relatively low temperature may not repair the structure, but annealing for 10 hours at 1250 °C could. Figure 7.12 shows the simulated results of implementing a shorter lifetime

of $1 \cdot 10^{-12}$ s for the first 100 nm and then abruptly restoring the bulk lifetime of $1 \cdot 10^{-9}$ s for the remainder of the thickness. This short recombination lifetime near the surface is an attempt to model the behavior of the unannealed and 700 °C annealed samples in the physical photoelectrochemical tests. For comparison, a simulated curve is shown where the lifetime is $1 \cdot 10^{-9}$ s throughout the thickness of the sample to model the increased saturated photocurrent characteristic of the 1250 °C annealed samples.

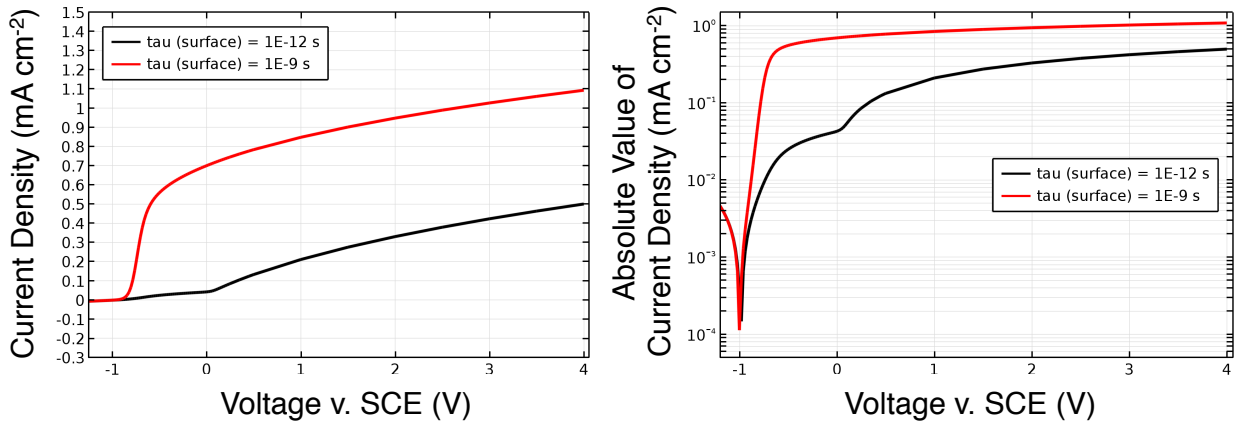

Figure 7.12: Linear and Semi-Log Simulated $SrTiO_3$ I-V Characteristics for Varying Near-Surface Lifetime

$A^*_p = 1 \cdot 10^{13}\ A/(m^2K^2)$ | $A^*_n = 1 \cdot 10^{-8} A/(m^2K^2)$

Comparing the output with the physical results in Figure 6.15, a change in the near-surface lifetime can account for the increase in saturated photocurrent magnitude, but not for the shift in apparent onset potential. The general shape of the onset for the simulated curve with reduced near-surface lifetime appears to be more drawn out than in the results of the physical experiment. The kink that can be observed in the simulated semi-log plot is a result of the abrupt change in the lifetime by three orders of magnitude at 100 nm. Carefully modeling a more smooth distribution of lifetimes near the surface may produce

an I-V characteristic that more closely resembles the unannealed and 700 °C annealed samples from Figure 6.15 for moderate anodic bias.

Another proposed explanation for the differences in saturated photocurrent magnitude for the 1250 °C annealed samples and the unannealed and 700 °C annealed samples is the possibility that, at high temperature and for long amounts of time, the Nb dopant atoms may migrate preferentially towards or away from the surface. This would alter the dopant concentration near the surface, which could vary the space charge width and change the flat-band potential. Figure 7.13 shows the simulated results from implementing a doping profile that sets the dopant density to decrease exponentially from a value of $1 \cdot 10^{22}$ cm^{-3} at the surface down to the bulk value of $2.3 \cdot 10^{20}$ cm^{-3} after 100 nm (solid black curve). This is compared to a uniform doping of $2.3 \cdot 10^{20}$ cm^{-3} throughout the thickness (red dashed curve).

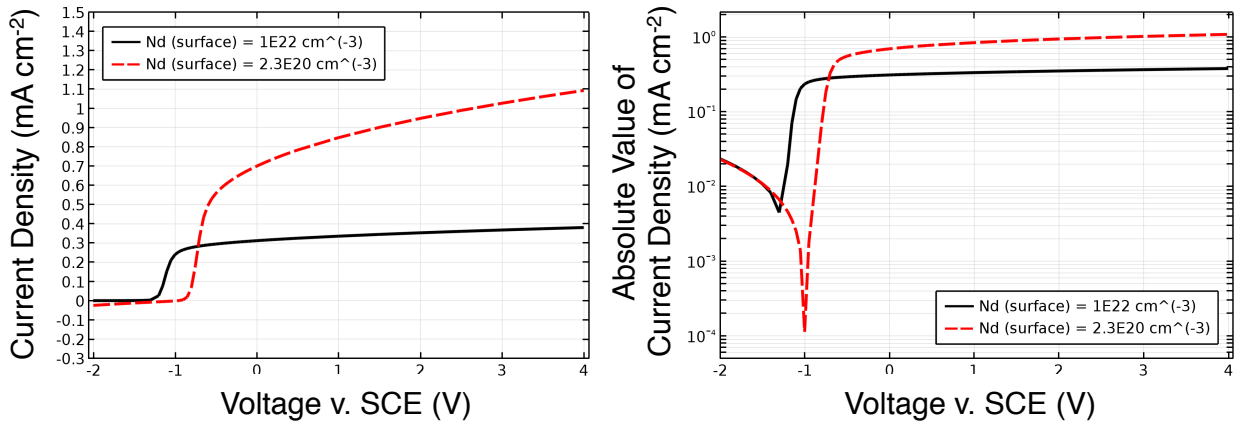

Figure 7.13: Linear and Semi-Log Simulated $SrTiO_3$ I-V Characteristics for Varying Near-Surface Doping

$A^*_p = 1 \cdot 10^{13}$ A/(m^{2}K^2) | $A^*_n = 1 \cdot 10^{-8}$A/(m^{2}K^2)

The selected distribution of dopants is founded on the possibility that the dopant distribution is non-uniform in the single crystals received from MTI, with a higher Nb concentration near the surface resulting from fabrication processes. Thus, the unannealed and 700 °C annealed samples are represented here as the solid black curve in Figure 7.13. The higher near-surface dopant density causes a cathodic shift in the flat-band potential, in accordance with the trends from Figure 7.7. The saturated photocurrent magnitude agrees well with those from the physical samples, displayed in Figure 6.10. After extended annealing at 1250 °C, it is possible that the Nb dopants would diffuse to a more uniform distribution represented by the dashed red curve in Figure 7.13. The uniform dopant density results in a significant increase in the saturated photocurrent magnitude and a small anodic shift in the onset potential, resembling the variation in the physical observations. The increase in the saturated value results from an increased space charge width, demonstrating a similar result to that seen in Figure 7.7. Migration of the Nb atoms could contribute to the discrepancies in the I-V characteristics of the 1250 °C annealed samples relative to the unannealed and 700 °C annealed samples.

7.4 Discussion

The two most impactful observations from the physical photoelectrochemical results in Chapter 6 were that annealing at 1250 °C resulted in both an anodic suppression of the photocurrent onset and a much higher saturated photocurrent magnitude, and that there was great variation in the onset behavior depending on annealing environment for 1250 °C annealed samples with both (100) and (111) orientations. The simulated results in Section 7.3 aimed to improve understanding of the material, approximate unknown parameters by

comparison with the physical results, and explore possible sources of the observed I-V characteristics.

Changes in the reactivity parameter for holes and variation of the flat-band potential were proposed as possible explanations of the variation in onset behavior observed for 1250 °C annealed samples. The original leading hypothesis was that the electric field created by the polarity of the termination layer was the driving force for reaction selectivity on the surface. Following from this hypothesis was the prediction that the net I-V characteristic of (111) surfaces would vary with annealing environment depending on the area fraction of terminations favoring reduction and oxidation, while the (100) surfaces would show no dependence on annealing environment since both possible terminations are nonpolar. However, significant dependencies on the annealing environment was seen for both the (100) and (111) samples. While different terminations on (100) don't have different polarity, they do have different chemistry, and it is very possible that they have very different reactivity rates for oxidation and reduction. If the annealing environments produce different area ratios of terminations on the surface, and the reactivity depends on the termination, then it should follow that the I-V characteristic could vary significantly for both (100) and (111) orientations. Figure 7.10 demonstrates how two different terminations with different hole reactivity parameters could reach the same saturation magnitude up to 0.8 V apart. Furthermore, the apparent flat-band potential, which can be seen on the semi-log plot, only shifts a portion of this distance, which is similar to the physical experimental results.

The other proposed explanation is a shifting of the flat-band potential, which could be achieved by variations in the difference between the local pH and the PZZP, which could

certainly vary significantly depending on the chemistry of the termination. However, looking at Figure 7.11 reveals that the shifts in the onset region are also directly correlated to a shift in the flat-band potential (not surprisingly), which is not reflective of the observations from the physical photoelectrochemical data.

Two possible explanations for the shift in onset to more anodic biases and increase in saturated photocurrent magnitude for the 1250 °C annealed samples relative to the unannealed and 700 °C annealed samples are non-uniform recombination lifetimes near the surface and non-uniform doping near the surface. A reduced lifetime for the first 100 nm near the surface can greatly reduce the saturated photocurrent magnitude. When combined with the effects of varying A^*_p, the drop in saturated photocurrent magnitude can be preserved and the onset can be shifted to resemble the physical results. Dopant migration away from the surface in the first 100 nm beyond the surface can lead to a small anodic onset shift (even without any change in A^*_p) and significant increases in the saturated photocurrent as shown in Figure 7.13. While both of these effects produce similar results to those seen physically, it is difficult to confidently determine whether one of these or a similar phenomenon is the most likely source of the change in the I-V characteristics. However, one constant between the two proposed mechanisms is the presence of near-surface non-uniformities. Given that XRD showed no additional phases, the most likely source of such drastic changes in the I-V curve for the same material after high temperature annealing is the introduction or existing presence of non-uniformity of a key parameter near the surface.

7.5 Joint Physical and Computational Results Discussion

Limited marker reaction results demonstrated spatially selective silver marker reaction products on the (111) pre-$SrTiO_3$ annealed Nb-doped $SrTiO_3$ surface. Past work focusing on photocatalytic surfaces exhibiting spatially selective reactivity characterized samples at open circuit under illumination, without any applied bias. The illuminated open-circuit potential (V_{oc}^*) for the unannealed (100) sample was measured to be -0.57 V vs. SCE in the electrolyte used for photoelectrochemical testing, and is approximated to be representative of V_{oc}^* for all samples. Figure 7.14 shows a semi-log representation of the I-V characteristics for all samples tested with the dashed yellow line representing the measured potential at open circuit under illumination. The intersection between the yellow line and the experimental curves represents the net current from the entire surface when no bias is applied. The performance at V_{oc}^* is therefore a strong descriptor of the expected behavior when characterized without any applied bias, such as during marker reactions.

It is shown in Figure 7.14 that nearly all samples exhibit net oxidative currents near V_{oc}^* when averaged over the whole surface, and that these currents are only a minute fraction of the saturated photocurrent magnitudes. This is true not only to the 1250 °C samples, but also to the unannealed and 700 °C annealed samples. A small bias, while energetically expensive, is generally worthwhile to maximize photoanodic performance in these samples and can lead to a current that is orders of magnitude higher.

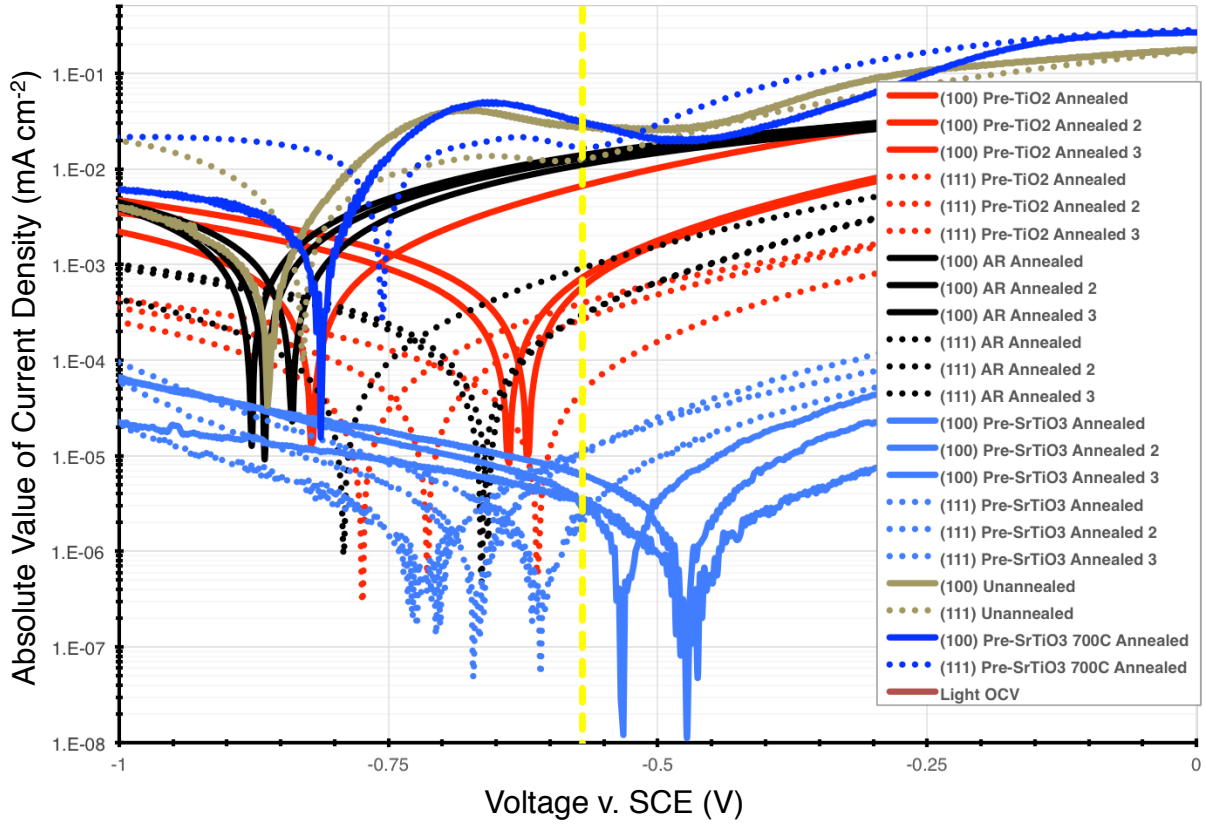

Figure 7.14: Current for All 0.7 wt% Nb-doped $SrTiO_3$ Samples at V_{oc}^* (Yellow Dotted Line)

Additionally, there are stark differences in the current magnitude at V_{oc}^* depending on the orientation and annealing conditions, with both orientations of pre-$SrTiO_3$ annealed samples having the smallest oxidation (or for some samples actually reduction) currents of the samples tested. Understanding possible sources of this variation, and in turn how to engineer materials to exhibit desired I-V behaviors, was a primary objective of the simulations presented in this work.

Figure 7.15a shows the simulated I-V characteristic for Nb-doped $SrTiO_3$, which is generally comparable to the physical photoelectrochemical results reproduced in Figure 7.15b for the unannealed and 700 °C annealed samples. One major difference between the

two results is the lower saturated photocurrent magnitude of the physical results, which could be due to a variety of loss mechanisms and was seen to increase to the simulated value after annealing at 1250 °C. The other major difference is the very sharp onset of anodic and cathodic current in the simulation at virtually the same potential, compared to the more extended onset for both current directions seen in the physical experiments. It is thought that this difference may be a result of the specific energy levels of redox species in solution and their overlap with energetic charge carriers in the semiconductor, which is a factor that is not considered in the simulations. A slower delivery rate, slower reaction rate of charge carriers, or a multitude of possible non-idealities could also widen the onset region in the simulations and may be present in the physical samples.

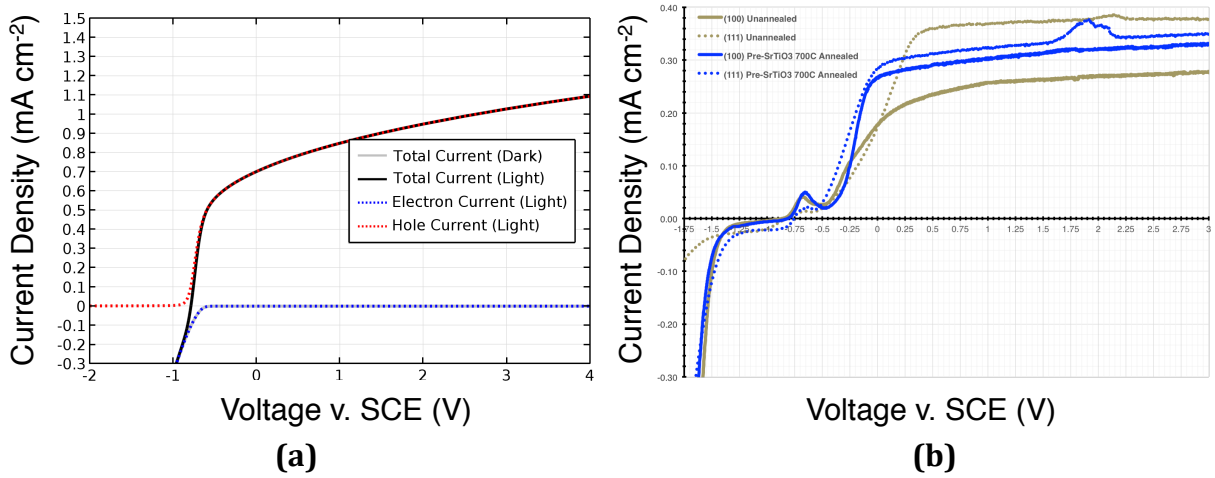

Figure 7.15: Physical and Computational I-V Characteristics for Nb-doped $SrTiO_3$
(a) Simulated (b) Physical Photoelectrochemical Results for Unannealed and 700 °C Annealed Samples

The simulations were used to test possible explanations for the widely varying anodic onset I-V behaviors among the 1250 °C annealed samples. Varying the reactivity parameter for holes was shown to produce significant shifts in the anodic onset region

while still maintaining equal saturated photocurrent magnitudes and only slightly shifting the apparent flat-band potential. A direct comparison between two extremes of the hole reactivity parameter and select physical photoelectrochemical data from two 1250 °C annealed samples is shown in Figure 7.16.

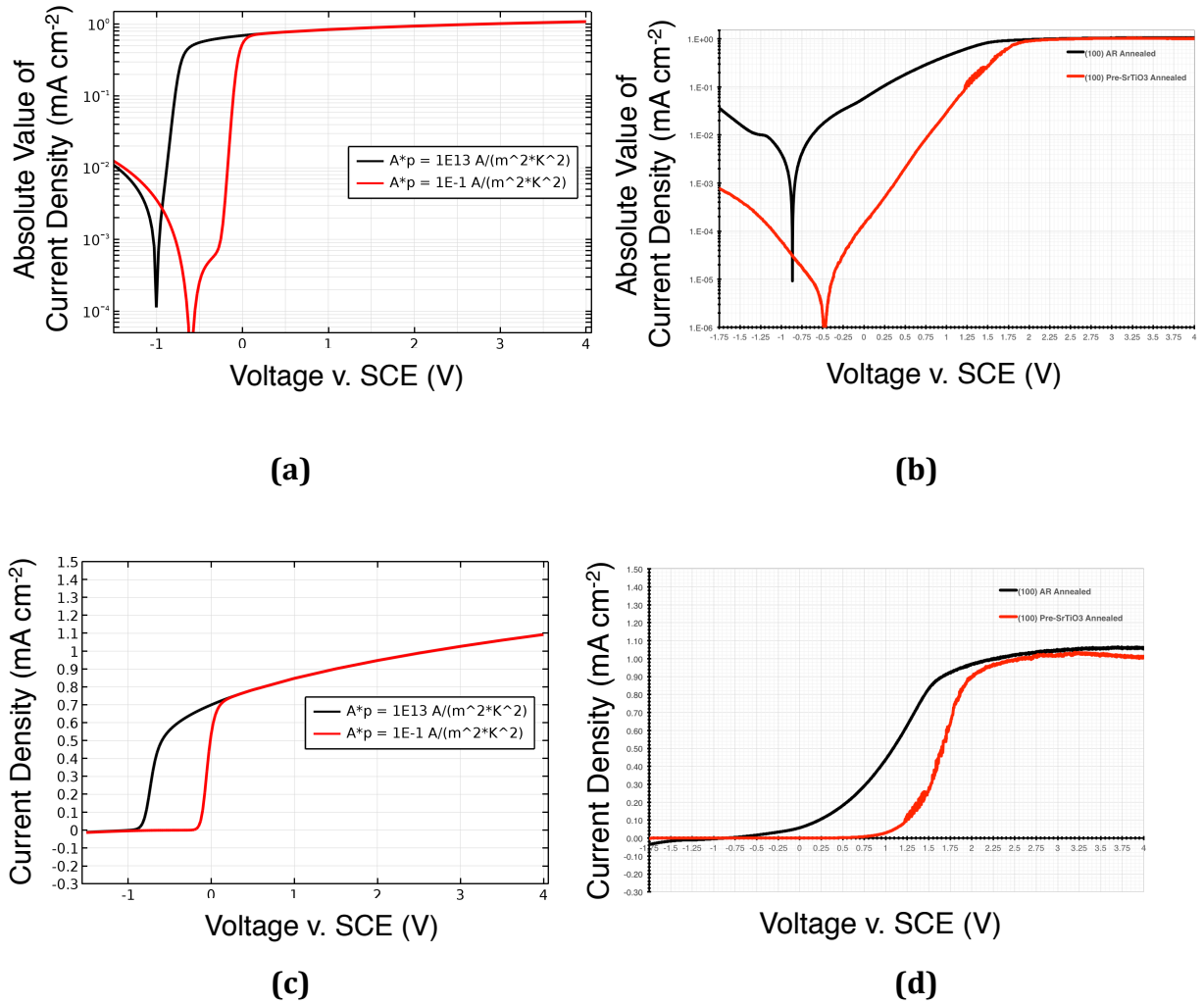

Figure 7.16: Physical and Computational Linear and Semi-Log I-V Characteristics for Nb-doped $SrTiO_3$. (a,c) Simulated (b,d) Physical Photoelectrochemical Results for Select 1250 °C Annealed Samples

The left two images represent simulated results while the right two images represent physical data. The same I-V data is represented in both cases on a semi-log plot

on top and a linear plot below. The two selected physical samples are (100) AR annealed and (100) pre-$SrTiO_3$ annealed, with the only difference between the samples being the pre-treatment of the crucible used for annealing. Looking at the semi-log plots, the simulated curves show a similar shift in flat-band potential and similar relative onsets compared to the physical data. In addition, for both sets of data, the two curves reach the same saturation value around 1.1 mA/cm^2. The primary difference between the simulated and physical data is precisely where the curves reach saturation on the potential axis. The onsets are much sharper and more vertical for both simulated samples compared to the physical data, which is a trend that is present throughout all of the simulations relative to the physical photoelectrochemical data.

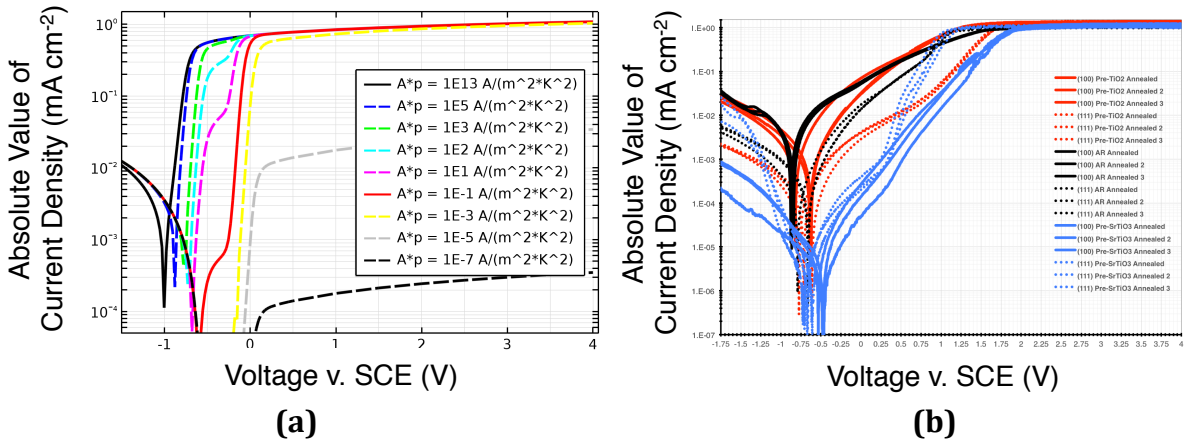

Figure 7.17: Physical and Computational Semi-Log I-V Characteristics for Nb-doped $SrTiO_3$ **(a)** Simulated **(b)** Physical Photoelectrochemical Results for 1250 °C Annealed Samples

This is also reflected in the linear representations of the data, where once again the relative behavior of the simulated curves matches the physical data well, but the anodic onset region is much more elongated in the physical data.

Simulated results for intermediate values of A^*_p are compared with the data for the entire set of 1250 °C annealed samples in Figure 7.17. In reality, it is possible that while individual terminations exhibit extreme differences in the reactivity for holes, the net current produced from photoelectrochemical experiments is an average over the whole surface, and will therefore exhibit a combination of the I-V characteristics of each individual termination. Figure 7.17 demonstrates how the behavior of an intermediate reactivity parameter for a single termination is similar to the I-V variations observed for the physical samples.

7.6 Conclusions

The physical photoelectrochemical results from Chapter 6 revealed significant dependencies in the I-V characteristic on the annealing environment for both (111) and (100) surfaces. Simulations demonstrated that surfaces with different reaction rates for holes could exhibit very similar I-V characteristics to those observed in the physical photoelectrochemical data. It is therefore proposed that different reactivities resulting from the chemistry of different terminations and their interactions with solution may be the primary driving force for spatial selectivity on the surfaces tested in this work. Simulated results suggest that non-uniformities of key parameters near the surface may be responsible for the observed shift in photocurrent onset and saturated photocurrent magnitude after annealing.

8 INTEGRATED DISCUSSION, CONCLUSIONS, AND FUTURE PROSPECTS

8.1 Integrated Discussion

A 1D photoelectrochemical computational model was developed in Chapter 4 to model domain-specific reactivity in $BaTiO_3$ coated with TiO_2. The carrier lifetime, kinetics, and potential were identified as key parameters that have a significant effect on the efficiency. The internal quantum efficiency (IQE) of the physical samples tested in the literature[21] was estimated to be below 1%, but could be increased to over 90% (independently for oxidation and reduction on single domains) through faster reduction kinetics, a longer carrier lifetime, and a small anodic potential shift. The model was expanded to 2D in Chapter 5 to incorporate the effects of adjacent domains and evaluate efficiencies integrated over a surface with an equal proportion of negative and positive domains. Surprisingly, it was demonstrated that the 1D limiting IQE for individual positive and negative domains was actually a good predictor of the 2D limiting IQE averaged across adjacent positive and negative domains. An IQE for the 2D model of up to 90% was achieved after optimizing parameters and controlling the domain width within a target range of 100 – 400 nm. In this way, the less computationally intensive 1D model can be used to estimate the 2D optimal performance.

The model produced comparable qualitative results to previously reported physical marker reactions,[21] and provided a pathway towards achieving greatly enhanced

efficiencies in this and other similar material systems. A photoelectrochemical model was developed (rather than a purely photochemical one) to allow for the potential to be adjusted in the same manner as common potentiostat-controlled physical photoelectrochemical testing of photocatalytic materials.[138] Therefore, a direct comparison of the results of the computational model to physical photoelectrochemical results was desired. However, there are two fundamental difficulties in making this direct comparison. The first is that, unlike in marker reaction characterization, the output for photoelectrochemical testing is a net current average across the whole surface for a set of voltages. This means that, unlike in the computations, the electron and hole currents cannot be resolved (only the net charge movement is captured) and the current produced by different areas of the surface (i.e. positive and negative domains) is combined to form an averaged output current. For coated ferroelectric $BaTiO_3$, prepared similarly to the reported marker reaction studies, there are a variety of different polarization orientations, domain wall angles, and domain widths present on a single surface that render a surface average direct quantitative comparison to the model very difficult. The second difficulty in a direct comparison is that physical photoelectrochemical testing requires a high dopant density to read the net current exchange at the surface through the back contact. A moderate donor concentration is assumed for $BaTiO_3$ in the simulations. However, increased dopant levels may influence the ferroelectric properties of the material and make the assignment of accurate parameter values into the model difficult.

For these reasons, another material, $SrTiO_3$, which has been shown to exhibit termination-specific reactivity on terraces produced after annealing,[16,32] was selected for a direct quantitative comparison of the model to physical photoelectrochemical results.

There are only two possible terminations of $SrTiO_3$ on the surface for a given orientation (compared to many possible normal components of the polarization vector in coated $BaTiO_3$), which simplified the comparison to the model. Additionally, literature results[32] revealed that the annealing environment can influence the proportion of the prevalence of one termination to the other on the surface, which should in turn change the current output from physical photoelectrochemical tests. Lastly, heavily Nb-doped $SrTiO_3$ is commercially available, with a number of materials parameters already established in the literature for the doped material (which were input into the simulations where available).

Reported marker reactions results on (not extrinsically doped) annealed $SrTiO_3$ showed that spatially selective reactivity was only observed for crystal orientations with polar (charged) terminations,[16] suggesting a similar effect of internal fields to that observed in ferroelectrics, which was supported by the simulations in Chapters 4 & 5. However, the physical results presented in Chapter 6 revealed I-V characteristics that were heavily dependent on the annealing environment for orientations with both polar and nonpolar terminations. The results also revealed an anodic shift in the photocurrent onset after annealing. Simulations in Chapter 7 were targeted at identifying another parameter, other than the charge of the terminations, that could result in the physically observed I-V characteristics for both orientations under different annealing conditions. The reactivity parameter for holes was demonstrated to produce similar variability in simulated I-V characteristics. It is possible that, while the charge of terminations dominates in the reported marker reactions on undoped $SrTiO_3$, when the dopants are introduced and the effects of internal fields are shielded over a shorter distance, other parameters have a more significant influence on surface currents. The simulations were also used to show that non-

uniformities in key parameters near the surface produce simulated shifts in the photocurrent onset consistent with the physically observed shifts after annealing. In $SrTiO_3$, annealing itself, which is required to some extent to form terraces of different terminations, has been shown to reduce the achievable photocatalytic efficiency. Further investigations into the detrimental effect of annealing observed here may be necessary to optimize the spatially selective photocatalyic performance of annealed $SrTiO_3$ surfaces.

8.2 Hypotheses Revisited and Conclusions

The research objectives and working hypotheses, outlined in Section 1.4, are revisited here along with corresponding conclusions produced by the results in Chapters 4-7.

1. *Construct a computational photoelectrochemical model of photocatalytic materials.*

Hypothesis: The physically observed spatially selective reactivity can be modeled using a simple semiconductor model (Chapter 4).

Conclusion: Assumptions of classical semiconductor device behavior and a Schottky contact at the surface were sufficient to produce computational data that generally supports reported physical results.

2. *Quantify the photocatalytic performance using a 1D model.*

Hypothesis: Oxidation and reduction reactions proceed at different rates at the illuminated open-circuit potential, limiting the overall efficiency (Chapter 4).

Conclusion: The estimated internal quantum efficiencies (IQE) of $TiO_2/BaTiO_3$ heterostructures from the literature are below 1%, with oxidation limiting the overall reaction rate.

3. *Identify and optimize the key material parameters that influence the performance.*

Hypothesis: The performance can be optimized primarily by altering the potential (Chapter 4).

Conclusion: The potential, the minority carrier lifetime, and the kinetic rate of reduction are most significant. Achieving a high minority carrier lifetime, promoting fast reduction kinetics, and shifting the potential slightly in the anodic direction permit an enhanced IQE near 90%.

4. *Expand to a 2D model, re-evaluate performance, and optimize design parameters.*

Hypothesis: The mutidomain performance is less than the single domain performance but greater than half of the single domain performance (Chapter 5).

Conclusion: The IQE for a surface with alternating negatively and positively polarized domains is not limited by a Z-scheme mechanism and is as high as 90% (nearly matching the 1D predicted performance) when the voltage and domain width are optimized.

5. *Conduct physical photoelectrochemical tests.*

Hypothesis: The annealing environment dictates the area fractions of different terminations on the (111) surface, which in turn affects the reactivity accordingly. Reactivity of the (100) surface has no dependence on the annealing environment (Chapter 6).

Conclusion: The I-V characteristic of (111) and (100) surfaces both vary with annealing environment. The net reaction across the surface (in almost all samples) is oxidation at the illuminated open-circuit voltage. After annealing, single crystal Nb-

doped $SrTiO_3$ samples produced a suppressed onset of anodic current to more positive voltages.

6. Use the computational model to enhance understanding of the physical results

Hypothesis: The electric field resulting from the polarity of the termination layer is the primary factor responsible for the selectivity of reaction products to specific terraces previously observed on the (111) $SrTiO_3$ surface (Chapter 7).

Conclusion: The variability in the I-V characteristics observed physically for different annealing environments is consistent with computationally varying the kinetic rate for the oxidation reaction.

8.3 Future Prospects

The most impactful method developed in this work for future studies of photocatalytic materials is the use of a computational model to isolate key parameters and develop a set of optimal parameters that produce significantly increased efficiencies. When studying photocatalytic materials exhibiting spatially selective reactivity, physical photoelectrochemical methods have been shown to be difficult to interpret (and may require such high doping levels that the achievable efficiency is reduced dramatically). While physical photoelectrochemistry has been used in this work to aid in the verification of the computational model, marker reactions provide invaluable qualitative information about the spatially selective nature of the reactivity, which, when combined with quantitative computational results, can lead to enhanced understanding of the performance. To be able to continually compare the model to physical results without the

limitations of physical photoelectrochemistry, marker reactions can be performed with the sample under an applied bias. A related approach, which may be technically challenging, would be to use a focused ion beam (FIB) to selectively deposit contacts to individual terraces on the surface to make local electrochemical measurements, thereby avoiding the difficulties in interpreting data (like that from physical photoelectrochemistry) that represents a surface average.

In this work, the focus has been on achieving high quantum efficiencies assuming that the incident photons are sufficiently energetic to be absorbed. However, there are additional factors that contribute to the overall solar to hydrogen (STH) efficiency, including maximizing solar absorption and limiting back-reactions. As materials with more narrow band gaps than $BaTiO_3$ and $SrTiO_3$ (that have a demonstrated capability of spatially separating oxidation and reduction half reactions, such as $BiFeO_3$[23]) are studied further and their material parameters are more confidently determined, the computational model developed in this work can be used to design photocatalysts with truly competitive STH efficiencies. The model can also be extended to include specific solution effects, including detailed reaction kinetics, back-reactions, and any losses from separating the hydrogen and oxygen products. Ultimately, after the development of a sufficiently efficient material system, this type of finite-element model can be extended further to simulate and optimize the 3D performance of more complex particulate photocatalyst and reactor geometries.

REFERENCES

1 Report, U.S. Energy Information Administration: “International Energy Outlook”, 2013.
2 Daniel Yergin: The Prize: The Epic Quest for Oil, Money & Power, FREE PRESS, New York, NY, 2008.
3 A. G. Chmielewski: Environmental effects of fossil fuel combustion, EOLSS Publishers, Oxford, UK, 2002.
4 Report, Interagency Working Group on Hydrogen and Fuel Cells: “Hydrogen & Fuel Cells: Interagency Action Plan”, 2011.
5 Report, T. Lipman, Office of Energy Efficiency and Renewable Energy: “An Overview of Hydrogen Production and Storage Systems with Renewable Hydrogen Case Studies”, 2011.
6 Report, U.S. Energy Information Administration: “Annual Energy Review: Primary Energy Consumption by Source and Sector”, 2012.
7 F. E. Osterloh: Chem. Mater., 2008, vol. 20, pp. 35-54.
8 A. Fujishima and K. Honda: Nature, 1972, vol. 238, pp. 37-38.
9 M. Ni, M. Leung, D. Leung, and K. Sumathy: Renew. Sust. Energ., Rev., 2005, vol. 11, pp. 401-425.
10 C. Xiaobo, S. Shaohua, G. Liejin, and S. S. Mao: Chem. Rev., 2010, vol. 110, pp. 6503-6570.
11 J. M. Bolts and M.S. Wrighton: J. Phys. Chem., 1976, vol. 80, pp. 2641-2645.
12 M. Tomkiewicz and H. Fay: Appl. Phys., 1979, vol. 18, pp. 1-28.
13 M. S. Wrighton, D. S. Ginley, P. T. Wolczanski, A.B. Ellis, D.L. Morse, and A. Linz: PNAS, 1975, vol. 72, pp. 1518-1522.
14 J. L. Giocondi and G. S. Rohrer: Chem. Mater., 2001, vol. 13, pp. 241-242.
15 J. L. Giocondi and G. S. Rohrer: J. Phys. Chem. B, 2001, vol. 105, pp. 8275-8277.
16 J. L. Giocondi and G. S. Rohrer: J. Am. Ceram. Soc., 2003, vol. 86, pp. 1182-1189.
17 N. V. Burbure, P. A. Salvador, and G. S. Rohrer: J. Am. Ceram. Soc., 2006, vol. 89, pp.2943-2945.
18 N. V. Burbure, P. A. Salvador, and G. S. Rohrer: J. Am. Ceram. Soc., 2010, vol. 93, pp. 2530-2533.
19 A. Bhardwaj, N. V. Burbure, A. Gamalski, and G. S. Rohrer: Chem. Mater., 2010, vol. 22, pp. 3527-3534.
20 A. Bhardwaj, N. V. Burbure, G. S. Rohrer: J. Am. Ceram. Soc., 2010, vol. 93, pp. 4129-4134.
21 N. V. Burbure, P. A. Salvador, and G. S. Rohrer: Chem. Mater., 2010, vol. 22, pp. 5823-5830.
22 N. V. Burbure, P. A. Salvador, and G. S. Rohrer: Chem. Mater., 2010, vol. 22, pp. 5831-5837.
23 Y. Zhang, A. M. Schultz, P. A. Salvador, and G. S. Rohrer: J. Mater. Chem., 2011, vol. 21, pp. 4168-4174.
24 A. M. Schultz, Y. Zhang, P. A. Salvador, and G. S. Rohrer: ACS Appl. Mater. Interfaces, 2011, vol. 3, pp. 1562-1567.

25 A. M. Schultz, P. A. Salvador, and G. S. Rohrer: Chem. Commun., 2012, vol. 48, pp. 2012-2014.
26 L. Li, G. S. Rohrer, and P. A. Salvador: J. Am. Ceram. Soc., 2012, vol. 95, pp. 1414-1420.
27 L. Li, X. Liu, Y. Zhang, P. A. Salvador, and G. S. Rohrer: Int. J. Hydrogen Energy, 2013, vol. 38, pp. 6948-6959.
28 L. Li, P. A. Salvador, and G. S. Rohrer: Nanoscale, 2014, vol. 6, pp. 24-42.
29 R. Munprom, P. A. Salvador, and G. S. Rohrer: Chem. Mater., 2014, vol. 26, pp. 2774-2776.
30 R. Munprom, P. A. Salvador, and G. S. Rohrer: J. Mater. Chem. A, 2016, vol. 4, pp. 2951-2959.
31 G. Koster, B. L. Kropman, G. J. H. M. Rijnders, D. H. A. Blank, and H. Rogalla: Appl. Phys. Lett., 1998, vol. 73, pp. 2920-2922.
32 Y. Zhu, P. A. Salvador, and G. S. Rohrer: Chem. Mater., 2016, vol. 28, pp. 5155-5162.
33 P. H. Maruska and A. K. Ghosh: Solar Energy, 1978, vol. 20, pp. 443-458.
34 G. J. Schulz: J. Chem. Phys., 1960, vol. 33, p. 1661.
35 H. Larzul, F. Gelebartand, and A. Johannin-Gilles: Compt. Rend., 1965, vol. 261, p. 4701.
36 R. N. Compton, R. H. Heubner, P. W. Reinhardt, and L. G. Christophorou: J. Chem. Phys., 1968, vol. 48, p. 901.
37 A. Skerbele, M. A. Dillon, and E. N. Lassettre: J. Chem. Phys., 1968, vol. 49, p. 5042.
38 L. M. Hunter, D. Lewis, and W. H. Hammill: J. Chem. Phys., 1970, vol. 52, p. 1733.
39 S. Trajmar, W. Williams, and A. Kupperman: J. Chem. Phys., 1971, vol. 54, p. 2274.
40 N. Y. Kiang: Scientific American, 2008, vol. 298, pp. 48-55.
41 T. Wantabe, A. Fujishima, and K.-I. Honda: Bull. Chem. Soc. Jpn., 1976, vol. 49, pp. 355-358.
42 J. G. Mavroides, J. A. Kafalas, and D. F. Kolesar: Appl. Phys. Lett., 1976, vol. 28, pp. 241-243.
43 M. S. Wrighton, A. B. Ellis, P. T. Wolczanski, D. L. Morse, H. B. Abrahamson, and D. S. Ginley: J. Am. Chem. Soc., 1976, vol. 98, pp. 2774-2779.
44 S. Sato and J. M. White: Chem. Phys. Lett., 1980, vol. 72, pp. 83-86.
45 K. Maeda and K. Domen: J. Phys. Chem. C, 2007, vol. 111, pp. 7851-7861.
46 A. B. Murphy, P. R. F. Barnes, L. K. Randeniya, I. C. Plumb, I. E. Grey, M. D. Horne, and J. A. Glasscock: Int. J. Hydrogen Energy, 2006, vol. 31, p. 1999.
47 J. R. Bolton, S. J. Strickler, and J. S. Connolly: Nature, 1985, vol. 316, pp. 495-500.
48 A. J.Bard and M. A. Fox, Acc. Chem. Res., 1995, vol. 28, pp. 141-145.
49 J. A. V. Butler: Trans. Faraday Soc., 1924, vol. 9, pp. 729-733.
50 T. Erdey-Grúz and M. Volmer: Z. Physik. Chem., 1930, vol. 150, pp. 203-213.
51 M. A. Butler and D. S. Ginley: J. Electrochem. Soc., 1978, vol. 125, pp.228-232.
52 W. W. Gärtner: Phys. Rev., 1959, vol. 116, pp. 84-87.
53 O. K. Varghese and C. A. Grimes: Sol. Energy Mater. Sol. Cells, 2008, vol. 92, pp. 374-384.
54 J. Shi and L. Guo: Prog. Nat. Sci., 2012, vol. 22, pp. 592-615.
55 L. Li, X. Liu, Y. Zhang, N. T. Nuhfer, K. Barmak, P. A. Salvador, and G. S. Rohrer: ACS Appl. Mater. Interfaces, 2013, vol. 5, pp. 5064-5071.

56 D. F. Wang, J. H. Ye, T. Kako, and T. Kimura: J. Phys. Chem. B, 2006, vol. 110, pp. 15824-15830.
57 H. Kato and A. Kudo: J. Phys. Chem. B, 2002, vol. 106, pp. 5029-5034.
58 R. Konta, T. Ishii, H. Kato, and A. Kudo: J. Phys. Chem B, 2004, vol. 108, pp. 8992-8995.
59 T. Ishii, H. Kato, and A. Kudo: J. Photochem. Photobiol. A, 2004, vol. 163, pp. 181-186.
60 R. Niishiro, H. Kato, and A. Kudo: PCCP, 2005, vol. 7, pp. 2241-2245.
61 S. W. Bae, P. H. Borse, and J. S. Lee: Appl. Phys. Lett., 2008, vol. 92, pp. 104-107.
62 H. Yu, S.X. Ouyang, S. C. Yan, Z. S. Li, T. Yu, and Z. G. Zou: J. Mater. Chem., 2011, vol. 21, pp. 11347-11351.
63 K. Domen, A. Kudo, and T. Onishi: J. Catal., 1986, vol. 102, pp. 92-98.
64 K. Domen, A. Kudo, T. Onishi, N. Kosugi, and H. Kuroda: J. Phys. Chem., 1986, vol. 90, pp. 292-295.
65 S. Ikeda, K. Hirao, S. Ishino, M. Matsumura, and B. Ohtani: Catal. Today, 2006, vol. 117, pp. 343-349.
66 K. Domen, S. Naito, M. Soma, T. Onishi, and K. Tamaru: J. Chem. Soc., Chem. Commun., 1980, pp. 543-544.
67 K. Domen, S. Naito, T. Onishi, and K. Tamaru: J. Phys. Chem., 1982, vol. 86, pp. 3657-3661.
68 J. H. Luo and P. A. Maggard: Adv. Mater., 2006, vol. 18, pp. 514-517.
69 S. Boumaza, A. Boudjemaa, A. Bouguelia, R. Bourab, and M. Trari: Appl. Energy, 2010, vol. 87, pp. 2230-2236.
70 K. Rajeshawar, P. Singh, and J. Dubow: Electrochim. Acta, 1978, vol. 23, pp. 1117-1144.
71 R. D. Nasby and R. K. Quinn: Mat. Res. Bull., 1976, vol. 11, pp. 985-992.
72 H. Fan, H. Li, B. Liu, Y. Lu, T. Xie, and D. Wang: Appl. Mater. Interfaces, 2012, vol. 4, pp. 4853-4857.
73 K. Maeda: Appl. Mater. Interfaces, 2014, vol. 6, pp. 2167-2173.
74 X. X. Xu, G. Liu, C. Randorn, and J. T. S. Irvine: Int. J. Hydrogen Energy, 2011, vol. 36, pp. 13501-13507.
75 J.-M. Lehn,J.-P. Sauvage, and R. Ziessel: Nouv. J. Chim., 1980, vol. 4, p. 623.
76 K. Yamaguti and S. Sato: J. Chem. Soc., Faraday Trans. 1, 1985, vol. 81, p. 1237-1246.
77 T. Kawai and T. Sakata: Chem. Phys. Lett., 1980, vol. 72, pp. 87-89.
78 Y. Inoue, O. Hayashi, and K. Sato: J. Chem. Soc., Faraday Trans., 1990, vol. 86, pp. 2277-2282.
79 A. Kudo and Y. Miseki: Chem. Soc. Rev., 2009, vol. 38, pp. 253-278.
80 H. W. Nesbitt, G. M. Bancroft, W. S. Fyfe, S. N. Karkhanis, and A. Nishijima: Nature, 1981, vol. 289, pp. 358-362.
81 A. Neubrand, R. Lindner, and P. Hoffmann: J. Am. Ceram. Soc., 2000, vol. 83, pp. 860-864.
82 J. H. Adair, J. Crampo, M. M. Mandanas, and E. Suvaci: J. Am. Ceram. Soc., 2006, vol. 89, pp. 1853-1860.
83 F. Liou and C. Y. Yang: J. Electrochem. Soc., 1982, vol. 129, pp. 342-345.
84 D. W. Kim, S. Lee, H. S. Jung, J. Y. Kim, H. Shin, and K. Hong: Int. J. Hydrogen Energy, 2007, vol. 32, pp. 3137-3140.

85 A. V. Bandura, R. A. Evarestov, and Y. F. Zhukovskii: RSC Adv., 2015, vol. 5, pp. 24115-24125.
86 T. A. Noland: Phys. Rev., 1954, vol. 94, p. 724.
87 Y.-W. Chung and W.B. Weissbard: Phys. Rev. B, 1979, vol. 20, pp. 3456-3461.
88 S. Zollner, A. A. Demkov, R. Liu, P. L. Fejes, R.B. Gregory, P. Alluri, J. A. Curless, Z. Yu, J. Ramdani, R. Droopad, T. E. Tiwald, J. N. Hilfker, and J. A. Woollam: J. Vac. Sci. Technol. B, 2000, vol. 18, pp. 2242-2254.
89 S.K. Hodak, C.T. Rogers: Microelectron. Eng., 2008, vol. 85, pp. 444-451.
90 I. Hod, M. Shalom, Z. Tachan, S. Rühle, and A. Zaban: J. Phys. Chem., 2010, vol. 114, pp. 10015-10018.
91 O. N. Tufte and P. W. Chapman: Phys. Rev., 1967, vol. 155, pp. 796-802.
92 T. Tomio, H. Miki, H. Tabata, T. Kawai, S. Kawai: J. Appl. Phys., 1994, vol. 76, pp. 5886-5890.
93 R. Moos and K. H. Hardtl: J. Am. Ceram. Soc., 1997, vol. 80, pp. 2549-2562.
94 R. N. Hall: Phys. Rev., 1951, vol. 83, p.228.
95 R. N. Hall: Phys. Rev., 1952, vol. 87, p. 387.
96 W. Shockley and W. T. Read: Phys. Rev., 1952, vol. 87, p. 835.
97 C. R. Crowell: Solid-State Electronics, 1965, vol. 8, pp. 395-399.
98 M. Shur: Physics of Semiconductor Devices, Prentice Hall, Upper Saddle River, NJ, 1990.
99 W. C. Clark and A. G. Vondjidis: J. Catal., 1965, vol. 4, pp. 691-696.
100 J.-M. Herrmann, J. Disdier, and P. Pichat: J. Catalysis., 1998, vol. 113, pp. 72-81.
101 K. Tanaka, K. Harada, and S. Murata: Sol. Energy, 1986, vol. 36, pp. 159-161.
102 J. Torres and S. Cervera-March: Chem. Eng. Sci., 1992, vol. 47, pp. 3857-3862.
103 W. M. Haynes: Handbook of Chemistry and Physics: 93rd edition, Chemical Rubber Company, 2012.
104 A. J. Bard, R. Parsons, and J. Jordan: Standard Potentials in Aqueous Solutions, Marcel Dekker, New York, NY, 1985.
105 J. Augustynski: Electrochim. Acta, 1993, vol. 38, p. 43.
106 A. Euken and U.A. Buchner: Z. Phys. Chem. B, 1934, vol. 27, p. 321.
107 S. Roberts: Phys. Rev., 1949, vol. 76, pp. 1215-1220.
108 R. G. Breckenridge and W. R. Hosler: Phys. Rev., 1953, vol. 91, pp. 793-802.
109 C. N. Berglund and W. S. Baer: Phys. Rev., 1967, vol. 157, pp. 358-366.
110 M. E. Lines and A. M. Glass: Principles and Applications of Ferroelectrics and Related Materials, Clarendon, Oxford, 1970.
111 H. Tang, K. Prasad, R. Sanjinès, P. E. Schmid, and F. Lévy: J. Appl. Phys., 1994, vol. 75, pp. 2042-2047.
112 N. A. Deskins and M. Dupuis: J. Phys. Chem. C, 2009, vol. 113, pp. 346-358.
113 P. Günter and H. Jean-Pierre: Photorefractive Materials and Their Applications I: Fundamental Phenomena, Topics in Applied Physics, Springer-Verlag, Berlin, 1988.
114 Y. Xiong and X. Lu: Metallic Nanostructures, Springer, Switzerland, 2015.
115 H. H. Kung, H. S. Jarrett, A. W. Sleight, and A. Ferretti: J. Appl. Phys., 1977, vol. 48, pp. 2463-2469.
116 S. H. Wemple: Phys. Rev. B, 1970, vol. 2, pp. 2679-2689.
117 L. Hafid: Solid State Commun., 1988, vol. 66, pp. 841-845.
118 N. Szydlo, R. Poirier: J. Appl. Phys., 1980, vol. 51, pp. 3310-3312.

119 J. Tang, M. White, G. D. Stucky, and E. W. McFarland: Electrochem. Commun., 2003, vol. 5, pp. 497-501.
120 B. Enright and D. Fitzmaurice: J. Phys. Chem., 1996, vol. 100, pp. 1027-1035.
121 P. Erhart and K. Albe: J. Appl. Phys., 2007, vol. 102, pp. 1-9.
122 T. Sekiya, K. Ichimura, M. Igarashi, and S. Kurita: J. Phys. Chem. Solids, 2000, vol. 61, pp. 1237-1242.
123 H. Tang, F. Lévy, H. Berger, and P. E. Schmid: Phys. Rev. B, 1995, vol. 52, pp. 7771-7774.
124 Report, MTI Corp: "Verneuil Crystal Growth", 2016.
125 K. Szot, W. Speier, R. Carius, U. Zastrow, and W. Beyer: Phys. Rev. Lett., 2002, vol. 88, pp. 075508-1-4.
126 D. Bäuerle, W. Braun, V. Saile, G. Sprüssel, and E. E. Koch: Z. Physik B, 1978, vol. 29, pp. 179-184.
127 K. Ozawa, M. Emori, S. Yamamoto, R. Yukawa, S. Yamamoto, R. Hobra, K. Fujikawa, H. Sakama, and I. Matsuda: J. Phys. Chem. Lett., 2014, vol. 5, pp. 1953-1957.
128 G. A. Brost, R. A. Motes, and J. R. Rotge: J. Opt. Soc. Am. B, 1988, vol. 5, pp. 1879-1885.
129 J. J Glickstein, P. A. Salvador, and G. S. Rohrer: J. Phys. Chem. C, 2016, vol. 120, pp. 12673-12684.
130 COMSOL Multiphysics® v. 5.1 www.comsol.com. COMSOL AB, Stockholm, Sweden.
131 A. T. Garcia-Esparza and K. Tankanabe: J. Mater. Chem. A, 2016, vol. 4, pp. 2894-2908.
132 C. R. Crowell: Solid State Electron., 1965, vol. 8, pp. 395-399.
133 E. Pelizzetti and M. Schiavello (eds.): Photochemical Conversion and Storage of Solar Energy, 193-212, Kluwer Academic Publishers, Palermo, 1991.
134 S. Bai, J. Jiang, Q. Zhang, and Y. Xiong: Chem. Soc. Rev., 2015, vol. 44, pp. 2893-2939.
135 M. R. Morris, S. R. Pendlebury, J. Hong, S. Dunn, and J. R. Durrant: Adv. Mater., 2016.
136 Y. Sun and R. J. Nemanich: J. Appl. Phys., 2011, vol. 109, pp. 104302-1-7.
137 J. N. Hanson, B. J. Rodriguez, R. J. Nemanich, and A. Gruverman: Nanotechnology, 2006, vol. 17, pp. 4946-4949.
138 S.R. Morrison: Electrochemistry at Semiconductor and Oxidized Metal Electrodes, Plenum Press, New York, NY, 1980.